THE LOW TEMPERATURE ACOUSTIC PROPERTIES OF AMORPHOUS SILICA AND POLYCRYSTALLINE ALUMINUM

A Dissertation

Presented to the Faculty of the Graduate School

of Cornell University

in Partial Fulfillment of the Requirements for the Degree of

Doctor of Philosophy

by

Andrew Douglas Fefferman

August 2009

THE LOW TEMPERATURE ACOUSTIC PROPERTIES OF AMORPHOUS SILICA AND POLYCRYSTALLINE ALUMINUM

Andrew Douglas Fefferman, Ph.D.

Cornell University 2009

The standard tunneling model of glass invokes low energy excitations due to tunneling two level systems to explain the universal properties observed in glasses below 1 K. Our measurements of the internal friction Q^{-1} and relative change in sound speed $\delta v/v_0$ in amorphous SiO_2 at three frequencies in the kHz range showed that the standard tunneling model is valid down to 10 mK, a much lower temperature than was previously thought. Yet below 10 mK, we observed a crossover from the prediction of the standard tunneling model to a $Q^{-1} \propto T$ dependence. This weaker temperature dependence is evidence for an additional two level system relaxation mechanism that dominates over phonon-driven relaxation at the lowest temperatures. While the nature of the additional TLS relaxation mechanism remains a topic of theoretical debate, the most likely explanation is interactions between pairs of two level systems. We were able to fit the theory to the observed Q^{-1} at all three frequencies with a single additional parameter, the interaction-driven relaxation rate. A weaker than expected temperature dependence of $\delta v/v_0$ below 3 mK is also studied, and it is shown that thermal decoupling is an unlikely explanation. Finally, glassy behavior in the acoustic properties of a polycrystalline aluminum film is discussed in the context of previous measurements on aluminum and models of dislocation-phonon interactions.

BIOGRAPHICAL SKETCH

The author was born in 1980 in Los Angeles. He attended Oakwood, a small school in the East San Fernando Valley, from kindergarten until 12th grade. His excellent high school physics teacher inspired him to pursue advanced study in the field. During the summer before staring college, he assisted in Tom Donnelly's ultrafast optics lab at Harvey Mudd College. Finding endless sunshine tedious, he began studying physics at beautiful Swarthmore College. There he was introduced to the elegance of quantum theory by John Boccio and to the art of experimental physics by Michael Brown. Upon graduating with high honors, he began the physics Ph.D. program at Cornell and joined Jeevak Parpia's lab a year later. There he studied the systems discussed in this dissertation as well as superfluidity of ^{3}He in aerogel using the torsional oscillator technique.

ACKNOWLEDGEMENTS

There are many who shaped my experience at Cornell. My graduate education would not have been the same without the day-to-day interactions with the residents of Clark basement. I interacted with people from almost all the experimental groups with regards to my research at some point, and my conversations with Ethan Bernard, Jared Hertzberg, Jarno Jaervinen, Ethan Pratt, Ryan Gutenkunst and Jee Hye Lee were particularly in depth and rewarding. Jared and I worked together to deposit the aluminum film on the silicon resonator, allowing me to take the data discussed in chapter 4 of this dissertation. The other members of the Parpia research group were a pleasure to work with. Eric Smith taught me a huge amount about low temperature physics and patiently answered all of my questions during the early years. Dan Ralph, Carl Franck and Keith Schwab were particularly generous with their time, taught me a lot of physics, and gave good advice. It was a pleasure to work with Alan Zehnder on the FEM calculation of the paddle modes. Tom Metcalf and Xiao Liu of NRL were extremely helpful for the elastic measurements on metal films. Jim Sethna served as the theoretician on my special committee and provided a great deal of theoretical insight. Seamus Davis also served on my committee and provided insight on the experimental side. I was very privileged to work closely with Bobby Pohl, because of his esteemed background, his knowledge of the field, and his good nature. My deepest thanks among the faculty go to Jeevak Parpia, my special committee chair, for his steadfast support, confidence in my abilities, and for all that he has taught me. Beyond Cornell, the support of taxpayers via the National Science Foundation and DARPA provided the resources that made my graduate studies possible. Finally, none of this would have been possible without the support of my parents throughout my education.

TABLE OF CONTENTS

LIST OF TABLES

LIST OF FIGURES

CHAPTER 1

THEORY OF AMORPHOUS SOLIDS AT LOW TEMPERATURES

1.1 Introduction

At temperatures much below the Debye temperature, at which the phonon wavelengths are long, a lattice can be considered as an elastic continuum. Thus one might expect that an amorphous solid (a glass) at low temperatures should act much like a crystal since the long wavelength phonons should be insensitive to disorder at length scales comparable to the interparticle spacing. However, it was discovered in the early 1970's [9] that certain properties of glasses are quite different from those of crystals.

In a crystal, the Debye density of phonon states leads to a specific heat capacity $C_{crys} \propto T^3$ [10]. In the relaxation time approximation, the thermal conductivity is given by

$$\kappa_{crys} = \frac{1}{3} C_{crys} v^2 \tau. \tag{1.1}$$

The sound speed v depends on the masses of the ions in the crystal and their interaction energies, which should be temperature independent at low temperatures. If the temperature is sufficiently low, the phonon relaxation time τ is no longer limited by intrinsic, anharmonic processes. The relaxation time in a perfect crystal is then determined by the finite size of the crystal and becomes temperature independent [10]. Thus the thermal conductivity shares the cubic temperature dependence of the heat capacity.

A weaker temperature dependence was observed in glasses for both the thermal conductivity and heat capacity. Fig. 1.1 shows the thermal conductivity of

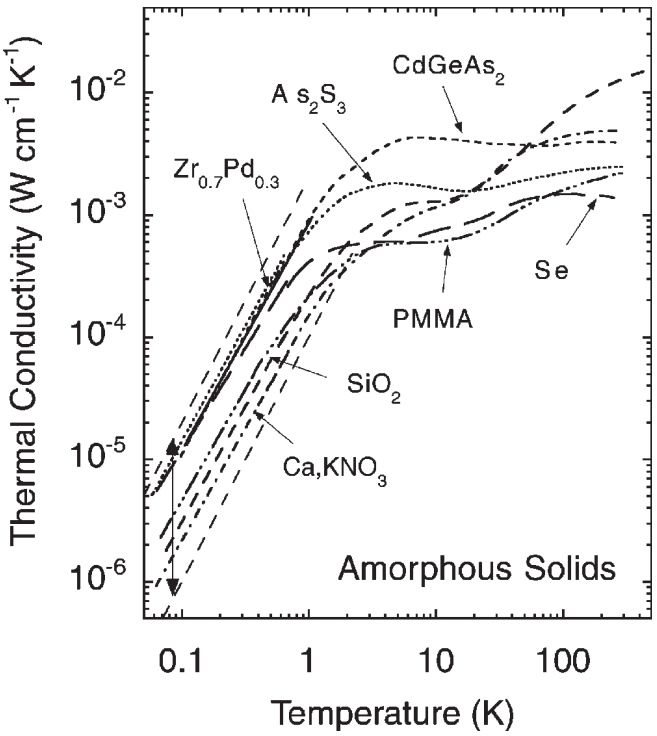

Figure 1.1: Thermal conductivity of several amorphous solids (from [1]). Each glass exhibits a roughly quadratic temperature dependence below 1 K. The "glassy range" is bounded by the two dashed lines and spanned by the double headed arrow.

several glasses, and κ_{glass} has a roughly quadratic temperature dependence for all of them. According to [1], the thermal conductivity of all glasses measured below 1 K is in the range spanned by the two dotted lines in Fig. 1.1, which is called the glassy range. Measurements of the heat capacity of several glasses have revealed a roughly linear temperature dependence [11].

The physical picture that was developed to account for these properties is the standard tunneling model (STM) [12, 13]. The model is reviewed in [11]. Briefly, this model supposes the existence of tunneling two level defects in the glass with a broad distribution of energy splittings [1]. The heat capacity of a

[1]It is argued in [14] that the STM is a member of a more general class of models, and that

two level system (TLS) and its interaction with phonons depends on the energy splitting of the TLS. Averaging the thermal properties over the distribution of TLS energy splittings leads to a heat capacity that is linear in temperature and a quadratic temperature dependence for the thermal conductivity, in agreement with low temperature observations. The STM does not, however, account for the similarities in the magnitudes of various quantities such as the thermal conductivity below 1 K [1]. This deficiency has been addressed by several authors [14, 15, 16].

Although the STM has been rather successful in predicting the low temperature behavior of nearly all types of glass, in many cases it is not known what forms the two level systems. The chemical composition of amorphous SiO_2 (vitreous silica) is simple, and its structure has been studied using x-ray diffraction. The basic building block of vitreous silica, as well as almost all forms of crystalline SiO_2, is the SiO_4 tetrahedron. In crystalline SiO_2, the tetrahedra are bound together in a well defined way. However, in vitreous silica, the Si-O-Si bond angle ranges between 120 and 180 degrees, with a mean of 150 degrees, and the tetrahedra rotation angle is random [17]. With this degree of disorder, one can imagine that nearby metastable states can form, leading to tunneling two level systems. A number of defect candidates have been identified in vitreous silica as shown in Fig. 1.2: one is the O atom in SiO_2 [18]. If the neighboring Si atoms are spaced too far apart, then the O atom experiences a two level potential. In [18], the interaction between the Si atoms and the O atom was approximated as a sum of Morse potentials: $(1-e^{-x-a})^2+(1-e^{x-a})^2$. If $a > \ln[2] \approx 0.69$, then the potential has two minima. Fig. 1.3 is a plot of the potential for a few values of a. Although the precise origin(s) of the hypothetical two level systems

other models in the class may better explain certain features of the data.

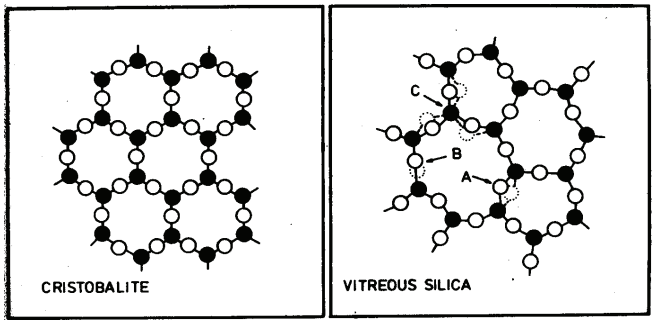

Figure 1.2: Crystalline and vitreous SiO_2 are made up of the same basic units: SiO_4 tetrahedra. However, vitreous SiO_2 has an irregular lattice. Three possible types of two level systems in the vitreous state are labeled. Figure is from [2]

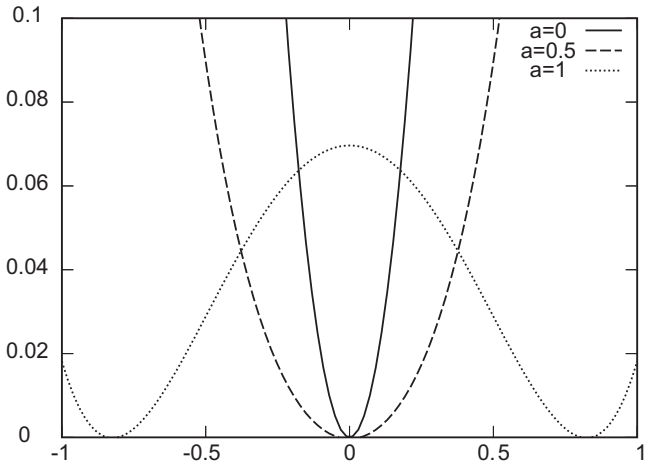

Figure 1.3: The sum of two Morse potentials $(1 - e^{-x-a})^2 + (1 - e^{x-a})^2$ for the indicated values of a. The zero-offset of the potential was subtracted for each value of a. A double well potential forms for $a > \ln[2] \approx 0.69$.

(TLS) in glasses are not known, the model is rather successful if it is assumed that the distribution of TLS energy splittings is approximately flat.

As shown in Fig. 1.4, a TLS can be characterized by an asymmetry, Δ, and a tunneling amplitude, Δ_0. The tunneling amplitude is approximated by [11]

$$\Delta_0 = \hbar\Omega \exp(-\lambda) \tag{1.2}$$

where

$$\lambda = -d(2mV_0/\hbar^2)^{1/2}, \tag{1.3}$$

Ω is approximately the mean ground state energy for the potential wells in the TLS if they were isolated, d is the separation between the minima of the two wells, m is the mass of the tunneling entity, and V_0 is the height of the TLS barrier. Although it is not clear that the potential shown in Fig. 1.4 is the best representation for real TLS, experimental data are generally well described by assuming a distribution

$$P(\Delta, \Delta_0) = P_0/\Delta_0 \tag{1.4}$$

without reference to the dependence of Δ_0 on d and V_0. For mathematical convenience, it is often desirable to transform the distribution to a function of different parameters using the Jacobian; several examples are given on p. 15 of [19]. However, it is easiest to see the physical justification for the assumed distribution using the form in Eq. 1.4 [11]. The distribution is expected to be symmetric in the asymmetry since there is no reason that a positive asymmetry should be favored over a negative one. The scale of the energy variation of the asymmetry is set by the glass transition temperature, which is typically near 1000 K. Since at low temperatures the relevant tunneling states have asymmetries much less than 1000 K, the distribution of asymmetries can be considered approximately constant. The exponential dependence of Δ_0 on λ in Eq. 1.2 means that for a

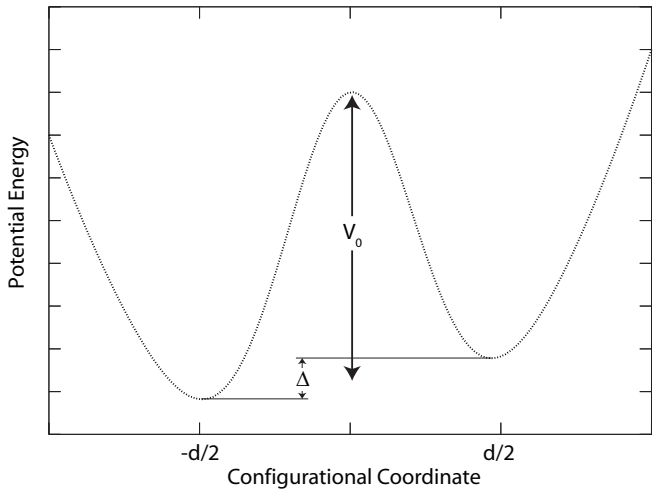

Figure 1.4: A generic TLS is characterized by an asymmetry, Δ, a well separation d, a barrier height V_0, and a tunneling amplitude Δ_0. The exact dependence of Δ_0 on d and V_0 depends on the precise shape of the potential, which is generally unknown.

small change in λ there is a large change in Δ_0. Thus the range of λ sampled in a low temperature experiment is narrow, and the distribution in λ can be considered uniform, leading to the $1/\Delta_0$ dependence in Eq. 1.4 (p. 15 of [19]).

1.2 Interactions Between Two Level Systems and Phonons

So far the TLS has been discussed in isolation, while in a glass the ensemble of TLS interacts with thermal phonons and phonons added due to externally imposed excitations. The interaction of phonons with TLS is discussed in mathematical detail below, but here I give a basic overview. The acoustic experimental observables are the internal friction Q^{-1} and the relative change in sound speed $(v-v_0)/v_0 \equiv \delta v/v_0$, where v_0 is the sound speed at an arbitrary reference temperature. TLS-phonon interactions contribute to the acoustic observables through

relaxational and resonant processes. In the resonant process, externally applied excitation phonons at ω_0 are scattered by TLS with energy splitting $E = \omega_0$, driving the phonon population towards the thermal equilibrium distribution. The resonant contribution to the internal friction is proportional to the phonon scattering rate, and the resonant contribution to $\delta v/v_0$ can be obtained from Q^{-1} using the Kramers-Kroenig relation. Although the resonant contribution to Q^{-1} is small for the temperature and frequency range in the experiment discussed in this dissertation, because the Kramers-Kroenig relation involves integration over all frequencies, the resonant contribution to $\delta v/v_0$ is substantial. In the relaxational process, externally applied phonons interact with TLS of any energy splitting by perturbing the TLS potential energy and thus changing the energy splitting. The ensemble of TLS is then no longer in thermal equilibrium, and thermal phonons interact with the TLS, driving them back to thermal equilibrium. Since re-equilibration of the TLS involves motion of particles in the lattice, it contributes to the stress in the lattice per unit strain, thus contributing to the modulus. The real part of the change in the modulus is proportional to the relaxational contribution to $\delta v/v_0$ and the imaginary part of the change in the modulus is proportional to the relaxational contribution to Q^{-1}.

The Hamiltonian for an isolated TLS in the position basis is

$$H_0 = \frac{1}{2} \begin{pmatrix} -\Delta & \Delta_0 \\ \Delta_0 & \Delta \end{pmatrix}_p .$$

The energy eigenvalues of the Hamiltonian are $\pm E/2$ with $E = \sqrt{\Delta^2 + \Delta_0^2}$. The energy eigenstates are plotted in position space for several values of Δ_0/E in Fig. 1.3 of [19]. For symmetric TLS (i.e. $\Delta = 0$), the position states are symmetric and anti-symmetric superpositions of the energy states. For highly asymmetric TLS (i.e. $\Delta_0 = 0$), the position states are the energy eigenstates.

The Hamiltonian H_0 corresponds to an isolated TLS. In an amorphous solid, the two level systems and atoms interact in a manner that is related to the interaction of photons with atoms. The latter system is studied in detail in [20]. Because the phonon wavelengths of interest are much greater than the separation between potential minima in the TLS, the phonons primarily couple to the asymmetry Δ rather than the tunneling amplitude Δ_0, as shown in Fig. 1.5. Thus the TLS-phonon interaction Hamiltonian in the position basis is

$$H_{int} = \gamma e \begin{pmatrix} -1 & 0 \\ 0 & 1 \end{pmatrix}_p ,$$

where the deformation potential $\gamma \equiv \frac{1}{2}\partial\Delta/\partial e$. When transformed to the energy basis, the interaction Hamiltonian becomes [11]

$$H_{int} = \gamma e/E \begin{pmatrix} \Delta & \Delta_0 \\ \Delta_0 & -\Delta \end{pmatrix}_E .$$

When the strain fields are weak enough, the dynamics can be described by rate equations [11]

$$\dot{p}_1 = -p_1\omega_{12} + p_2\omega_{21} \tag{1.5}$$

$$\dot{p}_2 = p_1\omega_{12} - p_2\omega_{21} \tag{1.6}$$

where p_i is the TLS occupation probability for state $|\psi_i\rangle$, $|\psi_1\rangle$ is the high energy state, and ω_{12} is the transition rate from $|\psi_1\rangle$ to $|\psi_2\rangle$ (emission). Using $p_1 + p_2 = 1$, we have

$$\dot{p}_1 = -p_1\omega_{12} + (1 - p_1)\omega_{21}. \tag{1.7}$$

We can now use these rate equations to derive the TLS and phonon relaxation rates. My derivation of the relaxation rates mainly follows that in [11], although I have tried to make the derivation more rigorous.

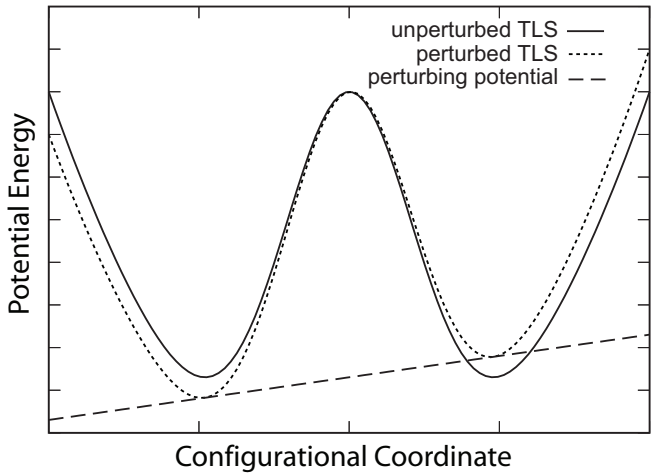

Figure 1.5: Strain fields couple mainly to the asymmetry of TLS. At low temperatures and low drive frequencies, the strain field wavelength is long compared to the well separation, yielding a linear perturbing potential to lowest non-trivial order. The relative change in asymmetry is much greater than the relative change in barrier height or well separation.

1.2.1 Two Level System Relaxation Rate

In this subsection, I assume that the phonons are in thermal equilibrium and that the TLS population has been perturbed away from thermal equilibrium. In this case, the phonon population is determined by the Bose factor and the TLS transition rates ω_{12} and ω_{21} are time independent. The solution to Eq. 1.7 is

$$p_1 = e^{-t/\tau} + \omega_{21}\tau \tag{1.8}$$

with the rate

$$\tau^{-1} = \omega_{12} + \omega_{21} \tag{1.9}$$

governing the relaxation of the two level systems to equilibrium. At infinite times, $p_1 = \omega_{21}\tau = \omega_{21}/(\omega_{12} + \omega_{21})$. If it is assumed that the phonon distribution remains thermal as the two level systems equilibrate, one can show that this is

the expected thermal equilibrium value for p_1 using Eq. 1.21 and using $p_1 + p_2 = 1$. The transition rate for a TLS with energy splitting E can be obtained from Fermi's Golden Rule [21]:

$$\omega_{12}(E) = \sum_{s,\vec{k}} \frac{2\pi}{\hbar} \left| \left\langle \psi_2, n_{ph}(\omega_s(\vec{k})) + 1 \right| H_{int} \left| \psi_1, n_{ph}(\omega_s(\vec{k})) \right\rangle \right|^2 \delta(E - \hbar\omega_s(\vec{k})) \tag{1.10}$$

$$= \int \frac{2\pi}{\hbar^2} |\left\langle \psi_2, n_B(\omega) + 1 \right| H_{int} \left| \psi_1, n_B(\omega) \right\rangle|^2 \delta(E/\hbar - \omega) g(\omega) d\omega \tag{1.11}$$

$$\omega_{21}(E) = \int \frac{2\pi}{\hbar^2} |\left\langle \psi_1, n_B(\omega) - 1 \right| H_{int} \left| \psi_2, n_B(\omega) \right\rangle|^2 \delta(E/\hbar - \omega) g(\omega) d\omega \tag{1.12}$$

where ω is the phonon angular frequency, $n_{ph}(\omega_s(\vec{k}))$ is the occupation number for a phonon mode with wavevector $\vec{k}$ and polarization s, and $g(\omega) = 3\omega^2/2\pi^2 v^3$ is the Debye density of phonon states [10]. The factor of three in the Debye density of states corresponds to the three possible phonon polarizations. As will be seen below, the factor γ^2/v^5 appears in the final result for the TLS relaxation rate. Although γ/v could in principle depend on phonon polarization, it is argued in [4] that it does not. Assuming that v also does not depend strongly on polarization, we can replace the sum over polarizations with the factor of three in the density of states. Since the phonons are in thermal equilibrium, the occupation number is given by the Bose factor $n_{ph}(\omega_s(\vec{k})) = n_B = 1/(\exp(\hbar\omega/k_B T) - 1)$. We integrate over all frequencies because we are interested in contributions to the transition rate from all phonons present in the thermal equilibrium ensemble. The TLS matrix element is easily evaluated, giving

$$\left\langle \psi_1, n_B(\omega) - 1 \right| H_{int} \left| \psi_2, n_B(\omega) \right\rangle = \gamma \frac{\Delta_0}{E} \left\langle n_B(\omega) - 1 \right| e \left| n_B(\omega) \right\rangle . \tag{1.13}$$

From the expression for the displacement in terms of second quantization from Appendix L of [10], the strain is

$$e = \nabla \vec{u}(\vec{R}) = \sum_{k,s} \sqrt{\frac{\hbar}{2\rho\omega_s(k)}} (a_{ks} + a^\dagger_{-ks}) \epsilon_s(k) e^{i\vec{k}\cdot\vec{R}} ik \cos\theta. \tag{1.14}$$

A rigorous derivation including the tensor nature of the strain is given in [22]. Here we simply take a directional average of the strain and evaluate it at $R = 0$, yielding

$$\langle n_B(\omega) - 1 \,|\, e \,|\, n_B(\omega) \rangle = \sqrt{\frac{\hbar}{2\rho\omega}} ik(\omega) \sqrt{n_B(\omega)} \tag{1.15}$$

$$\langle n_B(\omega) + 1 \,|\, e \,|\, n_B(\omega) \rangle = \sqrt{\frac{\hbar}{2\rho\omega}} ik(\omega) \sqrt{n_B(\omega) + 1}. \tag{1.16}$$

Substituting Eqs. 1.13, 1.15 and 1.16 into Eqs. 1.11 and 1.12, we have

$$\omega_{12}(E) = \frac{2\pi}{\hbar^2} \left(\frac{\gamma \Delta_0}{E} \right)^2 \frac{\hbar}{2\rho\omega} k^2(\omega) g(\omega) (n_B(\omega) + 1) \tag{1.17}$$

$$\omega_{21}(E) = \frac{2\pi}{\hbar^2} \left(\frac{\gamma \Delta_0}{E} \right)^2 \frac{\hbar}{2\rho\omega} k^2(\omega) g(\omega) n_B(\omega), \tag{1.18}$$

where $E = \hbar\omega$. The one in the last term in parentheses in Eq. 1.17 corresponds to spontaneous emission, since this contribution to the rate is independent of the density of phonons. Taking the ratio of Eqs. 1.17 and 1.18, we have

$$\frac{\omega_{12}(E)}{\omega_{21}(E)} = \frac{n_B(E) + 1}{n_B(E)} = e^{E/k_B T}. \tag{1.19}$$

There is an alternative way of obtaining Eq. 1.19 [11]: Since the transition rates ω_{12} and ω_{21} are independent of the TLS occupation probabilities, their ratio can be determined from the case where the TLS occupation probabilities are in thermal equilibrium. Thus we can set the left hand side of Eqs. 1.5 or 1.6 to zero, yielding

$$\frac{p_2^0}{p_1^0} = \frac{\omega_{12}}{\omega_{21}}, \tag{1.20}$$

where p_1^0 is the thermal equilibrium population for state $|\psi_1\rangle$. Since the ratio of the thermal equilibrium occupancies $\frac{p_2^0}{p_1^0}$ is given by the Boltzmann factor, we have

$$\frac{\omega_{12}}{\omega_{21}} = e^{E/k_B T}. \tag{1.21}$$

Thus we obtain from Eq. 1.9

$$\tau^{-1} = \omega_{21}[1 + \exp(E/k_B T)]. \tag{1.22}$$

Substituting Eq. 1.18 into Eq. 1.22 we have

$$\tau^{-1}(E) = \frac{3\gamma^2}{v^5}\frac{E\Delta_0^2}{2\pi\rho\hbar^4}\coth(E/2k_B T), \tag{1.23}$$

where v is the sound speed in the absence of TLS, we have used the Debye approximation for the phonon wavevector $k = \omega/v$, and we have used $E = \hbar\omega$ due to the delta function in Fermi's Golden Rule.

1.2.2 Phonon Relaxation Rate

In this subsection, I assume that the two level systems are in thermal equilibrium and that the phonon population at frequency ω has been perturbed away from thermal equilibrium. By conservation of energy, changes in the phonon population at ω must be due to emission or absorption of phonons by two level systems with energy splitting $E = \omega$:

$$\dot{n}_{ph}(\omega) = -\int_0^\infty \int_0^E \dot{p}_1 P(E, \Delta_0)\delta(E - \hbar\omega) d\Delta_0 dE, \tag{1.24}$$

Substituting Eq. 1.5 into Eq. 1.24, we have

$$\dot{n}_{ph} = \int_0^\infty \int_0^E [-p_1\omega_{12} + p_2\omega_{21}]P(E, \Delta_0)\delta(E - \hbar\omega) d\Delta_0 dE. \tag{1.25}$$

Using the expressions for the TLS transition rates Eqs. 1.17 and 1.18, we have

$$\dot{n}_{ph} = \int_0^\infty \int_0^E \Xi[-p_1(n_{ph} + 1) + p_2 n_{ph}]P(E, \Delta_0)\delta(E - \hbar\omega) d\Delta_0 dE \tag{1.26}$$

$$= \int_0^\infty \int_0^E \Xi[n_{ph}\delta p - p_1]P(E, \Delta_0)\delta(E - \hbar\omega) d\Delta_0 dE, \tag{1.27}$$

where

$$\Xi = \frac{2\pi}{\hbar}\left(\frac{\gamma\Delta_0}{E}\right)^2 \frac{\hbar}{2\rho\omega}k^2(\omega) \tag{1.28}$$

is the prefactor of the TLS transition rates (Eqs. 1.17 and 1.18) and δp is the TLS polarization $p_2 - p_1$. The solution to this equation is

$$n_{ph} = -\frac{p_1}{\delta p}(1 - Ae^{-t/\tau_{ph}}) \tag{1.29}$$

where A is some constant and

$$\tau_{ph}^{-1} = \int_0^\infty \int_0^E \Xi P(E, \Delta_0)\delta p \delta(E - \hbar\omega) d\Delta_0 dE \tag{1.30}$$

$$= \int_0^\infty \int_0^E \frac{2\pi}{\hbar}\left(\frac{\gamma\Delta_0}{E}\right)^2 \frac{\hbar}{2\rho\omega}k^2(\omega)P(E, \Delta_0)\delta p \delta(E - \hbar\omega) d\Delta_0 dE. \tag{1.31}$$

where the expression for Ξ from Eq. 1.28 was used. Since the TLS are in thermal equilibrium by assumption, we have the polarization

$$\delta p = \delta p^{(0)} = \tanh(E/2k_BT). \tag{1.32}$$

Substituting Eq. 1.32 along with the Debye approximation, $k = (\omega/v)^2$, in Eq. 1.31 yields

$$\tau_{ph}^{-1} = \int_0^\infty \int_0^E \pi\frac{\gamma^2}{\rho v^2}\left(\frac{\Delta_0}{E}\right)^2 \omega \tanh\left(\frac{E}{2k_BT}\right)\delta(E - \hbar\omega)P(E, \Delta_0)d\Delta_0 dE. \tag{1.33}$$

Using a transformed version of Eq. 1.4 from [19]

$$P(E, \Delta_0) = \frac{P_0}{\Delta_0\sqrt{1 - \frac{\Delta_0^2}{E^2}}}. \tag{1.34}$$

we have

$$\int_0^E P(E, \Delta_0)\Delta_0^2 d\Delta_0 = P_0E^2. \tag{1.35}$$

Substituting Eq. 1.35 into Eq. 1.33, we have

$$\tau_{ph}^{-1} = \pi\omega C \tanh\frac{\hbar\omega}{2k_BT}. \tag{1.36}$$

where we have defined the tunneling strength

$$C \equiv \frac{P_0\gamma^2}{\rho v^2}. \tag{1.37}$$

1.3 Response of the Amorphous Solid to Imposed Strain Perturbations

Consider an externally imposed strain perturbation at frequency f_0 applied to an amorphous solid in which the ensemble of two level systems and the ensemble of phonons are both initially in thermal equilibrium. At low temperatures, the temperature dependence of acoustic properties is dominated by the phonon-TLS interactions. There are two ways in which the drive phonons can interact with TLS: the resonant and the relaxational processes. In the resonant process the drive phonon frequency must match the TLS energy splitting, as in Eq. 1.11. In this case, it is assumed that the TLS remain in thermal equilibrium and drive the phonon population back toward thermal equilibrium as the amorphous solid is perturbed by the drive strain at frequency f_0. The resonant process is thus characterized by the rate τ_{ph}^{-1} (Eq. 1.36). In the relaxational process, it is assumed that the phonon population is in thermal equilibrium (except for the drive phonons at f_0) and that the TLS are perturbed out of thermal equilibrium as the drive modulates their energy splittings. Note that the TLS energy splitting need not equal the phonon energy in this case. As noted in Fig. 1.5, the phonons mainly perturb the distribution of energy splittings E via the TLS asymmetry Δ. Resonant interactions between thermal phonons and TLS then drive the TLS population back towards thermal equilibrium at the rate τ^{-1}. Yet in the case of a continuous, periodic strain perturbation (at frequency f_0), the TLS population never reaches instantaneous equilibrium.

Naming the two phonon-TLS interaction processes "resonant" and "relaxational" can lead to some confusion since the relaxational process depends on

resonant thermal phonons. These thermal phonons with $E = \hbar\omega$ drive the TLS back to thermal equilibrium after non-resonant drive phonons perturb the TLS. Thus the term "resonant" refers to the equality of the *drive* phonon energy and TLS energy splitting.

The two types of phonon-TLS interaction processes lead to an anelastic response of the amorphous solid. An ideal elastic material has a unique equilibrium relationship between stress and strain, the equilibrium response is achieved instantaneously (after accounting for the finite velocity of sound), and the response is linear [23]. The first condition implies that the response is completely recoverable and the material is not plastic. An anelastic material fulfills the first and third conditions (recoverability and linearity), but the equilibrium response is not immediately realized. The properties of anelastic materials are discussed in great detail in [23]. In an experiment in which a strain is suddenly applied to an anelastic material, the stress is given by the strain times the time dependent modulus. The initial value of the modulus is the unrelaxed modulus. As time elapses, the modulus asymptotically decreases towards the relaxed modulus. In an experiment in which an alternating strain is applied, the stress is out of phase with the strain by an angle depending on the frequency of excitation. In this case, the stress is equal to the strain times the complex modulus. [2] Thus a non-zero imaginary part of the complex modulus indicates that the material is anelastic. However, in the zero (infinite) frequency limit, the complex modulus equals the relaxed (unrelaxed) modulus (Eq. 1.3-16 and 1.3-17 of [23]), and the imaginary part of the complex modulus therefore vanishes.

[2] Some works (e.g. [24, 11, 25]) take the elastic susceptibility χ to be equivalent to the modulus. This convention seems to have arisen from the analogy between structural two level systems in an elastic field and spins in a magnetic field [24]. The modulus in the elastic case plays a role analogous to the susceptibility in the magnetic case. However, some confusion can arise because other works, e.g. [26], consider the susceptibility to be equivalent to the compliance, i.e. the strain per unit stress. I avoid the use of "susceptibility" in this dissertation.

In an amorphous solid, the complex modulus can be written as

$$M = \frac{\sigma}{e} = M_0 + M_{rel} + M_{res} \tag{1.38}$$

where σ is the stress, e is the strain, M_0 is the contribution of non-TLS processes and M_{rel} (M_{res}) is the relaxational (resonant) contribution to the complex modulus. Both the resonant and relaxational interactions contribute to the anelasticity since both interactions contribute to a phase difference between the stress and strain. Thus the resonant interaction as well as the relaxational interaction leads to relaxation of the macroscopic response of the amorphous solid, which might lead to some confusion. At low temperatures, the contribution from processes not involving TLS is nearly temperature independent and the dissipative part is small. Thus we can subtract the contribution of non-TLS processes to the sound speed and neglect their contribution to the dissipation. Therefore one of the theoretical quantities of interest is M_{rel}, which we will derive using the TLS relaxation rate Eq. 1.23. We will also derive expressions for the experimental observables in terms of M_{rel}. For simplicity, the resonant response will be given directly in terms of experimental observables without explicitly stating M_{res}. A derivation of M_{res} is given in [24] using a Bloch equation approach.

1.3.1 Relaxational Modulus

This argument follows those in [11] and [2]. I have tried to rewrite and expand upon the argument so that it is more directly applicable to the discussion above. Considering for now just a single class of TLS (particular Δ and Δ_0) with volume density n, we can derive a Maxwell-like relation that relates the strain dependence of the total energy to the dependence of the stress on the popula-

tion of the TLS excited state. The fundamental thermodynamic relation for a quasi-static infinitesimal process is [27]

$$dq = dE_{tot} - \sigma_{ij} de_{ij} - nE dp_1 \tag{1.39}$$

where dq is the heat per unit volume flowing into the solid, E_{tot} is the total energy per unit volume, the stress and strain are taken as second order tensors and repeated subscripts indicate summation. From the second law of thermodynamics [27], we have

$$dq = Tds \tag{1.40}$$

where s is the volume density of the entropy. Thus

$$\begin{aligned} dE_{tot} &= Tds + \sigma_{ij} de_{ij} + nE dp_1 & (1.41)\\ &= d(Ts) - sdT + \sigma_{ij} de_{ij} + nE dp_1. & (1.42) \end{aligned}$$

Substituting in the Helmholtz free energy density $f = E_{tot} - Ts$ yields

$$df = -sdT + \sigma_{ij} de_{ij} + nE dp_1. \tag{1.43}$$

Following the usual procedure for deriving Maxwell relations from thermodynamic potentials (Section 5.5 of [27]), one obtains

$$n \left(\frac{\partial E}{\partial e_{ij}} \right)_{T,p_1} = \left(\frac{\partial \sigma_{ij}}{\partial p_1} \right)_{T,e}. \tag{1.44}$$

Using

$$\frac{\partial E}{\partial e_{ij}} = \frac{\Delta}{E} \frac{d\Delta}{de_{ij}} \tag{1.45}$$

we have

$$\left(\frac{\partial \sigma_{ij}}{\partial p_1} \right)_{e,T} = n \frac{\Delta}{E} \gamma_{ij}. \tag{1.46}$$

Multiplying both sides by dp_1, we have the relaxational contribution to the stress

$$\sigma_{rel,ij} \equiv n \frac{\Delta}{E} \gamma_{ij} dp_1. \tag{1.47}$$

We now need to find an expression for dp_1 in terms of the strain e to obtain an expression for the relaxational contribution to the modulus. As noted above, the applied strain perturbs the TLS asymmetries periodically, which changes the instantaneous equilibrium population p_1^l continuously. We have to first order

$$p_1^l = p_1^{(0)} + \frac{dp_1^{(0)}}{d\Delta}\frac{d\Delta}{de_{kl}}e_{kl} \tag{1.48}$$

$$= p_1^{(0)} + \frac{dp_1^{(0)}}{d\Delta}\gamma_{kl}e_{kl}, \tag{1.49}$$

where $p_1^{(0)}$ is the equilibrium population in the absence of the strain perturbation. Assuming small excursions from instantaneous equilibrium, we have

$$\dot{p}_1 = -\frac{p_1 - p_1^l}{\tau} \tag{1.50}$$

and we define $\delta p_1 \equiv p_1 - p_1^{(0)}$. Therefore, substituting the expression for the instantaneous equilibrium population Eq. 1.49 into Eq. 1.50 we have

$$\tau\frac{d\delta p_1}{dt} = -\delta p_1 + \frac{dp_1^{(0)}}{d\Delta}\gamma_{kl}e_{kl}. \tag{1.51}$$

Assuming $e = e_0\exp(+i\omega t)$, the solution to this differential equation is [11]

$$\delta p_1 = \frac{dp_1^{(0)}}{d\Delta}\gamma_{kl}\frac{e_{kl}}{1+i\omega\tau}. \tag{1.52}$$

Substituting Eq. 1.52 into Eq. 1.47 with $dp_1 = \delta p_1$ (since δp_1 is small by assumption), we have

$$\sigma_{rel,ij} = n\frac{\Delta}{E}\gamma_{ij}\frac{dp_1^{(0)}}{d\Delta}\gamma_{kl}\frac{e_{kl}}{1+i\omega\tau}. \tag{1.53}$$

and

$$M_{rel,ijmn} = \frac{\sigma_{rel,ij}}{e_{mn}}. \tag{1.54}$$

In order to simplify this expression, I neglect the tensor nature of the elastic fields, yielding

$$M_{rel} = \frac{\sigma_{rel}}{e} = \frac{M_{rel}(0)}{1+i\omega\tau}. \tag{1.55}$$

where the zero frequency modulus

$$M_{rel}(0) = n\gamma^2 \frac{\Delta}{E} \frac{dp_1^{(0)}}{d\Delta}. \tag{1.56}$$

We now need to evaluate $\frac{dp_1^{(0)}}{d\Delta}$. Since the thermal equilibrium polarization $\delta p^{(0)} = p_2^{(0)} - p_1^{(0)}$ and $p_1 + p_2 = 1$, we have

$$p_1^{(0)} = \frac{1 - \delta p^{(0)}}{2} \tag{1.57}$$

and

$$\frac{dp_1^{(0)}}{d\Delta} = -\frac{1}{2} \frac{d\delta p^{(0)}}{d\Delta}. \tag{1.58}$$

Using $\delta p^{(0)} = \tanh(E/2k_BT)$ and $E = \sqrt{\Delta^2 + \Delta_0^2}$, we have

$$\frac{d\delta p^{(0)}}{d\Delta} = \frac{\Delta}{2Ek_BT} \mathrm{sech}^2 \left(\frac{E}{2k_BT} \right). \tag{1.59}$$

Combining Eqs. 1.56, 1.58 and 1.59, we have[3]

$$M_{rel} = \frac{M_{rel}(0)}{1 + i\omega\tau} \tag{1.60}$$

$$= -\frac{n\gamma^2}{4k_BT} \left(\frac{\Delta}{E} \right)^2 \mathrm{sech}^2 \left(\frac{E}{2k_BT} \right) \frac{1}{1 + i\omega\tau}. \tag{1.61}$$

In order to determine the total contribution to the modulus due to the relaxational interaction, Eq. 1.61 must be integrated over the distribution of TLS. However, it is interesting to determine the asymmetry Δ and tunneling amplitude Δ_0 of the TLS that contribute the most to the relaxational modulus. To do so, it is useful to write Eqs. 1.23 and 1.61 in dimensionless units $x = E/k_BT$ and

[3]The expression for $M_{rel}(0)$ here differs from that in [11] by a factor of -4. The factor of four may arise from a tensor average used implicitly in [11] to reduce the tensor modulus in Eq. 1.53 to a scalar. My calculation of a negative $M_{rel}(0)$ must be correct since relaxation of defects can only lead to a decrease in the stress for a given strain at zero frequency.

$y = \Delta/E$. Then Eq. 1.23 becomes

$$\tau^{-1} = \frac{a}{k_B^3}\Delta_0^2 E \coth(E/2k_BT) \tag{1.62}$$

$$= \frac{a}{k_B^3}\left[1 - \left(\frac{\Delta}{E}\right)^2\right] E^3 \coth(E/2k_BT) \tag{1.63}$$

$$= \frac{a}{k_B^3}(1-y^2)E^3 \coth(x/2), \tag{1.64}$$

where

$$\frac{a}{k_B^3} = \frac{\gamma^2}{2\pi\rho\hbar^4 v^5} \tag{1.65}$$

is the prefactor of the TLS relaxation rate. Eliminating E in favor of x in Eq. 1.64, we have

$$\tau = \frac{\tanh(x/2)}{a(1-y^2)x^3T^3}. \tag{1.66}$$

From Eq. 1.61 we have

$$M_{rel} = -\frac{n\gamma^2}{4k_BT} y^2 \mathrm{sech}^2\left(\frac{x}{2}\right) \frac{1}{1+i\omega\tau}. \tag{1.67}$$

Substituting Eq. 1.66 into Eq. 1.67 and defining $c \equiv \omega/aT^3$ we have

$$M_{rel} = -\frac{n\gamma^2}{4k_BT} \frac{y^2 \mathrm{sech}^2\left(\frac{x}{2}\right)}{1 + ic\frac{\tanh(x/2)}{(1-y^2)x^3}}. \tag{1.68}$$

Fig. 1.6 shows contour plots of the magnitudes of the real and imaginary parts of $4k_BM_{rel}/n\gamma^2$ as a function of x and y for a driving strain at 10 kHz, temperatures of 1 mK, 10 mK and 100 mK, and phonon-driven relaxation rate prefactor $a = 9 \times 10^7$ K^{-3} sec^{-1}. This value of a was derived from my measurements on SiO_2, as will be shown later in this dissertation. The constant c is much larger than unity at 1 mK and 10 mK, which explains why there is not much variation in the coordinates of the dominant response for these two temperatures (i.e. the response differs only by an overall scale). It is typically claimed that the response is dominated by thermal tunneling states, where "thermal" means that

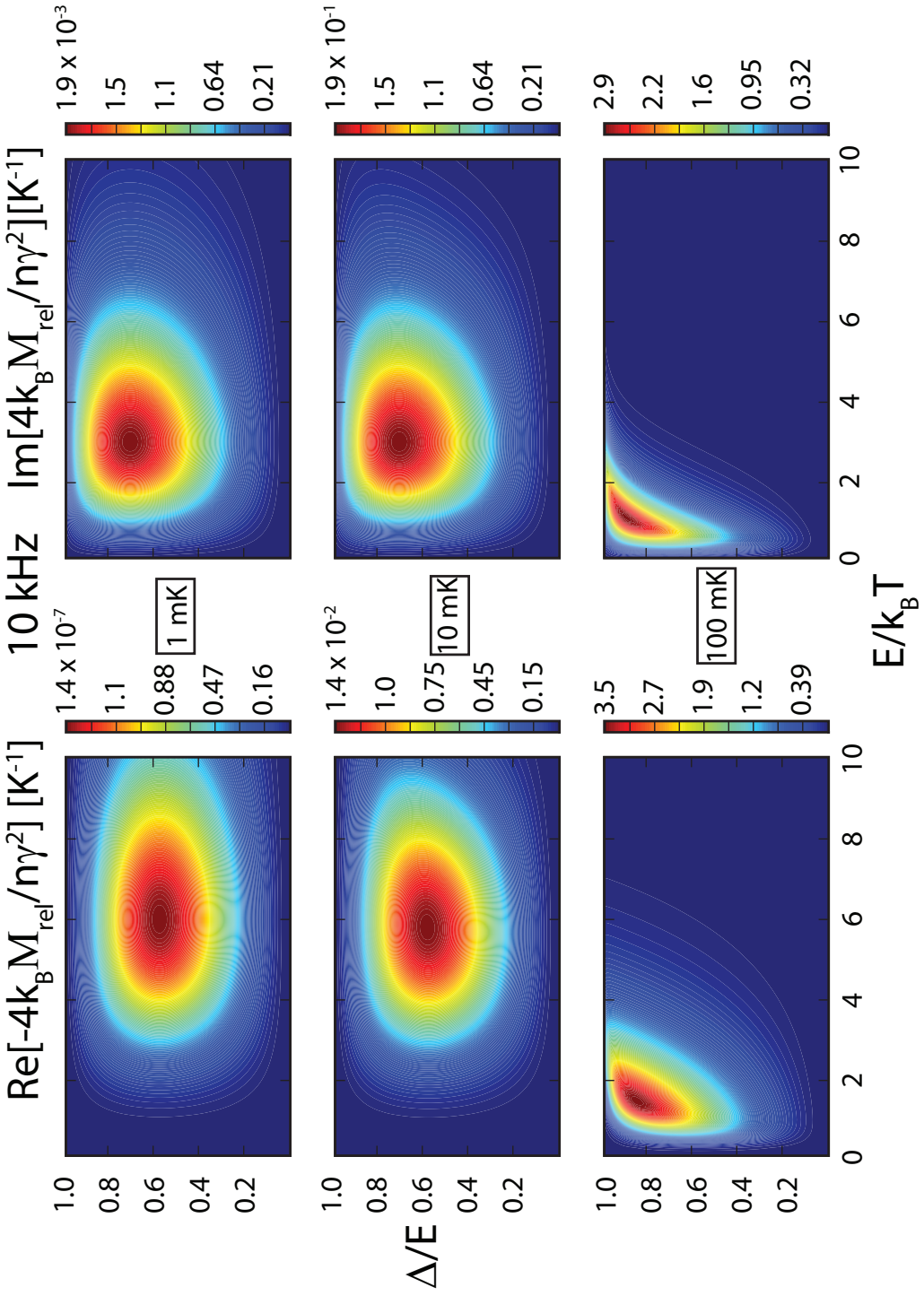

Figure 1.6: Plots of the relaxational response of TLS (Eq. 1.68) as a function of energy splitting E and asymmetry Δ at 10 kHz and three different temperatures.

the TLS energy splitting is equal to k_BT. This is ambiguous, however, because the asymmetry of the tunneling state is also important for determining the response. Fig. 1.6 shows that at 100 mK, the response is indeed dominated by TLS with $E = k_BT$. Furthermore, the response is peaked at $\Delta/E \approx 0.9$, which means that $\Delta_0 \approx \Delta/2$. Since the TLS distribution given by Eq. 1.4 diverges at small Δ_0, there should be many TLS with Δ many orders of magnitude larger than Δ_0. Thus the states with $\Delta_0 \approx \Delta/2$ can be considered small asymmetry states, and the response at 100 mK and 10 kHz is dominated by thermal tunneling states with small asymmetry [28].

One can consistently define a crossover temperature near 100 mK. Since a certain type of TLS dominates the response at 100 mK and 10 kHz, there is a well defined TLS relaxation rate at this temperature and frequency. It will be shown in the results section that there is a change in the temperature dependence of the acoustic properties near this temperature and at each of the experimental frequencies. This change in temperature dependence is expected to occur at the temperature T_{CO} that satisfies

$$\tau^{-1}(\Delta_0 = E = T_{CO}) = \omega_0, \tag{1.69}$$

i.e. the relaxation rate of the dominant TLS equals the excitation frequency. Using Eq. 1.23, the crossover temperature is

$$T_{CO} = \left(\frac{2\pi\hbar^4\rho\omega_0 v^5}{\coth(1/2)3\gamma^2 k_B^3} \right)^{1/3} \tag{1.70}$$

1.3.2 Experimental Observables In Terms of Moduli

The resonant frequency and internal friction of a mechanical resonator can be obtained from the poles of the dynamical susceptibility [29]. However, the fol-

lowing relations that follow from the wave equation are simpler to derive and relate the modulus directly to the relative change in sound speed, which is traditionally the quantity of experimental interest in the study of amorphous solids. Since we are considering an isotropic medium, the argument follows Chapter 6 of [30]. In the mechanical resonator experiments to be discussed later in this dissertation, standing waves occur due to the interference of traveling waves. Due to the isotropy of the medium, all directions of wave propagation are equivalent, and only a change in polarization of the wave can lead to a change in the elastic properties. Substituting into the wave equation a plane wave proportional to $e^{i(\omega t - kz)}$ (for an arbitrary choice of propagation in the positive z direction), the dispersion relation

$$\omega/k_t = \sqrt{M_{yzyz}/\rho} \tag{1.71}$$

is obtained for transverse waves and the relation

$$\omega/k_l = \sqrt{M_{xxxx}/\rho} \tag{1.72}$$

is obtained for longitudinal waves, where M_{yzyz} and M_{xxxx} are given by Eq. 1.54. Again neglecting the tensor nature of the modulus (there is some discussion of the similarity of the tensor components in Section 1.2.1), the phase speed ω/k is

$$v = \sqrt{\frac{M_1}{\rho}} \tag{1.73}$$

and

$$dv = \frac{1}{2}\sqrt{\frac{\rho}{M_1}}\frac{dM_1}{\rho} = \frac{1}{2}\frac{dM_1}{\rho v} \tag{1.74}$$

where M_1 (M_2) is the real (imaginary) part of the modulus. Thus the relaxational contribution to $\delta v/v_0$ is

$$\left(\frac{\delta v}{v_0}\right)_{rel} = \frac{1}{2}\frac{\langle M'_{rel}\rangle}{\rho v^2}, \tag{1.75}$$

where $M'_{rel} = \mathrm{Re}[M_{rel}]$ and the pointed brackets correspond to an average over the TLS distribution from Eq. 1.4. The internal friction is equal to the loss angle

$$Q^{-1} = \frac{M_2}{M_1}. \tag{1.76}$$

As defined in Eq. 1.38, the modulus consists of a sum of three parts, and the real part is dominated by the non-TLS contribution ρv^2. The relaxational contribution to Q^{-1} is thus given by

$$Q_{rel}^{-1} = \frac{\langle M''_{rel} \rangle}{\rho v^2}, \tag{1.77}$$

where $M''_{rel} = \mathrm{Im}[M_{rel}]$ and the pointed brackets correspond to an average over the TLS distribution from Eq. 1.4.

1.3.3 Resonant Response

The phonon scattering rate due to TLS is given by Eq. 1.36. The corresponding contribution to the internal friction is given by

$$Q_{res}^{-1} = \frac{\tau_{ph}^{-1}}{\omega} = \pi C \tanh \frac{\hbar\omega}{2k_B T}. \tag{1.78}$$

We note that $10^{-4} < C < 10^{-3}$ for almost all dielectric glasses (see [31] for the exception of high stress glass). Thus at kHz frequencies and mK temperatures, the resonant contribution to the internal friction is quite small. It will turn out to be negligible compared to the relaxational contribution in my experiments.

We can get the resonant contribution to $\delta v/v_0$ from the phonon mean free path $l = v\tau_{ph}$ via the Kramers-Kroenig relation [11]:

$$\delta v(\omega, T) = \frac{1}{\pi} \int_0^\infty \frac{v^2 l^{-1}(\omega')}{\omega^2 - \omega'^2} d\omega'. \tag{1.79}$$

If $v(T)$ is measured with respect to $T = 0$, we have

$$\left[\frac{\delta v}{v_0}\right]_{res} = \frac{v(T) - v(0)}{v(0)} = C\left[\mathrm{Re}\Psi\left(\frac{1}{2} + \frac{\hbar\omega}{2\pi \mathrm{i} k_B T}\right) - \ln\frac{\hbar\omega}{k_B T}\right], \tag{1.80}$$

where Ψ is the digamma function. Since in my experiments $\hbar\omega << k_B T$, the temperature dependence of the digamma term is negligible. Referring the sound speed measurement to some temperature T_0 such that $\hbar\omega << k_B T_0$, we have

$$\left[\frac{\delta v}{v_0}\right]_{res} = \frac{v(T) - v(T_0)}{v(T_0)} = C\ln(T/T_0). \tag{1.81}$$

1.3.4 Summary of Low Temperature Acoustic Response Predicted by the Standard Tunneling Model

As discussed above, TLS are expected to dominate the acoustic properties of amorphous solids at low temperatures. Non-TLS processes are expected to add a relatively large yet nearly temperature independent contribution to the sound speed and a relatively small contribution to the internal friction. The contributions from TLS processes can be divided into resonant and relaxational processes. The former can be evaluated analytically, but the latter must be evaluated numerically. I give the asymptotic forms for the different TLS contributions to the acoustic properties in Table 1.1.

1.4 Interactions Between Two Level Systems

Because the TLS defects are part of the lattice, a change in the state of the TLS results in a change in the local strain field. Nearby TLS must then be affected

Table 1.1: Asymptotic forms of the acoustic response of a dielectric amorphous solid. A star indicates that the contribution is negligible for the experimental parameters in this dissertation. T_{CO} is the temperature at which $\omega\tau = 1$ for the dominant tunneling states (Eq. 1.70). See text for a discussion of which tunneling states are dominant, as well as a definition of other constants in the table.

Interaction	**Quantity**	$\mathbf{T << T_{CO}}$	$\mathbf{T >> T_{CO}}$
Resonant	$\frac{\delta v}{v_0}$	$C\ln(\frac{T}{T_0})$	
Relaxational	$\frac{\delta v}{v_0}$	*	$-\frac{3}{2}C\ln(\frac{T}{T_0})$
Resonant	Q^{-1}	*	
Relaxational	Q^{-1}	$\frac{\pi^4}{12\omega}CaT^3$	$\frac{\pi}{2}C$

by this perturbation in the strain field to some extent. The first evidence for interactions between TLS came from spectral diffusion and anomalously low dephasing times in echo experiments as discussed in Chap. 5 of [32] and references therein. By applying intense acoustic pulses, the resonant contribution to the internal friction can be saturated; this is called "hole burning". However, because of interactions between TLS, the energy splittings of the TLS are constantly fluctuating, which indicates that the hole in the energy spectrum decays more quickly than expected from relaxation due to phonons. This is spectral diffusion. TLS interactions also decrease the dephasing time in echo experiments. Using the NMR analogy, the decay of the resonant signal is dominated by the spin-spin relaxation time rather than the spin-lattice relaxation time.

In the explanation for spectral diffusion, the energy of a given TLS fluctuates due to interactions with nearby TLS. However, interactions between TLS in the environment of the given TLS are neglected. According to Burin [32], such interactions are important at very low temperatures and lead to interaction-driven relaxation that is faster than phonon-driven relaxation. In this picture, pairs of

TLS form new effective TLS, and these pair TLS have a distribution of TLS parameters Δ_p and Δ_{0p} that differs from the distribution of ordinary TLS in Eq. 1.4. Most importantly, the distribution of pair TLS $P_2 \propto 1/\Delta_{0p}^2$, so that the density of pair TLS with small pair tunneling amplitude Δ_{0p} is enhanced over that of ordinary TLS with small tunneling amplitude Δ_0. Thus the pair TLS can form delocalized clusters that lead to thermal relaxation of ordinary TLS, whereas ordinary TLS cannot form such delocalized clusters. The interaction between TLS pairs leads to a TLS relaxation rate that is linear in temperature, as opposed to the cubic temperature dependence for phonon-driven relaxation of symmetric thermal TLS (Eq. 1.23). At sufficiently low temperatures, the interaction-driven relaxation rate should be dominant.

I now discuss in more detail the derivation of the interaction-driven relaxation. The argument is based on Chap. 5 of [32]. First Burin considers the Hamiltonian for an isolated pair of TLS. He neglects the contribution of the phonon bath, although he includes the interaction between the two TLS, which is mediated by virtual phonons. In the position basis, the interaction term of the Hamiltonian is given by $-U_{12}S_1^zS_2^z$, where S_i^z is a spin operator. The interaction factor is given by $U_{12} = U_0/R_{12}^3$. The $1/R^3$ dependence is because the TLS are like interacting dipoles. The position independent contribution is given by $U_0 \approx \gamma^2/\rho v^2$, and is derived from strain tensors on p. 237-8 of [32]. It is convenient to switch to the eigenbasis of the single TLS Hamiltonians so that the contribution of the interaction term can be treated as a perturbation and the tunneling amplitude $\Delta_{0,p}$ can be calculated according to perturbation theory.

Then the total Hamiltonian for the isolated pair of TLS becomes

$$H_{pair} = -E_1 S_1^z - E_2 S_2^z - U_{12} \times \tag{1.82}$$

$$\left[\frac{\Delta_1\Delta_2}{E_1E_2}S_1^zS_2^z - \frac{\Delta_{01}\Delta_2}{E_1E_2}S_1^xS_2^z - \frac{\Delta_1\Delta_{02}}{E_1E_2}S_1^zS_2^x + \frac{\Delta_{01}\Delta_{02}}{E_1E_2}S_1^xS_2^x\right] \tag{1.83}$$

Although there are four eigenstates of this Hamiltonian, the states $|{+}{+}\rangle$ and $|{-}{-}\rangle$ are well separated in energy from the states $|{+}{-}\rangle$ and $|{-}{+}\rangle$ and thus weakly coupled to them. Thus only transitions between the latter pair of states are considered. In such transitions, the first three terms in square brackets in Eq. 1.83 are negligible. Comparing the remaining terms with the Hamiltonian for a single TLS leads to the definition of the pair TLS parameters:

$$\Delta_p = E_1 - E_2 \tag{1.84}$$

$$\Delta_{0p} = \frac{1}{2}U_{12}\frac{\Delta_{01}\Delta_{02}}{E_1E_2}. \tag{1.85}$$

As shown in Chap. 5 of [32], the distribution of these parameters is

$$P_2(\Delta_p, \Delta_{0p}) = \frac{\pi^3}{12}P_0^2U_0k_BT\frac{1}{\Delta_{0p}^2}\Theta(k_BT - \Delta_{0p})\Theta\left(\Delta_{0p} - U_0\left(\frac{k_BT}{\hbar v}\right)^3\right). \tag{1.86}$$

1.4.1 Probability of Two Level System Resonant Pairs

Burin then derives the probability W_2 for a given TLS with energy splitting E and tunneling amplitude Δ_0 to find a resonant pair with energy splitting E_2 and tunneling amplitude Δ_{02} in the coherent region and shows that it is very small. This is analogous to Anderson localization. Here resonance means that the matrix element Δ_{0p} for the transition under consideration is greater than the difference in the energy splittings of TLS in the pair, Δ_p. The coherent region refers to that region surrounding the given TLS in which the interaction energy is greater than the energy corresponding to the phonon-driven relaxation rate

of the TLS. The phonon driven relaxation rate drops off as T^3, so the coherent region gets bigger as temperature decreases.

Here I explicitly evaluate the integral expression for W_2 since that is not done in Chap. 5 of [32]. We thus have

$$W_2 = \int_{R_0}^{R_c} \int_{E}^{E+\Delta_{0p}} \int_{0}^{E_2} P(\Delta_{02}, E_2) d\Delta_{02} dE_2 d^3R \tag{1.87}$$

where the volume integral is restricted by the coherent radius R_c. The lower limit on the volume integral comes from the restriction that the interaction energy Δ_{0p} should be less than the temperature. Since TLS with $\Delta_p < \Delta_{0p}$ dominate, we can take the energy splitting of the pair $\approx \Delta_{0p}$. Thus if $\Delta_{0p} > T$, the TLS pair is unlikely to be in the excited state. Since Δ_p is small compared to the single TLS energy splittings, we can replace E_2 with E in the integration limit. Also substituting in the TLS distribution yields

$$W_2 = P_0 \int_{R_0}^{R_c} \int_{0}^{E} \frac{1}{\Delta_{02}} \int_{E}^{E+\Delta_{0p}} \frac{E_2}{\sqrt{E_2^2 - \Delta_{02}^2}} dE_2 d\Delta_{02} d^3R \tag{1.88}$$

$$= P_0 \int_{R_0}^{R_c} \int_{0}^{E} \frac{1}{\Delta_{02}} \frac{E\Delta_{0p}}{\sqrt{E^2 - \Delta_{02}^2}} d\Delta_{02} d^3R \tag{1.89}$$

$$= P_0 \int_{R_0}^{R_c} \int_{0}^{E} \frac{1}{\cancel{\Delta_{02}}} \frac{\cancel{E}}{\sqrt{E^2 - \Delta_{02}^2}} \frac{1}{2} U_{12} \frac{\Delta_0 \cancel{\Delta_{02}}}{\cancel{E} E_2} d\Delta_{02} d^3R \tag{1.90}$$

where I have substituted Δ_{0p} from Eq. 1.85. Using

$$\int_{0}^{E} \frac{d\Delta_{02}}{\sqrt{E^2 - \Delta_{02}^2}} = \frac{\pi}{2} \tag{1.91}$$

we have

$$W_2 = \frac{\pi}{4} P_0 U_0 \int_{R_0}^{R_c} \frac{\Delta_0}{R^3 E_2} d^3R \tag{1.92}$$

$$= \frac{\pi}{4} P_0 U_0 \frac{\Delta_0}{E} \int_{R_0}^{R_c} \frac{1}{R^3} R^2 dR d\theta d\phi \tag{1.93}$$

$$= \pi^2 P_0 U_0 \frac{\Delta_0}{E} \ln\left(\frac{R_c}{R_0}\right) \tag{1.94}$$

where we have again used $E_2 \approx E$. The coherent radius R_c is determined by the condition that the TLS interaction energy equals the energy $\hbar\tau^{-1}$ associated with the phonon-driven relaxation rate. Thus

$$R_c = \left(\frac{U_0}{\hbar\tau^{-1}}\right)^{1/3} \tag{1.95}$$

The length R_0 is determined by setting the interaction energy equal to the temperature. Thus

$$R_0 = \left(\frac{U_0}{k_B T}\right)^{1/3}. \tag{1.96}$$

We then have

$$W_2 = \frac{\pi^2}{3} P_0 U_0 \frac{\Delta_0}{E} \ln\left(\frac{k_B T}{\hbar\tau^{-1}}\right). \tag{1.97}$$

The quantity $P_0 U_0 = C$ is the tunneling strength, which satisfies $10^{-4} < C < 10^{-3}$ for nearly all amorphous solids [1]. As will be shown later in this dissertation, $\tau^{-1} \approx 10^8$ K^{-3}sec$^{-1}T^3$, which implies that the logarithmic factor in Eq. 1.97 ≈ 30 at 1 mK. Thus, according to Eq. 1.97, W_2 is very small and it is unlikely that a delocalized cluster of resonant, coherent TLS would form.

1.4.2 Probability of Two Level System Resonant Triples

In [33], Burin computes W_3, the probability for a resonant triple of TLS in the coherent region. The procedure is analogous to that for calculating W_2. For an isolated triple of TLS the Hamiltonian is

$$H_{triple} = H_{0t} + U_t \tag{1.98}$$

$$= -\sum_{i=1}^{3} E_i S_i^z - \frac{1}{2}\sum_{i,j=1}^{3} U_{ij} \frac{\Delta_i S_i^z - \Delta_{0i} S_i^x}{E_i} \frac{\Delta_j S_j^z - \Delta_{0j} S_j^x}{E_j}. \tag{1.99}$$

As with the pairs, Burin considers transitions in which all TLS change states, such as $|++-\rangle$ to $|--+\rangle$. The first order contribution to the transition matrix

element vanishes since the perturbation term in Eq. 1.99 contains only terms with two S^x factors. In the first non-vanishing order, we have for the transition matrix element

$$J_{123} = -\sum_a \frac{\langle ++-|U_t|a\rangle \langle a|U_t|--+\rangle}{E_a - E_1 - E_2 - E_3} \tag{1.100}$$

where $|a\rangle$ represents an eigenstate of the unperturbed Hamiltonian. For example, for $|a\rangle = |+-+\rangle$ we have

$$\langle ++-|U|+-+\rangle \langle +-+|U|--+\rangle \tag{1.101}$$

$$= \frac{1}{4} \langle ++-|\frac{U_{23}\Delta_{02}S_2^x\Delta_{03}S_3^z}{E_2E_3}|+-+\rangle \times \tag{1.102}$$

$$\langle +-+|\frac{U_{12}\Delta_{01}S_1^x\Delta_2S_2^z}{E_1E_2} + \frac{U_{13}\Delta_{01}S_1^x\Delta_3S_3^z}{E_1E_3}|--+\rangle \tag{1.103}$$

$$= -\frac{U_{23}}{4}\frac{\Delta_{01}\Delta_{02}\Delta_{03}}{E_1E_2E_3}\left(\frac{\Delta_2U_{12}}{E_2} - \frac{\Delta_3U_{13}}{E_3}\right) \tag{1.104}$$

From [33], after summing over all intermediate states $|a\rangle$, we have

$$J_{123} = -\frac{\Delta_{01}\Delta_{02}\Delta_{03}}{8E_1E_2E_3} \times \tag{1.105}$$

$$\left(-\frac{\Delta_1U_{12}U_{13}}{E_2E_3} - \frac{\Delta_2U_{12}U_{23}}{E_1E_3} + \frac{\Delta_3U_{13}U_{23}}{E_1E_2}\right). \tag{1.106}$$

From this expression for the transition matrix element, Burin obtains

$$W_3 \approx P_0^2U_0^2\left[\ln\left(\frac{k_BT}{\hbar\tau^{-1}}\right)\right]^2 \approx W_2^2. \tag{1.107}$$

Since we showed above that W_2 is very small, the probability of finding a resonant triple in the coherent region is also very small. However, according to [34], even if the probability W_n to find a resonant cluster of n two level systems is much less than unity, higher order terms in the perturbation series may result in relaxation. At present, there seems to be disagreement in the theoretical community on this issue.

1.4.3 Interactions Between Pairs of Effective Two Level Systems

In Chap. 5 of [32], Burin shows that the probability of resonant pairs of pair TLS appearing in the coherent region is substantial, and that this leads to thermal relaxation of single TLS. The most straightforward approach seems to be to directly evaluate the probability of pairs of pair TLS using the same approach as for pairs of single TLS:

$$W_{2,2} = \int_{R_0}^{R_c} \int_{E_p}^{E_p+\Delta_{0p}^{(2)}} \int_0^{E_{p2}} P_2(\Delta_{0p2}, E_{p2}) d\Delta_{0p2} dE_{p2} d^3R \tag{1.108}$$

where

$$\Delta_{0p}^{(2)} = \frac{U_{12}\Delta_{0p}\Delta_{0p2}}{2E_pE_{p2}}. \tag{1.109}$$

However, Burin uses a different, clever argument. He considers pairs with small asymmetry $\Delta_p < \Delta_{0p}$ that have a tunneling amplitude Δ_{0p} that is comparable to that of the individual TLS making up the pair, i.e.,

$$\Delta_0 - \Delta_0/2 < \Delta_{0p} < \Delta_0 + \Delta_0/2. \tag{1.110}$$

Thus these TLS span a spectral range of width Δ_{0p} in both Δ_p and Δ_{0p} so that their density is, using Eq. 1.86,

$$n_r \approx P_2(\Delta_p, \Delta_{0p})\Delta_{0p}\Delta_{0p} \approx \frac{\pi^3}{12} P_0^2 U_0 k_B T. \tag{1.111}$$

Note that n_r is independent of Δ_{0p} whereas the analogous density for single TLS decreases in proportion to Δ_{0p}. It is this enhancement in the density that leads to delocalization in the case of pairs of pair TLS. The density n_r determines the average separation, and thus the average interaction energy between pairs of TLS is

$$\Delta_* = U_0 n_r \approx k_B T (P_0 U_0)^2. \tag{1.112}$$

For pairs separated by a distance less than the coherent radius, and for $\Delta_{0p} < \Delta_*$, the pairs form a delocalized cluster that allows for relaxation of TLS. The transport rate of the delocalized excitations is given by $\Delta_*/\hbar$, so the number of TLS that flip per unit time is $2n_r\Delta_*/\hbar$. The interaction-driven relaxation time τ_{tr} for single TLS is defined as the time required for the density of flipped TLS to reach the density of thermal TLS

$$\tau_{tr} = P_0 k_B T \frac{\hbar}{n_r \Delta_*}. \tag{1.113}$$

Using Eqs. 1.111 and 1.112, one can see that the relaxation rate τ_{tr}^{-1} is linear in temperature. This is the most important feature of the rate τ_{tr}^{-1} since the prefactor cannot be accurately calculated with this scaling approach [35]. Thus we have

$$\tau_{tr}^{-1} = bT, \tag{1.114}$$

where the prefactor, b, is left as a fitting parameter in the experimental sections of this dissertation.

CHAPTER 2

EXPERIMENTAL METHODS

2.1 Cryostat

Measurements included in this dissertation were made on the cryostat in H-13 Clark. This cryostat is a model 420 SHE dilution refrigerator with a combination copper/$PrNi_5$ demagnetization stage that is described in detail in [36]. The base temperature of the dilution stage was about 7 mK.

The theory of cooling by adiabatic demagnetization is discussed in [27]. In this implementation, a superconducting magnet with a maximum current of 65 A, corresponding to a maximum field of ≈ 7.2 T, is used to polarize the nuclear spins in the copper/$PrNi_5$ bundle. A large heat of magnetization is released, the heat capacity of the demag stage is greatly increased, and a couple of days are required for the dilution stage to cool the demag stage back to the base temperature. Once the demag stage is equilibrated near 7 mK, a tin superconducting heat switch is allowed to enter the superconducting state so that heat conduction between the mixing chamber and the demag stage is only via phonons and thus very small.

In order to understand cooling by nuclear demagnetization, it is easiest to first consider the ensemble of spins in isolation from the electrons and phonons. Thus the heat flowing into the nuclear spin ensemble is zero and from

$$dQ = TdS \tag{2.1}$$

the entropy of the nuclear spin ensemble is constant. If the magnetic field is then decreased, the only way that the polarization of the spins can be maintained

is for the temperature to decrease. More precisely, the field and temperature dependence of the entropy of a magnetic spin system with spin I [36] appears only as B/T. With constant entropy, we then have a linear dependence of the temperature on the field:

$$T = B\frac{T_0}{B_0}, \tag{2.2}$$

where T_0 and B_0 are the initial temperature and field. Note that a contribution to the magnetic field acting on a nuclear spin comes from the magnetic moments of neighboring nuclear spins. This internal field $B_{int} \approx 0.066T$ [36]. Interestingly, Eqs. 2.1 and 2.2 imply that the temperature of the nuclear spin system is lowered without removing any heat from the spin system.

In reality, the coupling between the nuclear spin system and the electrons of the demag stage is strong enough so that the spin system is not completely isolated and it possible cool the experimental sample. Yet Eq. 2.2 still allows one to determine the field corresponding to a desired temperature rather accurately because the heat flowing into the spin ensemble in the demag bundle is small. This heat is due to the heat capacity of the rest of the fridge and heat leaks. The heat leaks are either time dependent or magnetic field dependent. The time dependent heat leak decreases over time and is thought to be due to relaxation of two level systems [32]. The field dependent contribution is from eddy current heating due to vibrations of the demag bundle in the field gradient or intentional changes in the field strength [36].

Due to the combined contributions of the Cu and $PrNi_5$, the total heat capacity of the demag stage is large and nearly independent of B/T over a rather wide range [36]. Nonetheless, it was sometimes useful to slowly reduce the field

so as to cancel the change in temperature due to the heat leak. Since

$$\frac{dT}{dt} = \frac{T_0}{B_0}\frac{dB}{dt} + \frac{\dot{Q}}{C\left(\frac{B}{T}\right)}, \tag{2.3}$$

where $\dot{Q}$ is the heat leak to the demag stage, we must have

$$\frac{T_0}{B_0}\frac{dB}{dt} = -\frac{\dot{Q}}{C\left(\frac{B}{T}\right)} \tag{2.4}$$

for a stable temperature. Since T_0/B_0 will gradually increase as entropy flows into the nuclear spin system, one must gradually decrease dB/dt, assuming a constant heat capacity and heat leak.

The "cooling power" of the demag stage is somewhat ambiguous. Since the cooling by nuclear demagnetization used here is a "single-shot" rather than a continuous process, it perhaps makes more sense to consider the "cooling energy". The cooling energy is related to the removed entropy by Eq. 2.1, and at constant temperature it is proportional to the temperature,

$$\Delta Q = -T\int_{S(B_{int}/T)}^{S(B_i/T)} dS = T[S(B_{int}/T) - S(B_i/T)] \tag{2.5}$$

where ΔQ is the total heat absorbed by the spin system, bringing its entropy from the initial value $S(B_i/T)$ to the final value $S(B_{int}/T)$. The magnetic field is decreased from the initial value B_i to a final value B_{int} (determined by the mean field due to the spins) in order to hold the temperature constant as heat is absorbed by the spin system. For a constant temperature T =1 mK and an initial field to temperature ratio of 1 T/mK, corresponding to a removed entropy of about 7 J/K [36], the cooling energy is 7 mJ.

2.2 Melting Curve Thermometry

^{3}He melting curve thermometry was used for the measurements on SiO_2 presented in this dissertation. The position of the melting curve thermometer on the demag stage is shown in Fig. 2.1. The melting curve thermometer (MCT) is a sensitive capacitive pressure transducer known as a Straty-Adams gauge [37] that is used to measure the pressure of a ^{3}He sample. The pressure is converted to temperature according to the melting curve interpolation in [38]. One wall of the ^{3}He sample region is a flexible diaphragm, which actuates a mobile capacitor plate outside the sample region. Displacement of the diaphragm due to changes in the ^{3}He sample pressure thus modulates the capacitance. The mobile plate and a fixed plate form a parallel plate capacitor. The capacitance of the MCT was measured with an Andeen-Hageling 2500A digital capacitance bridge. A metal sinter fills part of the sample chamber in order to provide a large surface area and decrease the thermal boundary resistance between the ^{3}He and the cold finger. The fraction of the ^{3}He sample on the melting curve that is solid is given in [39] for different starting pressures in the liquid phase. If too low a starting pressure is used, the ^{3}He sample comes off the melting curve and into the liquid phase at the lowest temperatures. If too high a starting pressure is used the volume required by the solid becomes larger than the bulk volume in the sample chamber and the ^{3}He solid must form in the sinter, resulting in a modification of the melting curve [39]. I used a starting pressure of 510 psi (≈ 35 bar), and I tried to maintain this pressure as the fridge cooled and the ^{3}He contracted. The fill line for the MCT is heat sunk in several places, and a solid block in the fill line forms at some point, thus sealing the ^{3}He sample region.

In order to determine the pressure-capacitance calibration, the MCT ^{3}He chamber was connected to a room temperature Paroscientific pressure transducer. It was necessary to calibrate the MCT at $T < 4$K (but above the temperature at which the block in the fill line forms) to avoid temperature dependent errors. The capacitance bridge and the counter connected to the Parosci output were both set to average for four seconds, and a LabView program was used to read out the capacitance and the Parosci period synchronously. The pressure was cycled between 390 and 510 psi in order to span the relevant pressure range bounded by the melting curve minimum at ≈ 420 psi and the solid transition at ≈ 500 psi. Some hysteresis was observed in the pressure cycles, and it was not possible to eliminate the hysteresis by doing more pressure cycles. For small displacements of the diaphragm, the pressure, p, was expected to depend on the capacitance, C, as $P = A + B/C + D/C^2$, where A, B, and D are fit parameters. A typical uncertainty in the pressure calibration was 2 mbar, which corresponds to 70 μK at the lowest temperatures, at which precision is most important and the slope of the melting curve ≈ 30 mbar/mK.

2.3 $Si0_2$ Double Paddle Resonator Specimen

The development of the initial double paddle resonator geometry was reported in [40]. The mechanical resonator and electrode structure discussed in this dissertation were fabricated by the Heidelberg group. Photos of the resonator and electrodes are shown in Fig. 2.2 and a sketch of the resonator showing the geometry with parts labeled and the length scale is shown in Fig. 2.3. The resonator was laser cut from a 400 micron thick wafer of Suprasil 300 with a double paddle resonator (DPR) geometry. This type of silica is very pure and the OH content

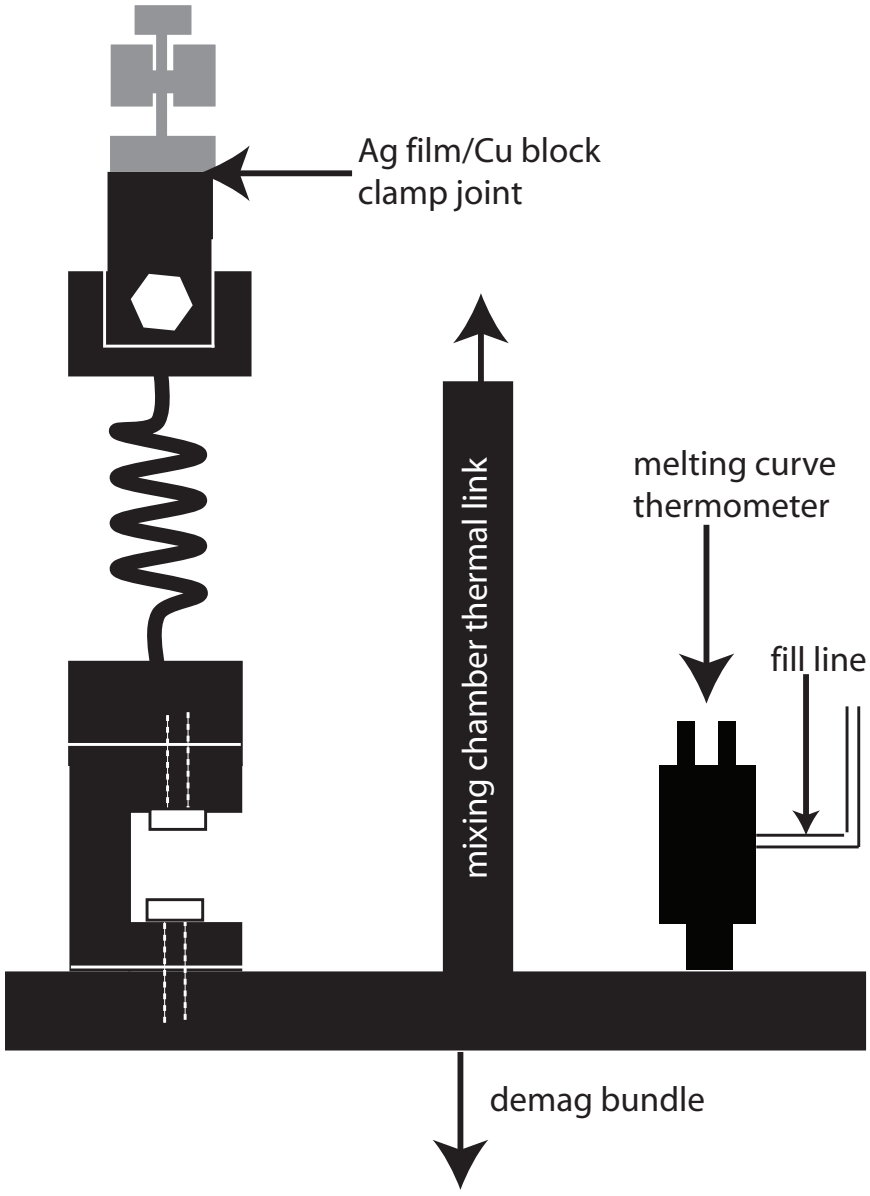

Figure 2.1: Arrangement of components on the demag stage, demonstrating the thermal paths.

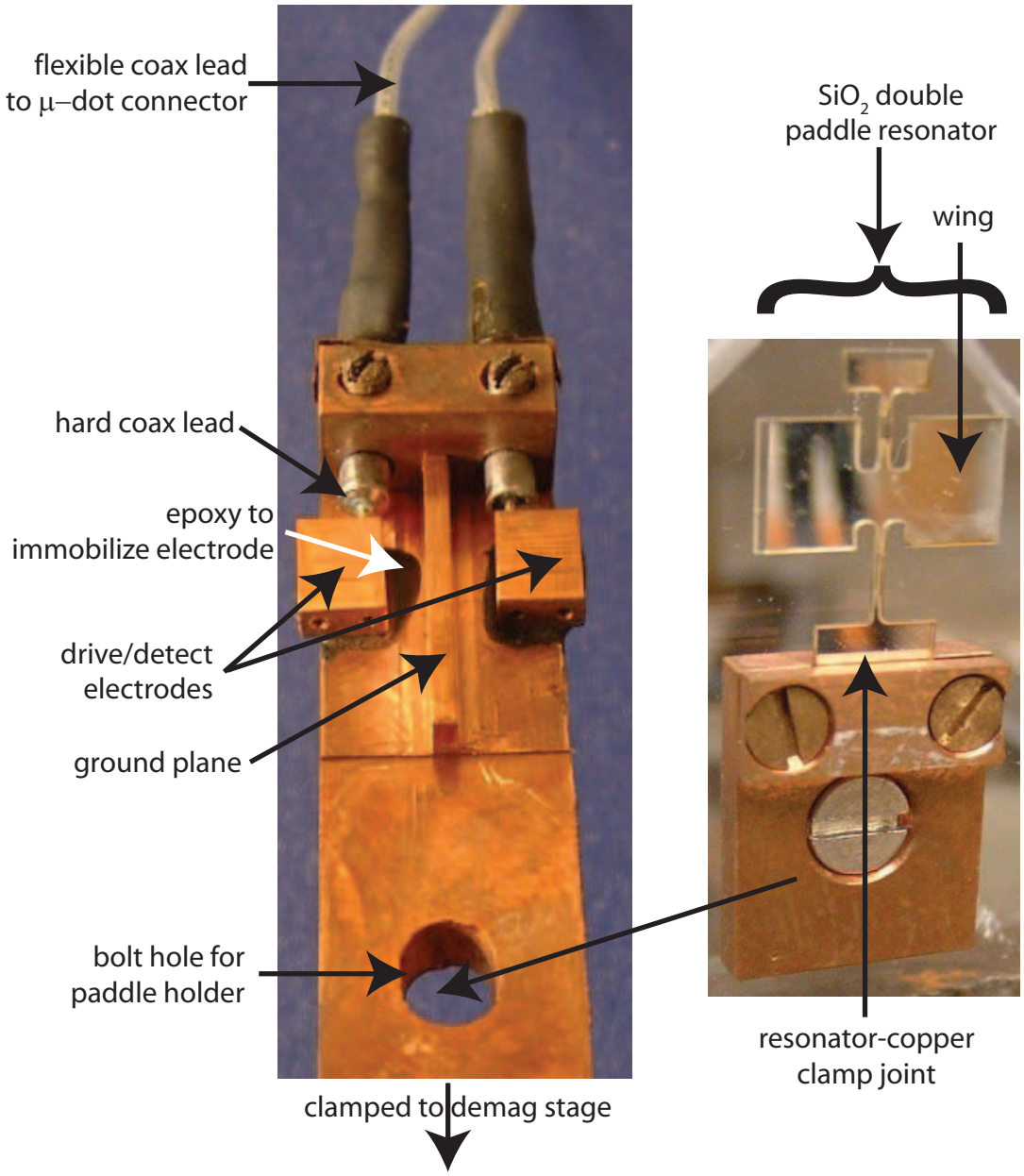

Figure 2.2: Electrode structure and double paddle resonator. The $Si0_2$ resonator is reflective due to the silver coating on the back side. Each electrode is capacitively coupled to the Ag film covering the "wings" of the resonator.

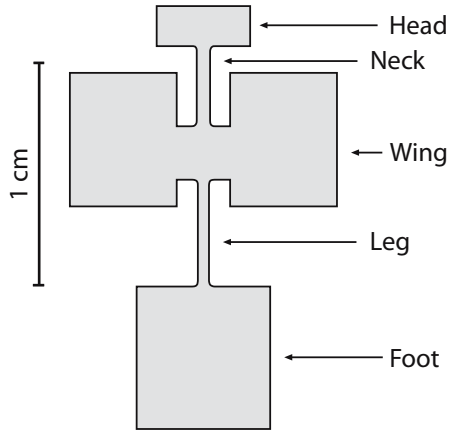

Figure 2.3: Geometry and size of the double paddle resonator, with labeled "anatomy". Figure from [3].

at less than 1 ppm is particularly low. It also has 1500 ppm Cl. It is important to use a pure glass because the impurities may have their own excitations that can be difficult to distinguish from the SiO_2 TLS. The SiO_2 resonator discussed in this dissertation is very similar to that in [3] and the small resonator in [4]. The DPR was coated with an Ag film so that it could be excited electrostatically and to aid in thermalization. The one micron thickness of the Ag film was chosen so that its thermal conductivity was sufficiently high while the film was sufficiently thin so as to negligibly affect the total dissipation of the DPR. During the later set of measurements presented in this dissertation, a copper coil vibration isolator as shown in Fig. 2.1 was used. Sound speed data taken with the additional vibration isolator was slightly different than earlier data that was taken without it, but this small difference turned out to be insignificant.

A finite element method (FEM) calculation showed that there are several different mode shapes for the resonator. Only certain modes can be excited and detected using the electrode geometry shown in Fig. 2.2. The mode excitation is determined by both the placement of the electrodes and the frequency of ex-

citation.

2.4 Electronics

Several different modes of operation are possible for acoustic experiments using mechanical resonators, including the frequency sweep, ringdown, and phase locked loop techniques. In the constant amplitude phase locked loop technique the controller modifies the drive amplitude and drive frequency to maintain a constant response amplitude and a constant phase shift from resonance. Although this method in principle allows one to collect data most efficiently, it was not viable for the measurements on SiO_2 because it was important to operate at very low strains to remain in the linear regime. At such low strains, the signal to noise ratio was not high enough for the controller to maintain a phase lock. Instead, most of the measurements were made using the frequency sweep technique, in which we used $\delta v/v_0 \approx (f_\mathrm{r} - f_{\mathrm{r},0})/f_{\mathrm{r},0}$ (assuming negligible thermal expansion) and $Q^{-1} = \Delta f/f_\mathrm{r}$, where f_r is the frequency at peak response and Δf is the half-power width. Ideally $f_{\mathrm{r},0} = f_\mathrm{r}(T = 0)$, and any small difference amounts to an offset in $\delta v/v_0$, which is not of interest here.

The circuit that was used for the frequency sweep measurements is shown in Fig. 2.4. The LabView program allowed one to set a drive level, an initial frequency, a final frequency, the number of points to acquire, and the time delay that allowed time for the transients to decay at each new frequency. The LabView program would initially set the function generator drive amplitude. For each of the selected frequencies, the LabView program would then set the drive frequency and query the lockin amplifier for the response. The parameters were

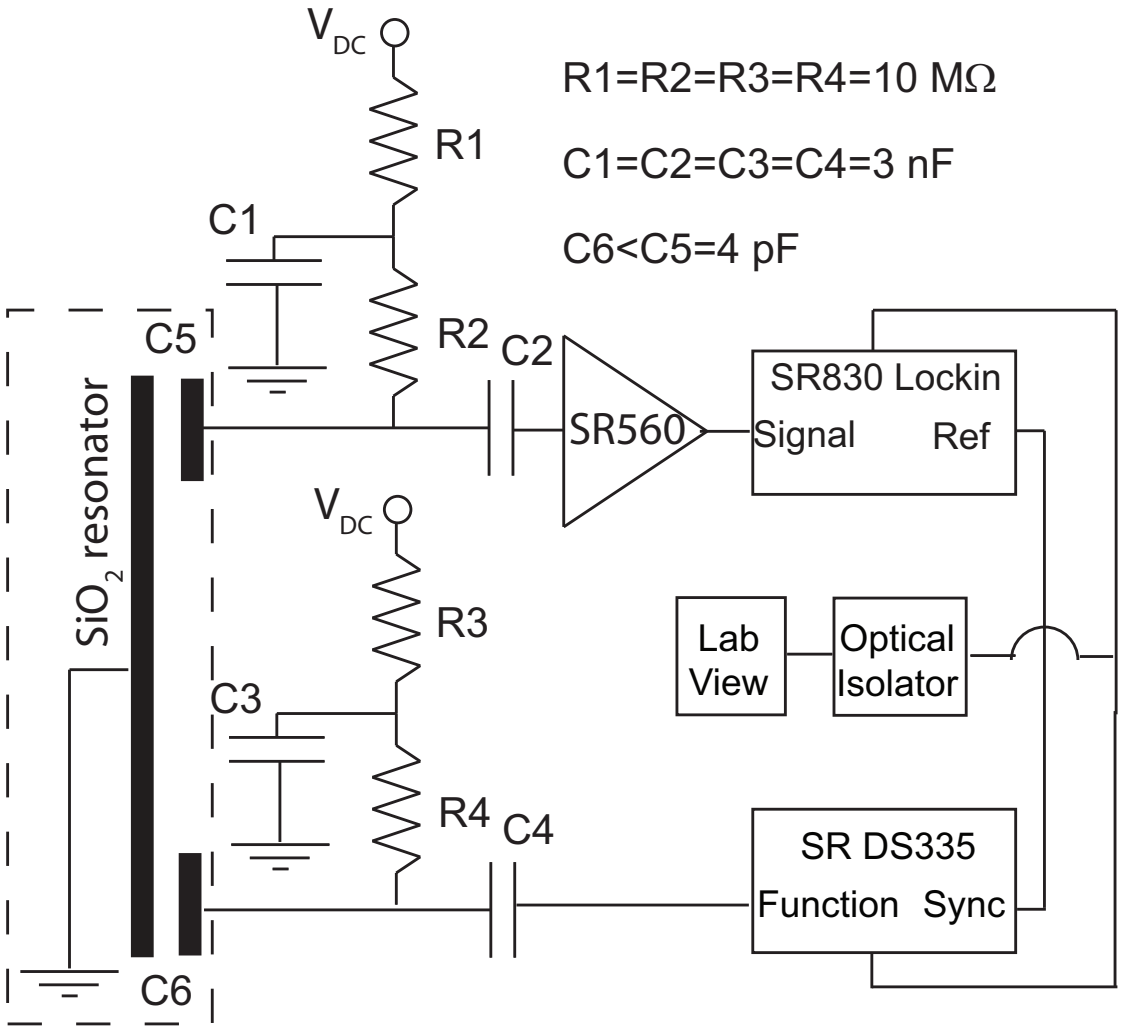

Figure 2.4: Electronic circuit for drive and detection of $Si0_2$ resonator motion. Components outside the dashed box are at room temperature.

chosen so that errors due to sweep speed and drive amplitude were negligible.

I now describe in detail the drive and detect portions of the circuit. The fixed electrodes and the Ag film on the paddle form two parallel plate capacitors, labeled C5 and C6 in Fig. 2.4. The electric field between the two plates of capacitor C6 acts on the charge collected on the outer surface of the silver film near the fixed electrode, resulting in a force density $f = \sigma^2/2\epsilon_0$ [41] that

draws the paddle wing towards the fixed electrode, where σ is the areal charge density. Thus the force on the DPR is proportional to the square of the voltage across C6. One way of driving the oscillator is to use a purely AC drive voltage. The driving force is then at twice the frequency of the driving voltage, which is convenient in the sense that spurious signals due to capacitive coupling between drive and detect electrodes are easily removed with the lockin. However, because it was possible to digitally remove the crosstalk signal, we added to the AC voltage a relatively large DC voltage. Then the force on the DPR was given by $F \propto (V_{DC} + V_{AC})^2 = V_{DC}^2 + V_{AC}^2 + 2V_{DC}V_{AC}$. Since $V_{DC} >> V_{AC}$, the term V_{AC}^2 is negligible, and the term V_{DC}^2 amounts to a static force that only shifts the resonant frequency of the mode of interest. The dominant force term $2V_{DC}V_{AC}$ is linear in the AC drive voltage and oscillates at the same frequency as the AC drive voltage. The coupling capacitor C4 along with the input resistance of the function generator forms a high pass filter that blocks the voltage V_{DC} from the function generator. R3 and C3 form a low pass filter that prevents the voltage source V_{DC} from compensating for the fluctuating voltage due to the function generator. R3 and R4 also limit the current from V_{DC} in case of an arc between the plates of C6. R4 is present absorb the energy stored on C3 in case of an arc.

The functions of the elements in the bias network on the detect side are analogous to the functions of those on the drive side. The impedance between capacitor C5 and equipotential reservoirs is high enough so that the charge on C5 does not change on the timescale of an oscillation of the DPR. There are ≈ 10 feet of coax with ≈ 30 pF/ft of capacitance between C5 and R2,C2, and this stray capacitance C_s must be considered in parallel with the capacitance C5. A lower limit on the discharge time of C5 is given by 2πR2(C5+C_s)$\approx$10 ms, since the resistance seen by capacitor C5 is at least as large as R2. Under the condition

$dQ/dt = 0$, where Q is the charge on C5, we can derive a relationship between the displacement of the DPR and the voltage into the SR560. We thus have

$$\frac{Q}{V} = \mathrm{C5} + C_s \tag{2.6}$$

where V is the voltage across C5 and the stray capacitance. Differentiating both sides of Eq. 2.6 and using the fact that the charge Q is constant, we have

$$\frac{\delta V}{V} = \frac{\delta \mathrm{C5}}{\mathrm{C5} + C_s} \approx \frac{\delta \mathrm{C5}}{\mathrm{C5}} \frac{\mathrm{C5}}{C_s} \tag{2.7}$$

since $\mathrm{C5} << C_s$. It will be shown in the FEM section that for the AS2 mode near 14 kHz C5 cannot be modeled as a parallel plate capacitor with a modulating spacing d: in fact the motion of the wing is about an axis nearly centered on and parallel to the surface of the fixed electrode. However, there are other modes for which it is possible to model C5 in this way, in which case we have

$$\frac{Q}{V} = \frac{\epsilon_0 A}{d} + C_s \tag{2.8}$$

where A is the area of the fixed electrode at C5 and d is the spacing between the electrodes forming C5. Differentiating both sides and using $dQ = 0$, we have

$$-\frac{Q}{V^2}\delta V = -\frac{\epsilon_0 A}{d^2}\delta d \tag{2.9}$$

$$= -\left(\frac{Q}{V} - C_s\right)\frac{\delta d}{d} \tag{2.10}$$

and

$$\frac{\delta V}{V} = \left(1 - C_s \frac{V}{Q}\right)\frac{\delta d}{d} \tag{2.11}$$

$$= \left(1 - \frac{C_s}{C_{tot}}\right)\frac{\delta d}{d} \tag{2.12}$$

$$\approx \frac{\mathrm{C5}}{C_{tot}}\frac{\delta d}{d_0}, \tag{2.13}$$

where $C_{tot} = \mathrm{C5} + C_s$ and d_0 is the equilibrium spacing. Rearranging terms, we have

$$\delta d = \frac{\delta V}{V}\frac{C_{tot}}{\mathrm{C5}} d_0. \tag{2.14}$$

Although Eq. 2.14 (or the analogous relation derived from the FEM calculation) is not necessary for determining the resonant frequency or dissipation at a given temperature, the amplitude of oscillation is useful for determining the power dissipated by the resonator or showing that the resonator is in the linear regime.

Some of the measurements at the lowest temperatures were done with the ringdown technique, and it was shown that this measurement technique led to the same values for the resonant frequency and dissipation as the sweep technique. In the ringdown technique, the circuit shown in Fig. 2.4 was again used. The function generator was set to the resonant frequency of the desired mode in order to energize the resonator. After reaching a sufficient amplitude of oscillation, the drive was disconnected. At this point, the frequency setting of the function generator was changed so that the lockin reference was slightly off the mechanical resonance. Thus any spurious signals at the beat frequency would oscillate quickly compared to the ringdown time of the mechanical resonator and would not affect the measured time constant of the decay.

2.5 FEM Analysis

In order to explore non-linearity and strain heating, finite element method (FEM) calculations of the modes of the DPR were done in collaboration with Alan Zehnder. Previous FEM calculations for a single crystal silicon paddle resonator are documented in [42]. A traveling microscope was used to determine the coordinates of all the corners of the DPR. For Suprasil 300, the Young's Modulus is 70 GPa, the Poisson Ratio is 0.17 and the density is 2.203 g/cm^3 [43]. Inputting this information into the ABAQUS FEM program yielded a list of res-

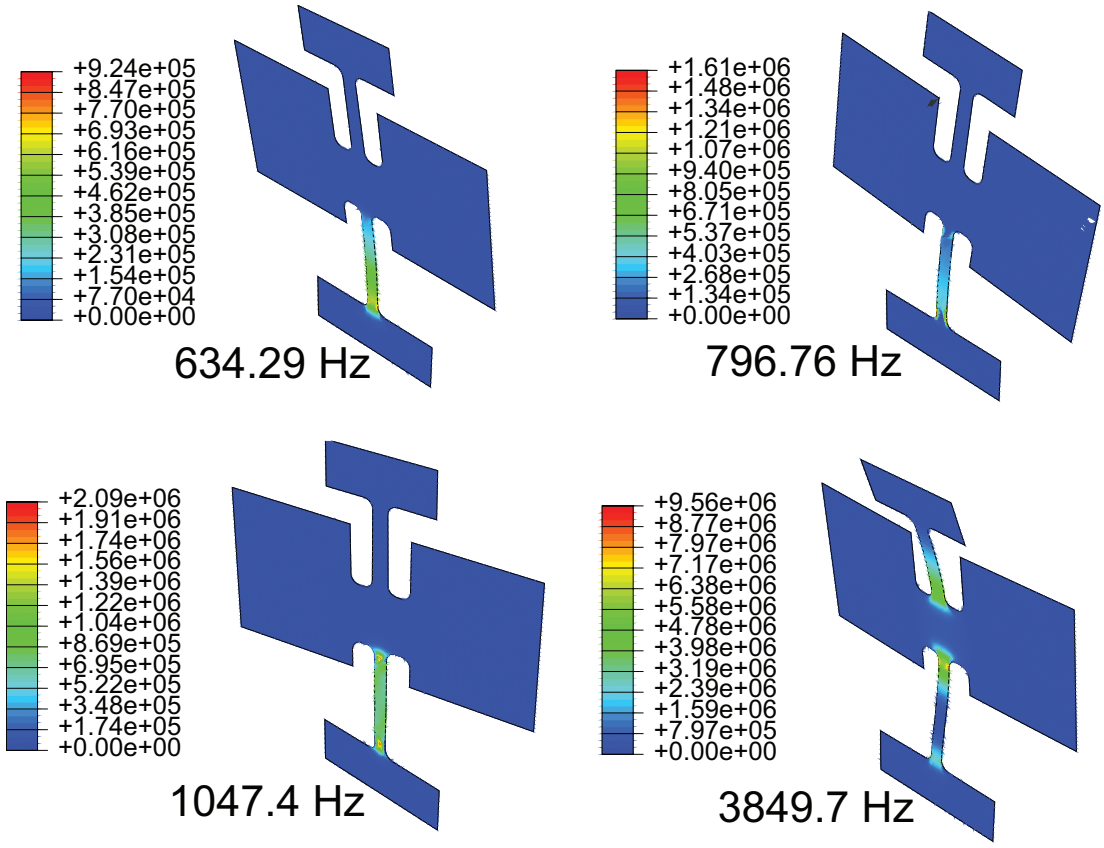

Figure 2.5: Displacement profiles and strain energy densities (J/m^3) for the first through fourth modes of the SiO_2 double paddle resonator at 1 mm peak displacement. The lowest edge of the resonator coincides with the upper edge of the clamp.

onant frequencies for the DPR that matched the five experimentally identified frequencies to within 2%. The lowest edge of the resonator was held stationary in the FEM calculation. Plots of the displacement profile and strain energy for the lowest 15 modes are shown in Figs. 2.5, 2.6, 2.7, and 2.8.

The FEM model should also provide insight into the clamping loss for the different modes of the resonator. This type of dissipation is due to elastic vibrations of the resonator's support structure [44]. According to [45], a high mechanical energy density near the support structure leads to a large clamping

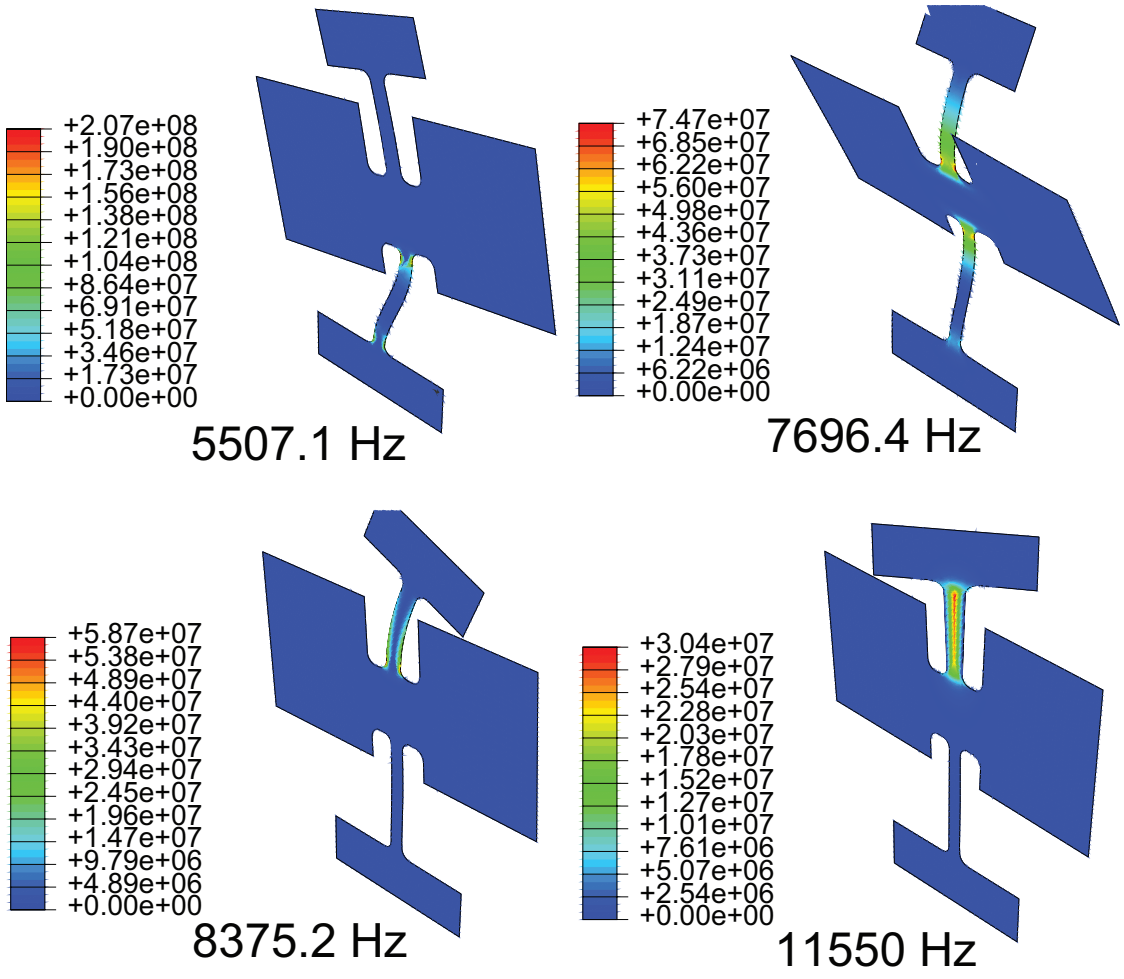

Figure 2.6: Displacement profiles and strain energy densities (J/m^3) for the fifth through eighth modes of the SiO_2 double paddle resonator at 1 mm peak displacement. The lowest edge of the resonator coincides with the upper edge of the clamp.

loss. Modes in which the force due to the support and the moments about the support vanish have low clamping loss. Intuitively, the AS2 (14.0 kHz) mode should have a lower clamping loss than a symmetric torsional mode because in the former the strain energy is concentrated farther from the support. It is also claimed in [40] that the anti-symmetric torsional mode of a resonator with a geometry similar to ours has a lower clamping loss than the symmetric torsional

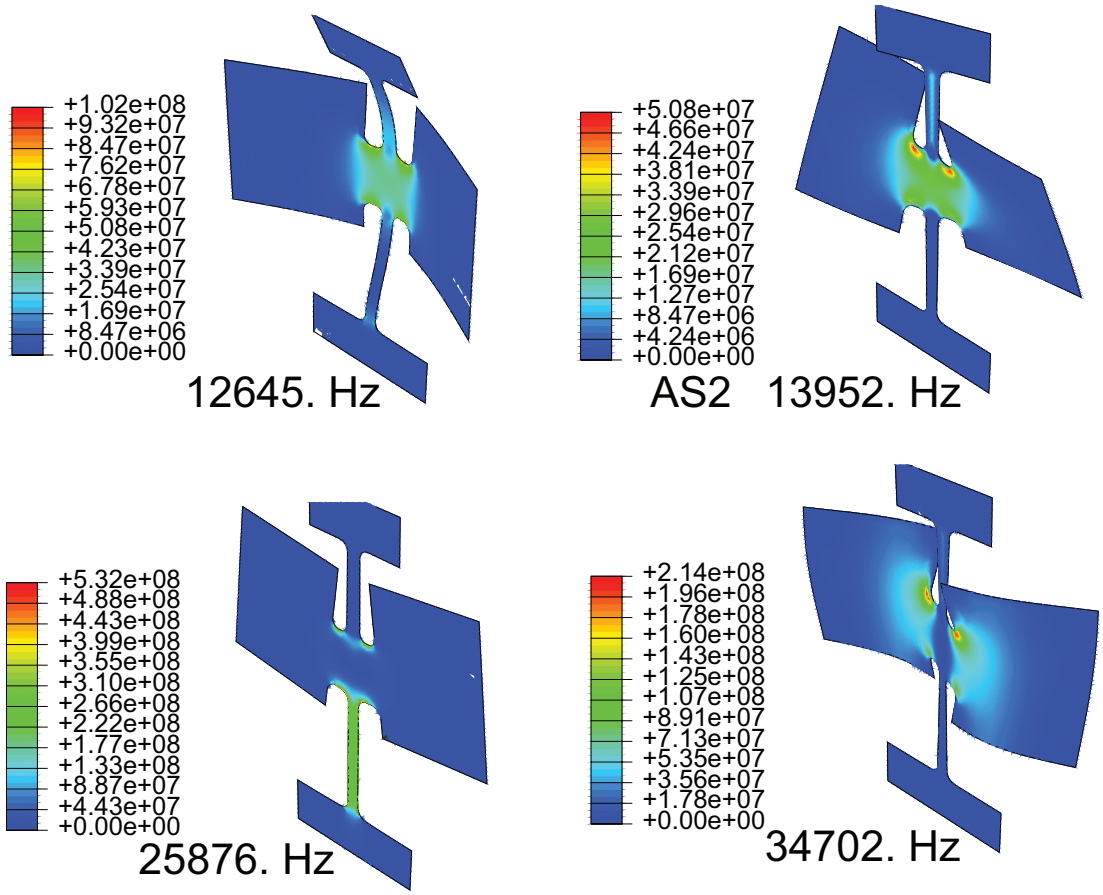

Figure 2.7: Displacement profiles and strain energy densities (J/m^3) for the ninth through twelfth modes of the SiO_2 double paddle resonator at 1 mm peak displacement. The lowest edge of the resonator coincides with the upper edge of the clamp.

more. However, the strain energy density along the clamping line in our FEM calculation was found to be almost the same for three modes that were studied: a bending mode, a symmetric torsion mode, and the AS2 mode (Fig. 2.9). This result is surprising, and no experimental input is available because, as shown in section 3.1, none of the modes that were used seem to be affected by clamping loss. Furthermore, no difference in the loss was observed for the symmetric and anti-symmetric modes described in the section of [45] called "Support-Related

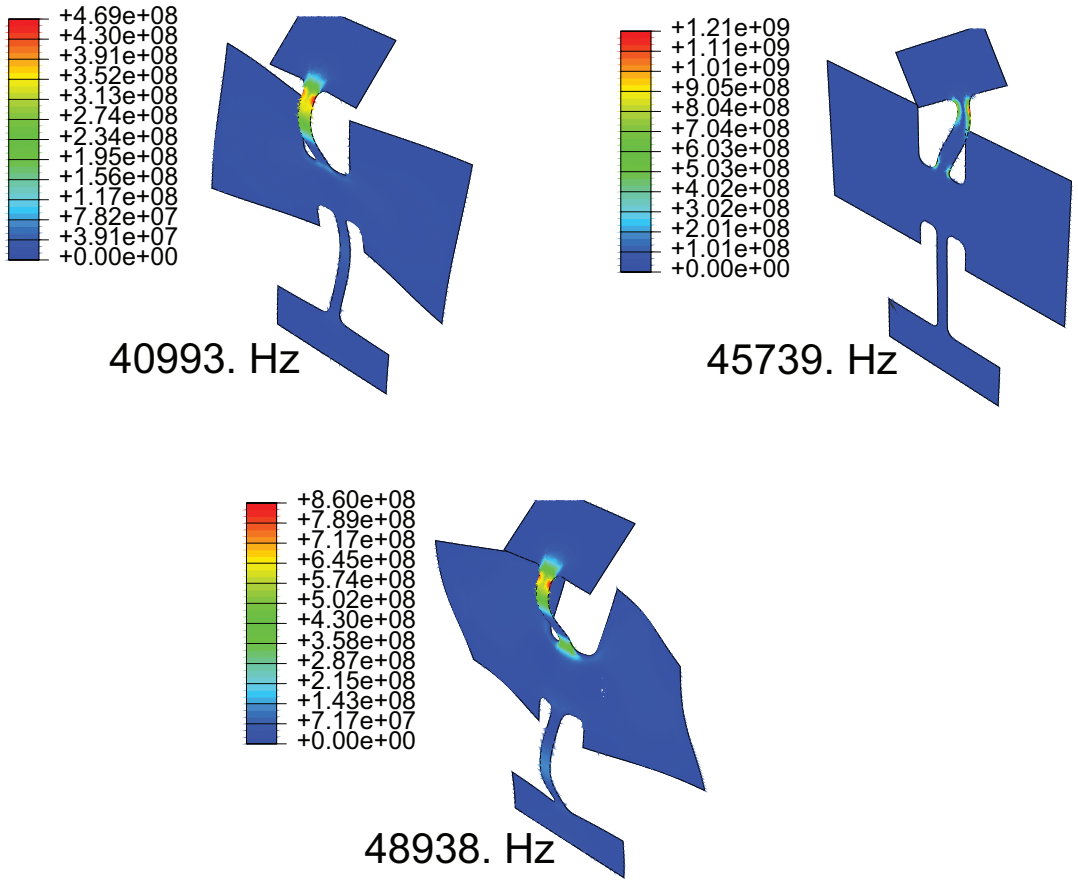

Figure 2.8: Displacement profiles and strain energy densities (J/m^3) for the 13th through 15th modes of the SiO_2 double paddle resonator at 1 mm peak displacement. The lowest edge of the resonator coincides with the upper edge of the clamp.

Losses". One way to settle this issue would be to accurately model a double paddle resonator made of single crystal silicon (so that bulk loss mechanisms are negligible) and compare the low temperature loss in each mode with the corresponding strain energy near the clamp or the reaction forces and moments exerted by the clamp. Because the edges of the silicon double paddle resonators are beveled due to the etching process, accurate modeling of these resonators is more involved than modeling of the glass resonators.

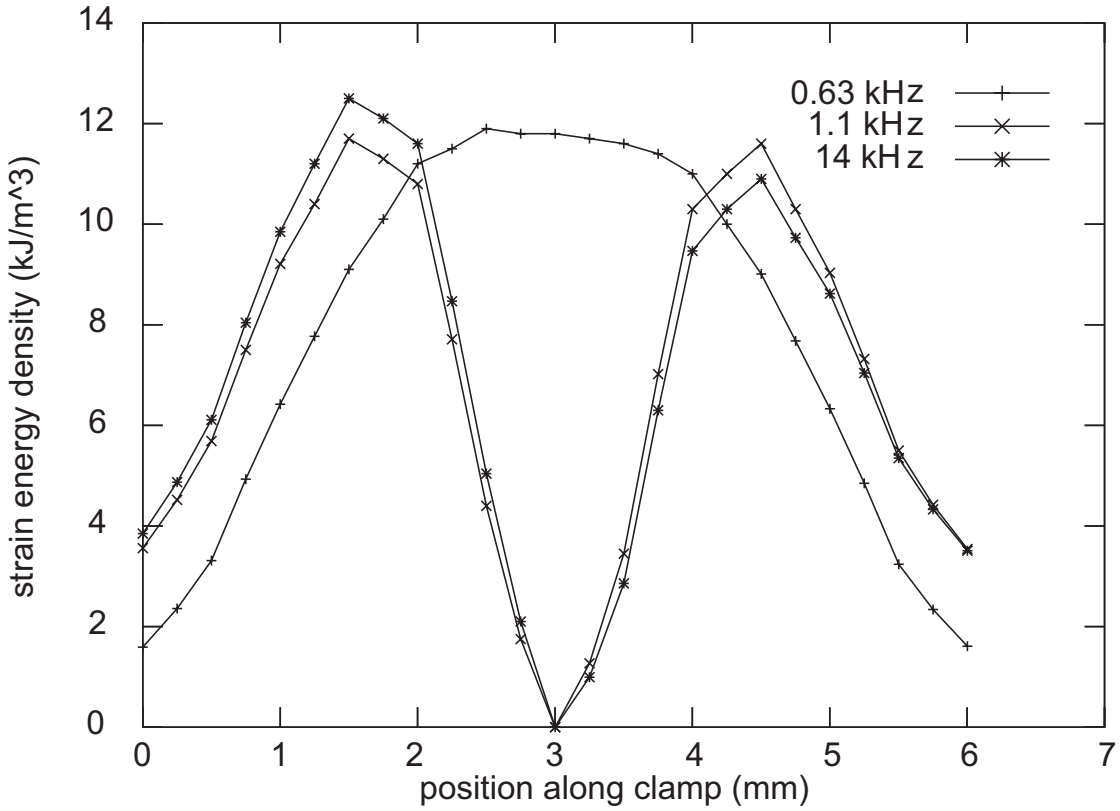

Figure 2.9: Strain energy density calculated at the finite element nodes along the resonator clamping line for modes at three different calculated frequencies. The clamp position and the mode shapes are shown in Figs. 2.5, 2.6, 2.7, and 2.8.

The mode at 14.0 kHz, called the second antisymmetric torsion (AS2) mode (Fig. 2.7), yielded the best acoustic data. Thus, I focussed on this mode and used the FEM calculation to obtain a voltage-strain calibration. As noted above, because of the shape of the AS2 mode, the capacitor formed by the paddle wing and the fixed electrode cannot be modeled simply as a parallel plate capacitor with variable spacing. In fact, as shown in Fig. 2.7, the motion of a wing is almost rigid about an axis near its center. We can thus make a first order approximation to the relative change in capacitance before extracting the exact calibration from the FEM calculation. The cross section of the wing in this ap-

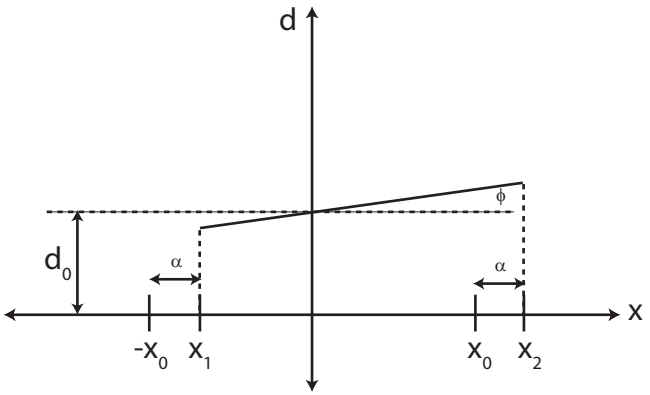

Figure 2.10: Cross section of the tilted wing.

proximation is sketched in Fig. 2.10. The parameter α represents the offset of the wing with respect to the fixed electrode that gives rise to the first order contribution to the displacement signal; for $\alpha = 0$, the rotation axis of the wing is centered over the fixed electrode. The plane of the fixed electrode is at $d = 0$. Thus the spacing along the wing is given as

$$d = \phi x + d_0. \tag{2.15}$$

The capacitance is then given by

$$C = \int \frac{\epsilon_0 dA}{d} \tag{2.16}$$

$$= \epsilon_0 w \int_{x_1}^{x_2} \frac{dx}{\phi x + d_0}, \tag{2.17}$$

where w is the width of the wing in the direction perpendicular to the plane of the cross section in Fig. 2.10, ϵ_0 is the permittivity of free space, and the other parameters are defined in Fig. 2.10. Evaluating the integral, we have

$$C = \frac{\epsilon_0 w}{\phi} \left[\ln d_0 + \ln \left(\frac{\phi x}{d_0} + 1 \right) \right]_{x_1}^{x_2} \tag{2.18}$$

$$\approx \frac{\epsilon_0 w}{\phi} \left[\ln d_0 + \frac{\phi x}{d_0} - \frac{1}{2} \left(\frac{\phi x}{d_0} \right)^2 \right]_{x_1}^{x_2} \tag{2.19}$$

$$= \frac{\epsilon_0 w}{\phi} \left[\frac{\phi}{d_0}(x_2 - x_1) + \frac{\phi^2}{2d_0^2}(x_1^2 - x_2^2) \right], \tag{2.20}$$

where the approximate equality holds because $\phi x << d_0$. The first term in brackets in Eq. 2.20 corresponds to the equilibrium capacitance $\approx C$ and the second term corresponds to the first order correction δC. We now let $x_1 = -x_0 + \alpha$ and $x_2 = x_0 + \alpha$ so that $x_1^2 - x_2^2 = -4x_0\alpha$. We then have

$$\frac{\delta C}{C} = \frac{\phi\alpha}{d_0} \tag{2.21}$$

to first order in α, assuming the deflection sketched in Fig. 2.10. As will be shown below, the curve running through the wing for which the displacement vanishes is quite close to the center of the electrode, i.e., $\alpha \approx 0$. Thus the first order approximation to $\delta C/C$ may not be sufficiently accurate and we must use the FEM results.

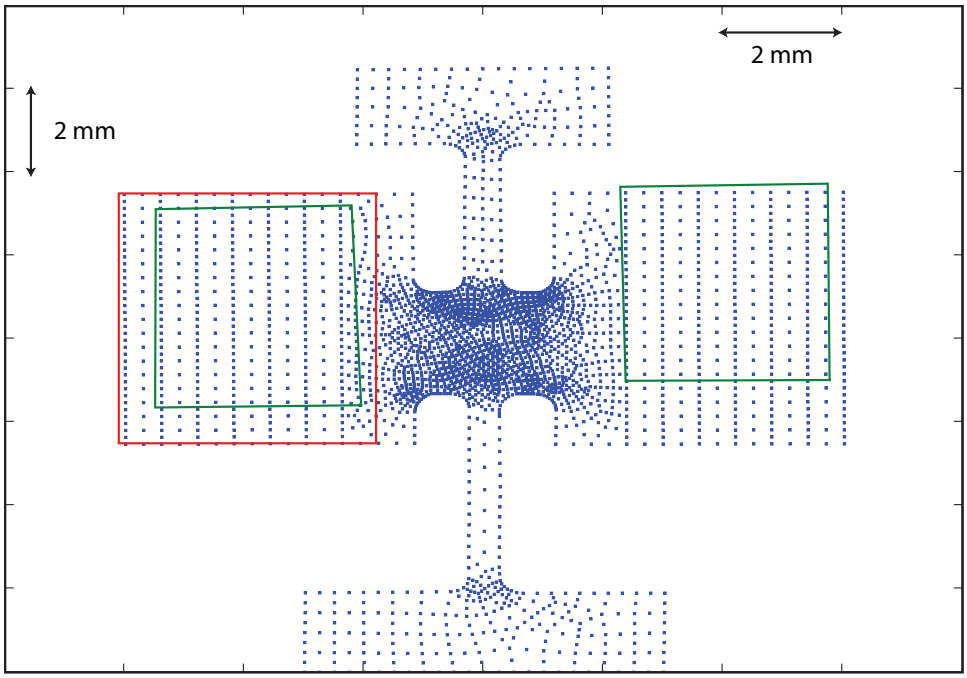

Figure 2.11: Nodes for the FEM calculation (blue) and effective borders of the fixed electrodes (green). Also shown is the domain for the contour plot in Fig. 2.12 (red).

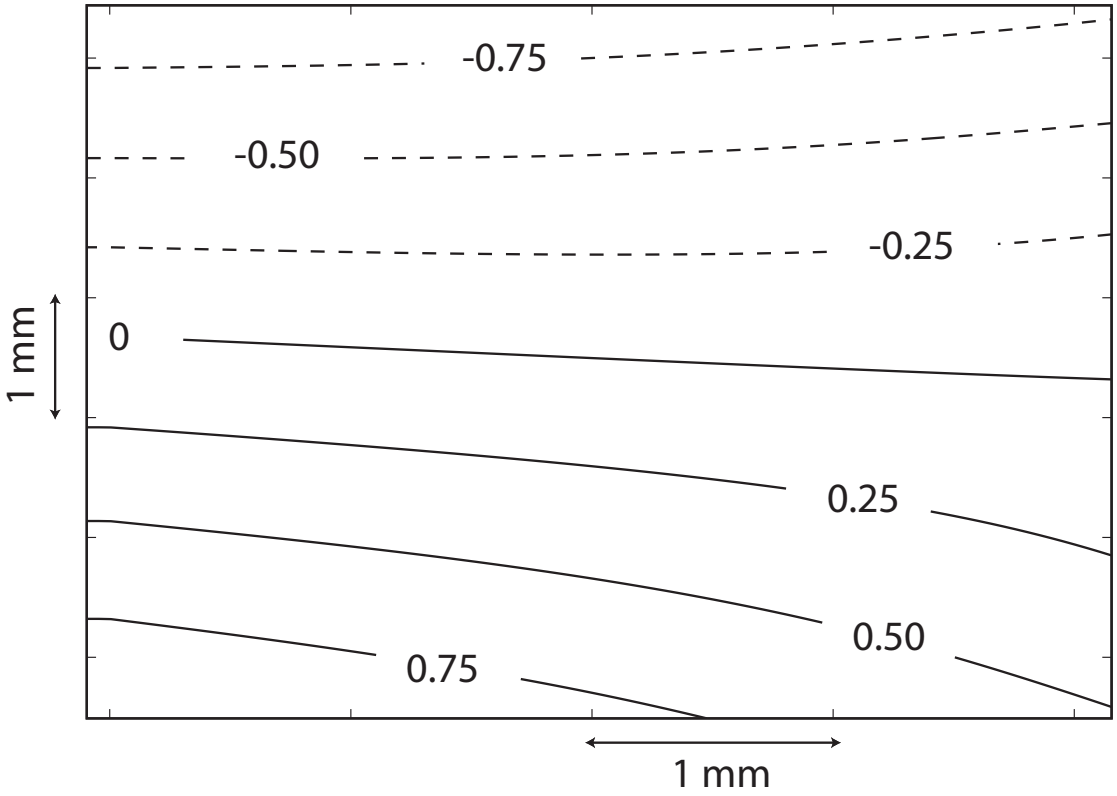

Figure 2.12: Contour plot of the normalized DPR displacement in the region bounded by red lines in Fig. 2.11.

Fig. 2.11 shows the nodes used for the FEM calculation as well as the effective area of the fixed electrodes. In this approximation, only the regions of the electrodes that are opposite a region of silver film on the DPR contribute. Thus the left side of the rectangle corresponding to the left electrode was cropped slightly due to the incomplete coverage of the silver film. Because the left electrode is then not perfectly rectangular, the integration region was broken up into a central rectangle and bordering triangles. The Python code for the analysis of the FEM results is in the Appendix. Fig. 2.12 shows a contour plot of the displacement for the left DPR wing in the region bordered by the red lines in Fig. 2.11. It can be seen that the zero displacement contour is nearly straight, but it is also very close to the center line of the left electrode, so the curvature of the contour may be important. Using $C = \int \frac{\epsilon_0 dA}{d}$ with the values for d output by the FEM calculation yields

$$\frac{\delta C}{C} = 1.5 \times 10^{-8} \tag{2.22}$$

for a peak displacement of the wing of 0.01 nm, corresponding to an angular excursion $\phi = 3.4 \times 10^{-9}$ rad. The relative change in capacitance is related to the voltage measured in the experiment by Eq. 2.7. Along with the Lorentzian line shape, the FEM results allowed us to show that we were operating the DPR in the linear regime, as discussed in the experimental results section of this dissertation. Using these values and the equilibrium spacing of $d_0 = 0.058$ mm in Eq. 2.21 yields an effective offset α=0.2 mm, which is quite small. A higher sensitivity could have been obtained for the AS2 mode by increasing the offset α between the fixed electrode and wing centers, but this would have decreased the sensitivity for modes in which rotations are about the axis defined by the neck and leg of the DPR.

CHAPTER 3

EXPERIMENTAL RESULTS

3.1 $\delta v/v_0$ and Q^{-1} of Amorphous SiO_2

A sample of the raw data at 14.0 kHz for two different drive levels at each of three temperatures is shown in Fig. 3.1 [46]. The lockin time constant ranged between one and ten seconds, and no additional averaging was used for the data in Fig. 3.1. The frequency sweeps were done slowly enough so that there was no significant change in the response if the sweep rate was halved. The center frequency for data taken at low drive for each temperature was shifted to zero frequency, but any frequency offset between the high and low drive data at a given temperature was retained. It was important to lower the drive level as the temperature decreased in order to remain in the linear regime, where the data exhibit the Lorentzian form shown by the black lines in the figure. The frequency shift between low and high drive data sets at each temperature is negligible on the scale of the variation of $\delta v/v_0$ with temperature and is accounted for by the small thermal drift of the low temperature stage.

Corroborating evidence that the data were taken in the linear regime is provided by the results of the FEM calculation. These imply that the theoretical condition of linearity [47], $e\gamma/k_BT << 1$, where e is the strain in the paddle, is satisfied for the measurements in Fig. 3.1. In the case of the double paddle resonator, there is a complicated distribution of strains, and the theory does not specify what type of average should be used to obtain the relevant strain value. Thus the tilt angle of the wing ϕ indicated in Fig. 3.1 is used for the strain. Equation 2.7 relates the change in capacitance per wing angular displacement ϕ to a

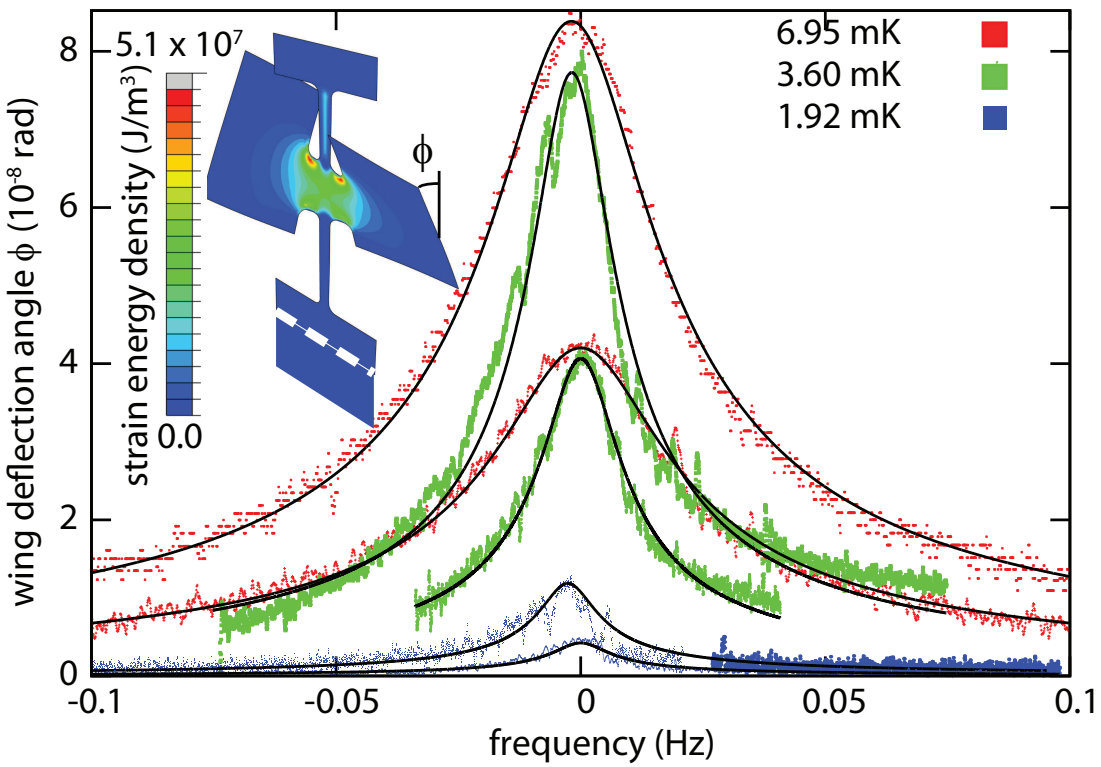

Figure 3.1: Response of the 14.0 kHz mode at three different temperatures. For each temperature two drive levels were chosen to demonstrate the linear response. Inset: Finite element visualization of the oscillator displacement and strain energy density (linear scale) at 14.0 kHz for 0.4 radians peak displacement. The white broken line indicates the upper edge of the dry clamp.

change in voltage. As shown in Fig. 3.1, the peak wing displacement at 1.92 mK is about 10^{-8} radians. Using a typical deformation potential γ=1 eV leads to $e\gamma/k_BT \approx 0.1$ which fulfills the theoretical condition for linearity. Care was taken to prevent experimental artifacts at other T and ω as well.

We used the low strain measurements in Fig. 3.1 and those at other T and ω to obtain $\delta v/v_0 \approx (f_\mathrm{r} - f_{\mathrm{r},0})/f_{\mathrm{r},0}$ (assuming negligible thermal expansion) and $Q^{-1} = \Delta f/f_\mathrm{r}$, where f_r is the frequency at peak response and Δf is the half-power width. Ideally $f_{\mathrm{r},0} = f_\mathrm{r}(T = 0)$, and any small difference amounts to an

offset in $\delta v/v_0$, which is not of interest here. These results are shown along with the predictions of the STM in Figs. 3.2 and 3.3. The solid curves in Fig. 3.2 and the red and blue curves in Fig. 3.3 correspond to the STM with best fit values of the tunneling strength $C = 2.4 \times 10^{-4}$ and prefactor of the single-phonon relaxation rate $a = 9.0 \times 10^7$ $\mathrm{K}^{-3}\mathrm{s}^{-1}$, and the dashed and dotted curves in Fig. 3.2 show the sensitivity of the fit to the parameter a. The best fit values obtained here are comparable to those in [4].

The discrepancy between the measurements of Q^{-1} and the predictions of the STM below 10 mK shows most clearly that the present results are not in agreement with the STM. This result cannot be explained by thermal decoupling between the thermometer and the sample because $\delta v/v_0$ exhibits the expected $\log\ T$ dependence down to 2.5 mK. The departure of the data from the standard tunneling model also cannot be explained by a temperature independent clamping loss.

As observed in previous experiments that did not extend to such low temperatures [4, 19, 48, 49], the ratio of $d(\delta v/v_0)/d(\log_{10} T)$ at low and high temperatures is more nearly 1:-1 than the 2:-1 ratio predicted by the STM. In fact, the $\delta v/v_0$ data in the present work and in [4] are in good agreement over much of the temperature range as shown in Fig. 3.4. Also, the tunneling strength determined from the slope of $\delta v/v_0$ for $T << T_{CO}$ does not exactly agree with the tunneling strength determined from the value Q^{-1} in the plateau for $T >> T_{CO}$, where T_{CO} is defined in Eq. 1.70. These observations are summarized in Table 3.1. If the standard tunneling model were in perfect agreement with the data, the values in each column would agree with each other. No explanation for the discrepancies has been forthcoming. For strong TLS interaction-driven

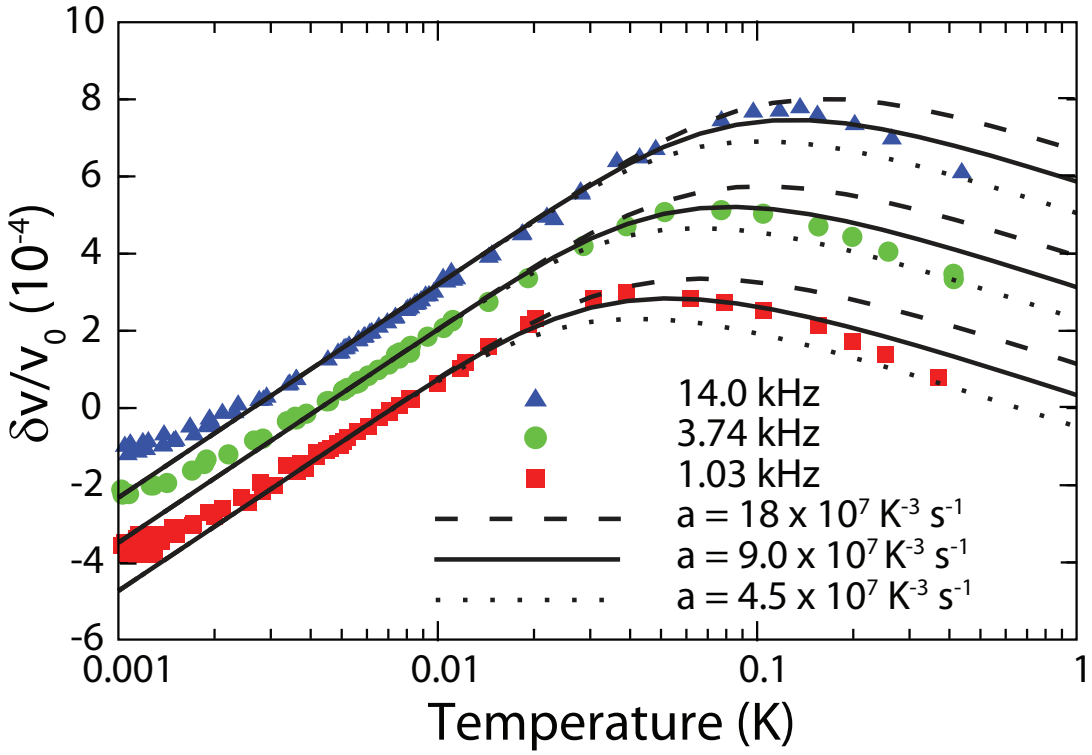

Figure 3.2: Measurements of the relative change in sound velocity $\delta v/v_0$ (data points) and predictions of the STM [$b = 0$] (curves) for each of the experimental frequencies (offset vertically). The curves correspond to a tunneling strength $C = 2.4 \times 10^{-4}$ and the indicated values of a, the prefactor of the single-phonon relaxation rate. The best fit at each frequency is represented by a solid curve. These curves are indistinguishable from those corresponding to the same C and a, but with the prefactor $b = 1.0 \times 10^5$ K^{-1}s^{-1} (see text).

relaxation, the slope ratios approach 1:-1, but such strong interactions are inconsistent with the Q^{-1} data. As will be discussed below, a modification of the TLS distribution leads to a consistent fit to Q^{-1} and $\delta v/v_0$.

Figure 3.3 shows the internal friction data from the present experiment along with predictions of the tunneling model including the relaxation rate bT from Eq. 1.114. The best fit values of C and a were retained and the new interac-

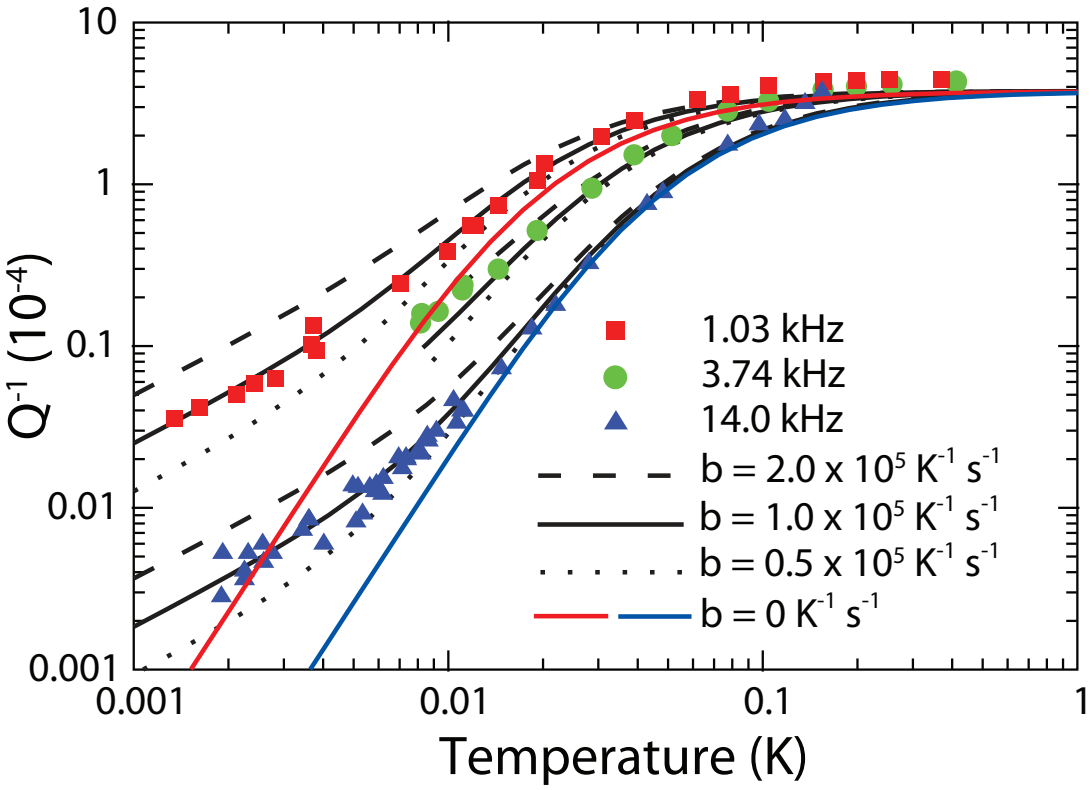

Figure 3.3: Measured internal friction Q^{-1} (data points) and predictions (curves) for each of the experimental frequencies. The curves correspond to a tunneling strength $C = 2.4 \times 10^{-4}$, a single phonon relaxation prefactor $a = 9.0 \times 10^7$ K^{-3}s^{-1}, and various values of b. The solid black curves correspond to the best fit value of b and agree well with the measured Q^{-1}. For comparison, the prediction of the non-interacting model ($b = 0$) is shown for $\omega/2\pi = 1.03$ and 14.0 kHz.

tion parameter b was varied. The best fit (solid black lines) corresponds to a *single* value of $b = 1.0 \times 10^5$ K^{-1}s^{-1}. Curves corresponding to a factor of two variation in b are also drawn to show the sensitivity to the choice of b. For comparison with the STM prediction, curves corresponding to $b = 0$ and $\omega/2\pi = 1.03$ and 14.0 kHz are also shown. The result with $b > 0$ for the sound velocity is not shown because for $a = 9.0 \times 10^7$ K^{-3}s^{-1} and $b = 1.0 \times 10^5$ K^{-1}s^{-1} it is

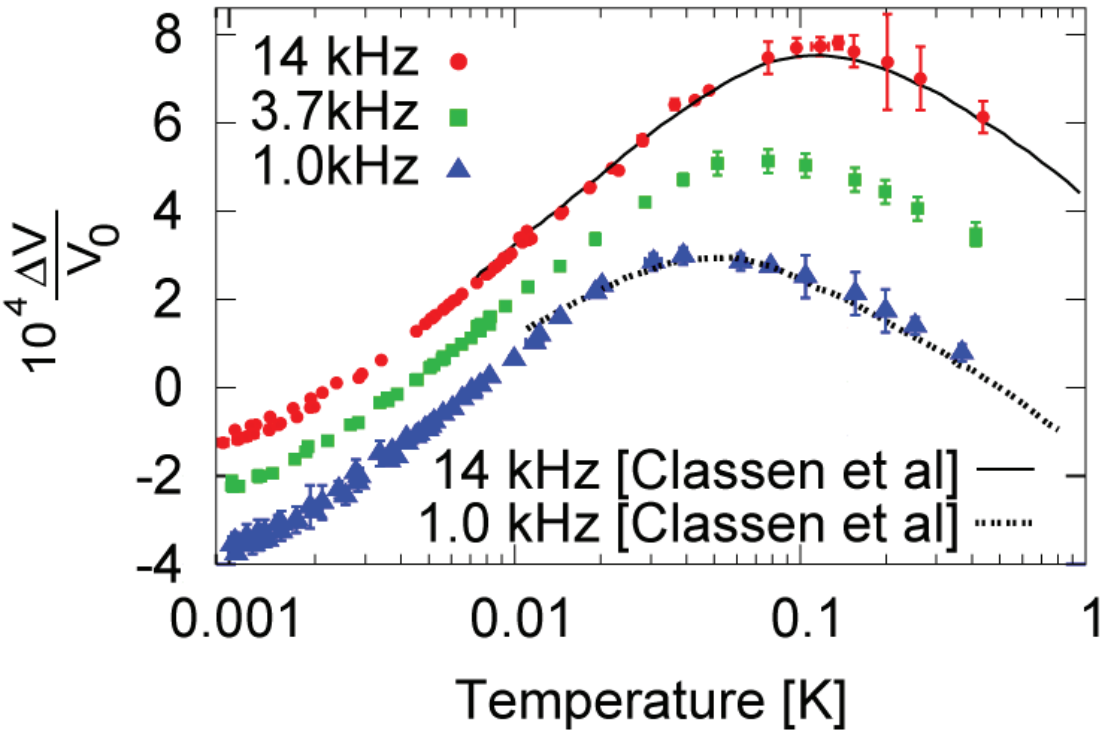

Figure 3.4: Comparison of $\delta v/v_0$ from the present work with that of [4].

Table 3.1: Measured values of quantities in the left most column and corresponding expected values for quantities in the top column determined using the asymptotic forms of the standard tunneling model given in Table 1.1.

	$Q^{-1}_{plateau}$	$\frac{d\frac{\delta v}{v_0}}{d\log_{10}T}, T \ll T_{CO}$	$\frac{d\frac{\delta v}{v_0}}{d\log_{10}T}, T \gg T_{CO}$	C
$Q^{-1}_{plateau}$	4.5	6.6	-3.3	2.9
$\frac{d\frac{\delta v}{v_0}}{d\log_{10}T}, T \ll T_{CO}$	3.8	5.5	-2.8	2.4
$\frac{d\frac{\delta v}{v_0}}{d\log_{10}T}, T \gg T_{CO}$	6.3	9.2	-4.6	4.0

indistinguishable from the STM prediction (Fig. 3.2). Thus the most striking discrepancy between the STM and the present data, i.e., the behavior of Q^{-1} for $T < 10\ \mathrm{mK}$, is resolved by assuming the relaxation rate bT. Furthermore, the quality of the fit to Q^{-1} for $T > 10\ \mathrm{mK}$ and to $\delta v/v_0$ over the entire temperature range is maintained or slightly improved.

The origin of the additional relaxation rate assumed above may be interactions between pairs of TLS. It is argued in [50] that the existence of such four-particle clusters leads to a relaxation rate that is linear in temperature (Eq. 1.114). As noted in [35], the prefactor of the term that is linear in temperature must be determined by experiment at this point. While [25] also predicts a relaxation rate that is linear in temperature, according to [35] and [34] the number of resonant triples of TLS was overestimated.

There are significant differences between the present work and [4], which did not extend to as low a temperature. In [4], the temperature dependence of Q^{-1} was characterized by the power laws T^{α}, which did not have a direct connection to theory, and a monotonic frequency dependence of α was noted. While our data could in principle be so fitted with different values of α over the same limited ($30\ \mathrm{mK} > T > 6\ \mathrm{mK}$) temperature range, it became evident after pushing to lower T that the exponents α relate to the crossover from the developing T^3 STM behavior to the linear temperature dependence that is likely generated by interaction-driven relaxation (see Fig. 3.3). Thus we have shown that it is not necessary to assume a range of power laws to fit the data. We also note that all Q^{-1} in [4] are greater than those observed in our experiment (and differ significantly from those reported in [3]). Third, the frequency dependence of the slope $d(\delta v/v_0)/d(\log_{10} T)$ observed in [4] was not observed in

the present work. Thus, the extension of the $\delta v/v_0$ measurements to a lower temperature in the present work allowed for a more definitive measurement of $d(\delta v/v_0)/d(\log_{10} T)$ at 1.0 kHz than in [4].

By assuming a modified TLS distribution function [5]

$$P_\mu(r, E) = P_0(1-r)^{\mu-1/2}/2r, \tag{3.1}$$

where $r = (\Delta_0/E)^2$, we were able to fit the $\approx 1 : -1$ slope ratio exhibited by our $\delta v/v_0$ data. For $\mu = 0$, this distribution reduces to that in Eq. 1.4, which was used for the fits in Figs. 3.3 and 3.2. Our $\delta v/v_0$ and Q^{-1} data at 1.03 kHz are shown in Fig. 3.5 along with the calculations assuming $\mu = 0.09, C = 2.9 \times 10^{-4}, a = 6.0 \times 10^7$ $\mathrm{K^{-3}s^{-1}}$, and $b = 1.0 \times 10^5$ $\mathrm{K^{-1}s^{-1}}$. Similar agreement between theory and data was obtained at 3.74 and 14.0 kHz using the same fitting parameters. The density of tunneling states is plotted versus $r = (\Delta_0/E)^2$ in Fig. 3.6. It can be seen that increasing μ does not affect the number of tunneling states at small r, but decreases the density of tunneling states at high r. The density of states as a function of energy, obtained by integrating Eq. 3.1 over r, depends on the choice of $r_m = (\Delta_{0,min}/E)^2$. For the calculation of $\delta v/v_0$ and Q^{-1} in Fig. 3.5, $r_m = 0$ was assumed, although it is not possible to plot the corresponding density of states because it is logarithmically divergent at each energy. As r_m approaches zero, the density of states as a function of energy becomes increasingly uniform, and the distributions corresponding to different values of μ become indistinguishable. Therefore, although increasing μ has an effect on the acoustic predictions, the effects of μ are not manifested in the density of states versus energy.

Additional insight into the modified TLS distribution function can be obtain by transforming the coordinates to the asymmetry Δ and the tunneling para-

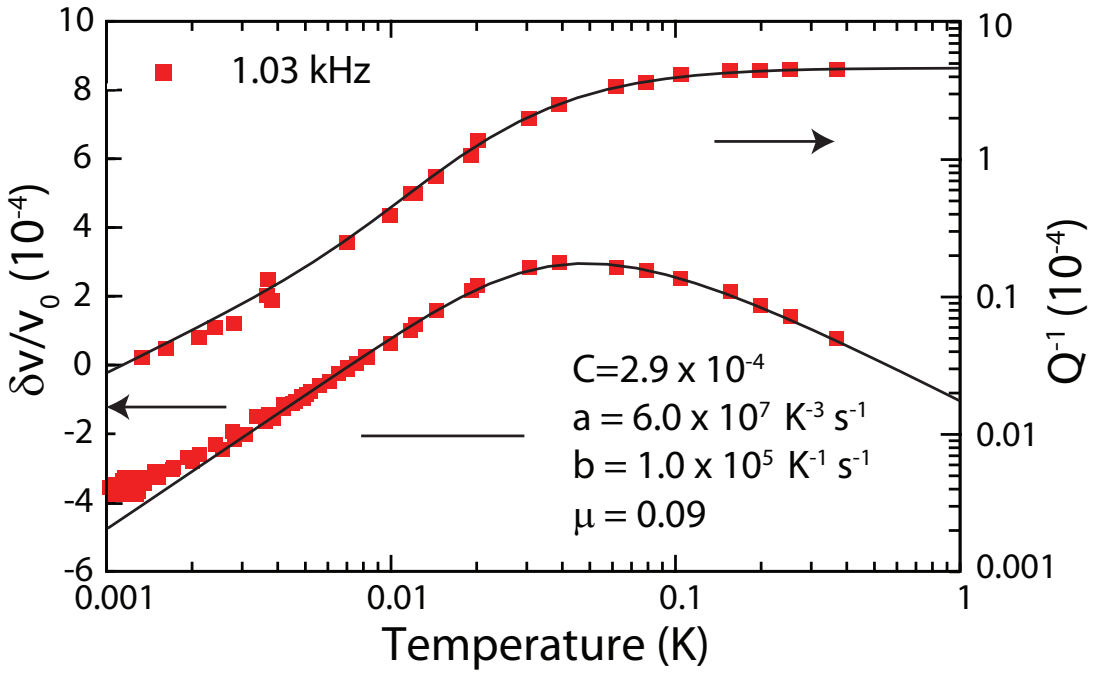

Figure 3.5: Measured $\delta v/v_0$ (offset vertically) and Q^{-1} at 1.03 kHz along with tunneling model predictions assuming an interaction-driven relaxation rate $b = 1.0 \times 10^5$ K^{-1}s^{-1} and TLS distribution parameter $\mu = 0.09$.

meter λ (Eq. 1.3):

$$P_\mu(\Delta,\lambda)d\Delta d\lambda = P_\mu(r,E)\left|\frac{\partial r}{\partial\Delta}\frac{\partial E}{\partial\lambda} - \frac{\partial r}{\partial\lambda}\frac{\partial E}{\partial\Delta}\right| d\Delta d\lambda \tag{3.2}$$

where I have followed the physicist's convention of labeling the distribution function by its arguments. Using

$$\frac{\partial r}{\partial\Delta} = -\frac{2\Delta\Delta_0^2}{E^4} \tag{3.3}$$

$$\frac{\partial r}{\partial\Delta_0} = \frac{2\Delta^2\Delta_0}{E^4} \tag{3.4}$$

$$\frac{\partial E}{\partial\Delta_0} = \frac{\Delta_0}{E} \tag{3.5}$$

$$\frac{\partial E}{\partial\Delta} = \frac{\Delta}{E} \tag{3.6}$$

$$\frac{\partial\Delta_0}{\partial\lambda} = -\Delta_0 \tag{3.7}$$

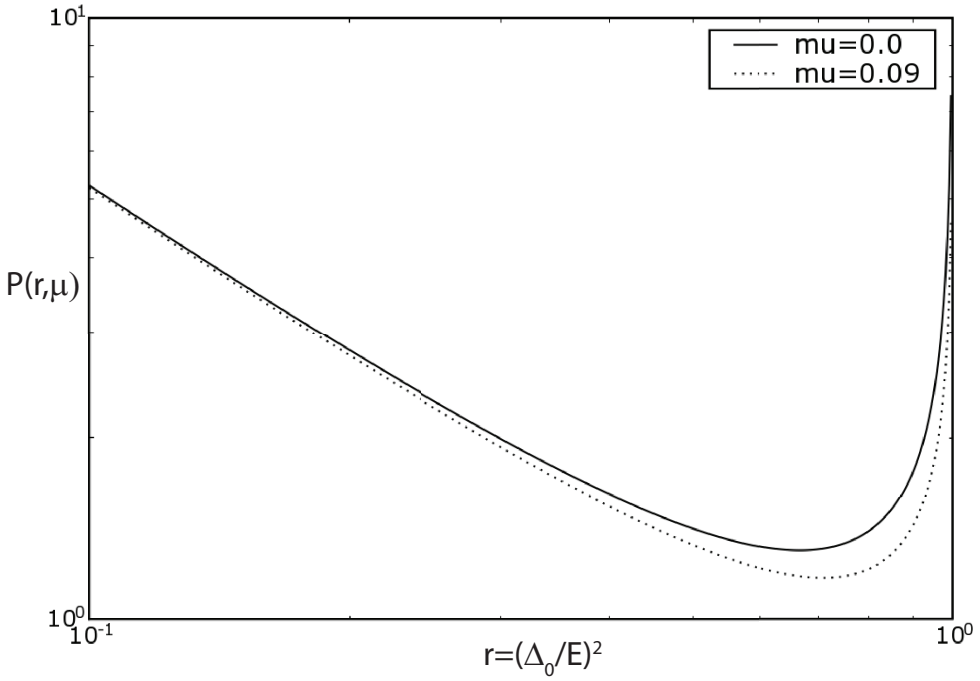

Figure 3.6: The TLS distribution in [5] plotted versus $r = (\Delta_0/E)^2$ for $\mu = 0$ (as in Eq. 1.4) and for $\mu = 0.09$ (best fit value).

yields

$$P_\mu(\Delta, \lambda) d\Delta d\lambda = P_0 \left(\frac{\Delta}{E}\right)^{2\mu} d\Delta d\lambda. \tag{3.8}$$

This form of the distribution again indicates that increasing μ suppresses the density of tunneling states with small asymmetry.

The fit of the STM to thermal properties of glass is not significantly degraded by assuming $\mu = 0.09$: the heat capacity remains nearly linear in T and the thermal conductivity remains nearly quadratic in temperature [5]. The heat capacity of the ensemble of two level systems is given by integrating the heat capacity of

a single two level system over the distribution of two level systems

$$C = \int_{E_{min}}^{\infty} \int_{r_m}^{1} P_\mu(r, E) dr C_{TLS} dE \tag{3.9}$$

where $P_\mu(r, E)$ is given by Eq. 3.1. C_{TLS} is the heat capacity of a single two level system, which is obtained by differentiating with respect to temperature the mean energy of a two level system at temperature T:

$$C_{TLS} = \frac{E^2}{4k_B T^2} \mathrm{sech}^2 \left(\frac{\beta E}{2} \right). \tag{3.10}$$

One must choose a non-zero r_m in order to compute a finite heat capacity since the density of states with respect to energy diverges for $r_m = 0$. At a given temperature, only two level systems with energy splittings satisfying $0.1T < E < 10T$ significantly contribute to the heat capacity, which means that if the temperature range of interest is $T_{min} < T < T_{max}$, the heat capacity is approximately given by

$$C = \int_{T_{min}/10}^{T_{max} \times 10} \int_{r_m}^{1} P(r, \mu) dr C_{TLS} dE, \tag{3.11}$$

where the condition $T_{min}/10 > E_{min}$ must hold. Since I assumed $E_{min} = 0$ in the calculation of $\delta v / v_0$ and Q^{-1} in Fig. 3.5, I will choose E_{min} to be small but non-zero for the heat capacity calculation, although it must also satisfy $E_{min} > 0$. As E_{min} is decreased, the heat capacity increases and approaches a more perfectly linear temperature dependence. In the temperature range of interest (1 mK to 1 K) and for $\Delta_{0,min} = 1$ nK, the heat capacity with $\mu = 0$ is indistinguishable from the heat capacity with $\mu = 0.09$ and has a nearly linear temperature dependence. The results of a numerical calculation of the heat capacity for the two different values of μ are shown in Fig. 3.7 for $\Delta_{0,min} = 1$ nK. The sampling of the density of states with respect to energy is logarithmically uniform so that even for small T the density of states is sampled many times over the relevant range,

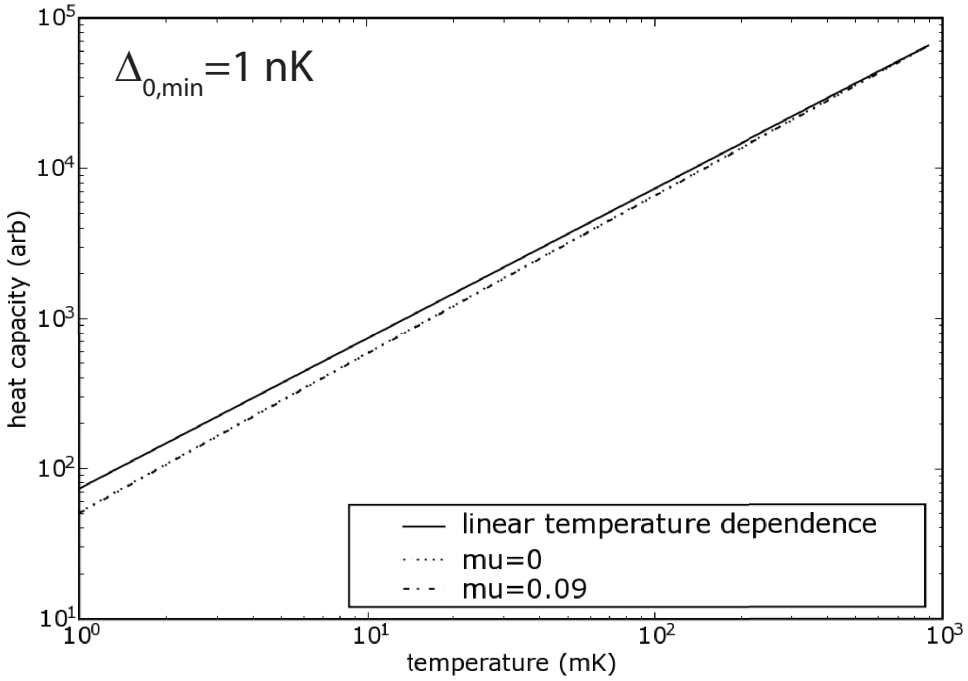

Figure 3.7: Two level system heat capacity as a function of temperature for $\Delta_{0,min} = 1$ nK and $\mu = 0$ (as in Eq. 1.4) and for $\mu = 0.09$ (best fit value). For such a small $\Delta_{0,min}$, the heat capacities are nearly the same for both values of μ.

i.e., the number of sample points in the interval $0.1 < T < 10T$ is the same for all T. While we have no physical justification for this particular distribution, we have shown that it is possible to account for the behavior of Q^{-1} and $\delta v/v_0$ independently from TLS interactions for $T > T_{CO}$, where T_{CO} is defined in Eq. 1.70.

3.2 Leveling Off of $\delta v/v_0$

When conducting low temperature experiments on dielectric glasses, it is important to be careful of temperature gradients between the sample and the thermometer due to heat input from a variety of sources. The saturation of the sound speed in Ref. [51] was initially attributed to intrinsic physics, namely a low energy cut off in the tunneling density of states $\Delta_{0,min}$. However, it was later discovered [6] that the saturation could also be attributed to thermal decoupling of the sample from the thermometer. Thermal relaxation of tunneling states, cosmic rays, radiation from building material, ambient vibrations, and excessive strain excitation are all potentially significant sources of heat in low temperature experiments on dielectric glass. An analysis of the heat input to another glass sample from these sources is given in Ref. [6]; the primary contribution to thermal decoupling in that case was relaxation of the tunneling states, with a lesser contribution from cosmic rays. In the present experiment, we used a different type of oscillator, as described above, to reveal that the range over which the sound speed is logarithmic extends down to 2.5 mK. We have been unable to find a unique explanation for the weaker temperature dependence observed below 3 mK: it could be due to intrinsic physics or thermal decoupling. Additional innovations will be required to determine the intrinsic temperature dependence of the sound speed below 3 mK.

Figure 3.8 displays the sound speed measured with the double paddle oscillator at 14 kHz between 1 mK and 40 mK (solid circles). Also displayed in Figure 1 (open circles) is the sound speed measured with a cylindrical torsional composite quartz-silica oscillator at 84 kHz between 1 mK and 40 mK as reported in Ref. [6]. Both experiments show a logarithmic temperature dependence of the

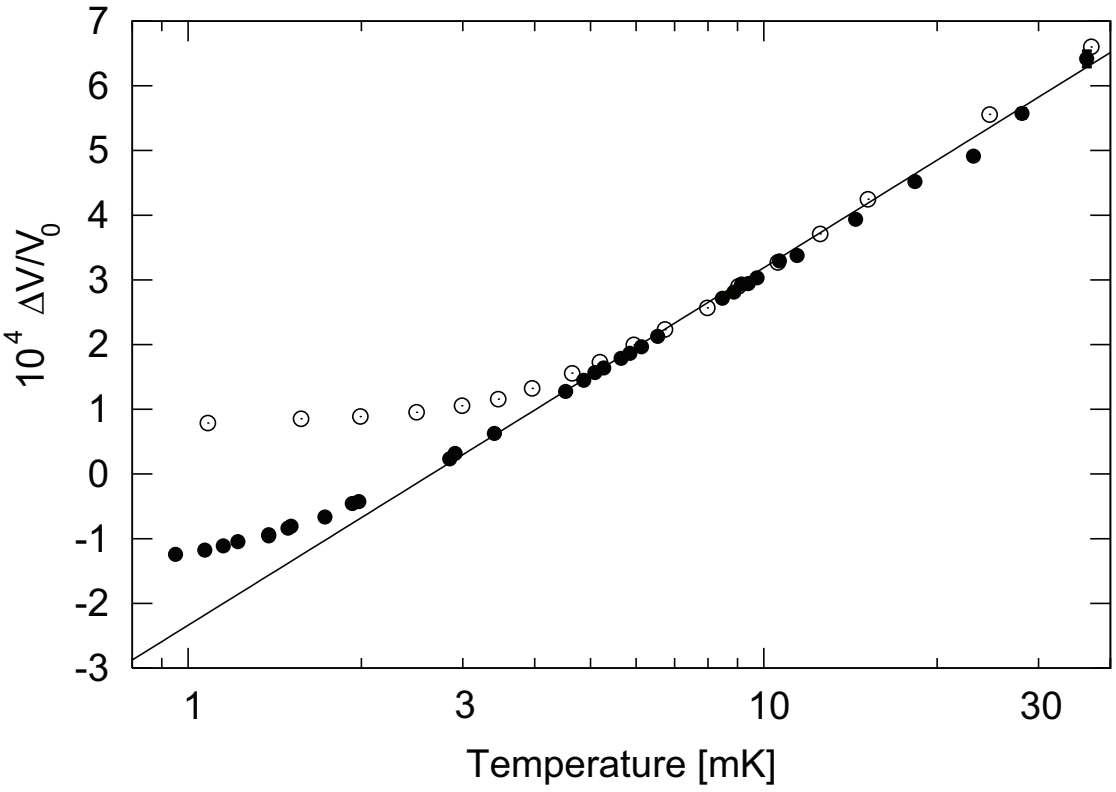

Figure 3.8: Speed of sound versus experimental plate temperature on a semi-logarithmic plot. Solid circles: present work, 14.0 kHz; open circles: taken from Fig. 4 of Ref. [6], 84 kHz. The solid line represents the logarithmic dependence predicted in Table 1.1 for $T << T_{CO}$.

sound speed above 6 mK, as predicted in Table 1.1 for $T << T_{CO}$, where T_{CO} is defined in Eq. 1.70. Below 6 mK, the sound speed in the composite oscillator shows an increasingly weak temperature dependence as temperature decreases. In contrast, the sound speed in the double paddle oscillator begins to level off from the logarithmic temperature dependence only below 3 mK.

The true logarithmic dependence of the sound speed between 6 mK and 3 mK was revealed because of the more than 100 times lower thermal resistance of the sample in the present experiment. To a lesser extent, the smaller mass

(and therefore decreased internal heat release) of the double paddle oscillator compared to the composite oscillator also contributed to a smaller temperature gradient between the sample and the thermometer. Since driving the oscillator into the nonlinear regime causes a decrease in the resonant frequency[52], nonlinear effects could counteract an apparent increase in the resonant frequency due to thermal decoupling. However, we were careful to drive the oscillator at a low enough strain so that any non-linearity had a negligible effect on the sound speed (Fig. 3.1).

In order to determine whether stray heat input is a reasonable explanation for the leveling off observed in the present experiment, we determined its magnitude. The thermal resistance between the sample and the experimental plate was measured by introducing a known heat input $\dot{Q}$ to the sample and measuring the resultant shift in sound speed. The heat input was provided by a gamma source situated outside the cryostat. The radiation significantly heated the sample (as evidenced by the shift in sound speed upon heating) but did not alter the temperature of the experimental plate (as evidenced by a negligible shift in the melting curve thermometer reading).

The gamma source for the thermal resistance measurements was ^{137}Cs. This isotope undergoes beta decay to metastable ^{137}Ba, which then emits gamma rays at 0.66 MeV upon relaxing to the ground state [53]. The power absorbed by the double paddle resonator is

$$\dot{Q}_{Cs} = A_r \Omega_p S_r \frac{E_{abs}}{E_\gamma} E_\gamma = 4.3 \times 10^{-13} \mathrm{W} \tag{3.12}$$

where $A_r = 7.4 \times 10^7$ Bq is the activity of the gamma source (nearly all of the ^{137}Cs decays lead to 0.66 MeV gamma emission). The solid angle subtended by

the double paddle resonator is given by

$$\Omega_p = A_p/4\pi L_s^2 \tag{3.13}$$

where $A_p = 1$ cm^2 is the surface are of the double paddle resonator and $L_s = 93$ cm is the distance between the source and the sample. The transmission factor $S_r = 0.9$, which specifies the fraction of γ quanta transmitted through the walls of the dewar and the metal in the magnet surrounding the sample region, was calculated in [54]. The energy absorption factor is given by

$$\frac{E_{abs}}{E_\gamma} = 1 - \exp[-(\mu/\rho)_{en}\rho l] = 6.7 \times 10^{-3}, \tag{3.14}$$

where $\rho = 2.2$ g/cm^3 is the density of vitreous silica and $l = 400$ microns is the path length of the γ quanta through the vitreous silica. The energy absorption cross section $(\mu/\rho)_{en} = 7.7 \times 10^{-2}$ cm^2/g for SiO_2 is given by summing the contributions of the bound electron incoherent absorption, the pair production absorption (zero for this gamma ray energy), and the photoelectric absorption coefficients [55, 56].

The measurement of sound speed versus temperature that was made without the cesium source was used to relate the sound speed shift upon gamma-induced heating to a temperature shift ΔT, yielding a thermal resistance $R_{th}(T) = \Delta T/\dot{Q}_{Cs}$. In fact, the appropriate value of ΔT depends on whether the leveling off in $\delta v/v_0$ is due to an intrinsic effect or thermal decoupling, as shown in Fig. 3.9. In each plot in Fig. 3.9, the lower dot corresponds to the $\delta v/v_0$ value before irradiating the paddle, and the upper dot corresponds to the steady state $\delta v/v_0$ value while irradiating the paddle. The horizontal axis corresponds to the melting curve thermometer temperature. In the left plot, ΔT is the change in temperature corresponding to a change δ in $\delta v/v_0$ assuming that the melting curve thermometer gives the true temperature of the double paddle

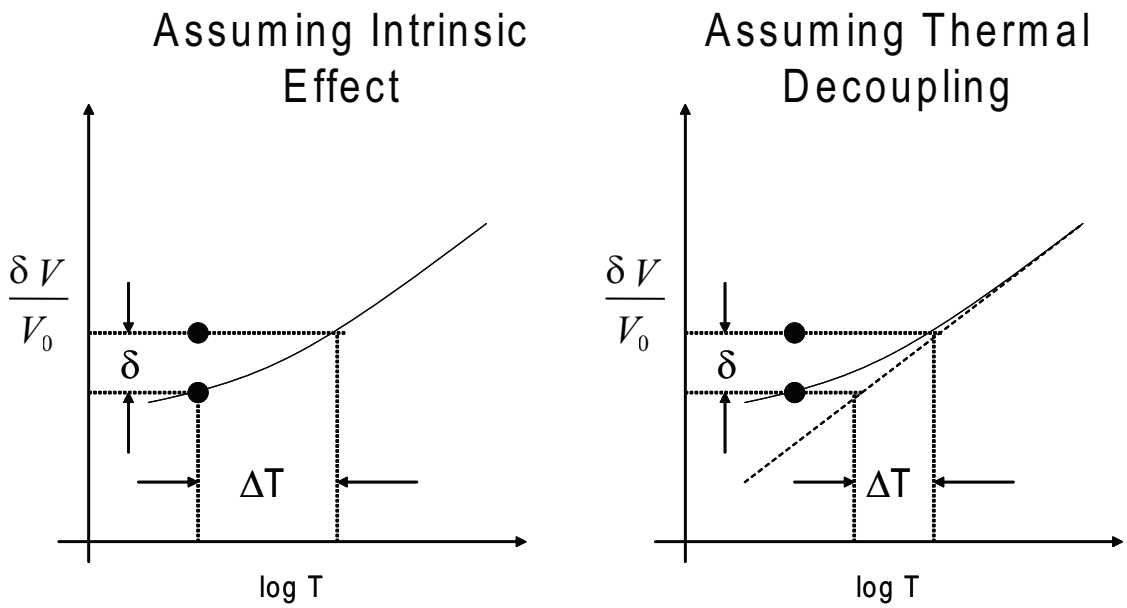

Figure 3.9: Demonstration of the appropriate value for ΔT in the radiation heating experiment if it is assumed that the leveling off in $\delta v/v_0$ is due to an intrinsic effect or thermal decoupling (see text).

resonator. In the right plot, ΔT is the change in temperature corresponding to a change δ in $\delta v/v_0$ assuming that the temperature dependence of $\delta v/v_0$ is given by an extrapolation of the $\log T$ dependence exhibited at higher temperatures. As shown in Fig. 3.10, the temperature dependence of the thermal resistance is independent of assumptions about the thermal coupling of thermometer to the glass sample. A function of the form

$$R_{th} = C_{th}/T^m \tag{3.15}$$

was fitted to the thermal resistance data in Fig. 3.10 with best fit values $m = 1.54$ and $C_{th} = 10^{4.75}$.

If thermal decoupling is responsible for the leveling off observed in the sound speed, it should be possible to fit to the lowest temperature data a func-

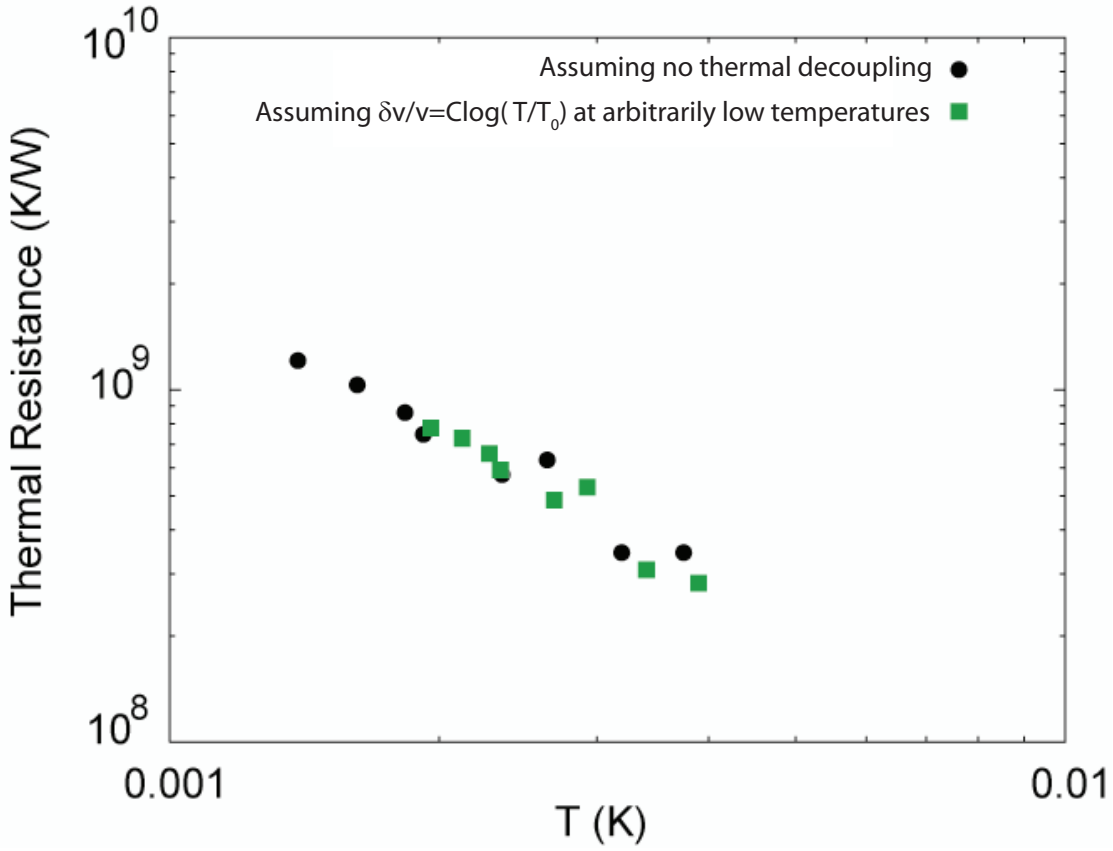

Figure 3.10: Thermal resistance of the vitreous silica double paddle resonator determined from irradiation measurements. The temperature dependence is independent of assumptions about the thermal coupling of the thermometer to the sample (see text).

tion of the form

$$\delta v/v_0 = C \ln T_H/T_0 \tag{3.16}$$

where T_H is the temperature of the double paddle resonator and T_0 is an arbitrary reference temperature. Using the expression for the heat flowing into the double paddle resonator

$$\dot{Q} = \int_T^{T_H} dT/R_{th} \tag{3.17}$$

and the expression for R_{th} from Eq. 3.15, we have

$$T_H = [(m+1)C_{th}\dot{Q} + T^{m+1}]^{1/m+1}, \tag{3.18}$$

where the parameters m and C_{th} are known from the fit to the thermal resistance measurements. Substituting Eq. 3.18 into Eq. 3.16 yields a function that can be fit to the lowest temperature measurements of $\delta v/v_0$ by varying the heat input $\dot{Q}$. A stray heat input of $\dot{Q} = 9 \times 10^{-4}$ nW would be required to produce the leveling off observed in the present work.

The saturation observed in Ref. [6] was modeled by a stray heat input of only 2×10^{-4} nW/g, and only a portion of this stray heat input was due to thermal relaxation. Therefore, under the assumption that the amount of thermal relaxation is not sample dependent, we conclude that the stray heat input due to thermal relaxation cannot account for the entire amount of heat necessary to produce the leveling off in the 0.1 g double paddle oscillator. No strain heating was observed in the present experiment, and heating due to radiation from building materials and cosmic rays was negligible compared to the required heat input.

In order to determine whether vibrational heating substantially contributed to the leveling off in $\delta v/v_0$, the oscillator was suspended over the experimental plate with a copper mass-spring system functioning as a vibrational filter, as shown in Fig. 2.1. The filter is a lightly damped oscillator with a few resonant frequencies ω_i. Ambient vibrations at frequencies ω above one filter resonance and not too close to another filter resonance are attenuated as $(\omega/\omega_i)^2$. If vibrations are attenuated at the paddle resonances, then paddle heating is reduced. Although it was not possible to calculate the resonant frequencies of the vibrational filter, the copper spring was annealed in order to lower the resonant frequencies of the filter. The filter caused a decrease in the heat input needed to

explain the leveling off from 15×10^{-4} nW to 9×10^{-4} nW. It is possible that even with the mass-spring filter in use, vibrational heating amounts to the remaining 9×10^{-4} nW of stray heat input in the present experiment.

If the leveling off of the sound speed observed below 3 mK is due to an intrinsic effect, it is not certain what the mechanism might be. A low temperature saturation is expected [57] in glasses composed of atoms with nuclear quadrupole moments, but the constituent atoms of silica do not have nuclear quadrupole moments. If the leveling off is due to an intrinsic effect, and if a subset of the TLS contributing to acoustic properties of the glass also contribute to its dielectric properties, one would expect to observe a leveling off of the dielectric constant at low temperatures as well. Saturation in the dielectric constant of SiO_x at low temperatures has been observed[58], but, as in the present work, heating from an external source could not be ruled out.

A possible explanation for the leveling off is a low energy cut off in the tunneling amplitude $\Delta_{0,\min}$. Such a cut off leads at low temperatures to the expression [51]

$$\frac{\delta v}{v_0} = C\left(\ln\frac{T}{T_0} + \frac{\Delta_{0,\min}/k_B}{2T}\right). \tag{3.19}$$

Fitting this function to the experimental data at all three frequencies leads to a best fit value of $\Delta_{0,\min}/k_B = 1.5$ mK. This value is in fair agreement with the results of other measurements: heat capacity measurements in vitreous silica in [59] lead to $\Delta_{0,\min}/k_B = 3.10$ mK and dielectric measurements on a-SiO_x in [58] lead to $\Delta_{0,\min}/k_B = 3.3$ mK. Although it has been argued that values for $\Delta_{0,\min}/k_B$ in the mK range are inconsistent with the long relaxation times observed for some tunneling states, this is a spurious argument according to [59]. However, the origin of a low energy cutoff in Δ_0 is not clear. One possibility

is that the maximum TLS barrier height is set by thermal energy available at the glass transition temperature, at which the structure of the glass is frozen in. In this case, one would expect glasses with a low glass transition temperature to have low maximum barriers and a high $\Delta_{0,\min}$ (Eq. 1.3) [58]. The polymer mylar should have a low glass transition temperature, yet no leveling off was observed in dielectric measurements on mylar [58], indicating a low $\Delta_{0,\min}$.

The origin of the leveling off in the present experiment might be determined by improving the design of the oscillator so that the thermal resistance between the sample and the thermometer is negligible. However, the result that we wish to emphasize is that a logarithmic temperature dependence of the sound speed, as predicted by the tunneling model without TLS interactions (Table 1.1 for $T << T_{CO}$), has been observed to a lower temperature (between 2 and 3 mK) in the present experiment than in previous experiments. The logarithmic behavior is not produced by overdriving the oscillator into the non-linear regime, and it is unlikely that any other factor could have artificially produced the logarithmic dependence. The logarithmic behavior is the intrinsic behavior down to 3 mK.

3.3 Contribution of the Ag film to Q^{-1}

The thickness of the silver film coating the vitreous silica double paddle resonator is optimal if it provides adequate thermalization of the glass substrate without significantly contributing to the dissipation of the composite resonator. In order to determine the contribution of the one micron Ag film to the dissipation of the composite vitreous silica resonator, a single crystal silicon double paddle resonator was used as a substrate to measure the internal friction in an-

other one micron Ag film.

The single crystal Si double paddle resonator is described in detail in [42]. It was etched from a wafer of 300 micron thick Si with the geometry shown in Fig. 3.11. Unlike in [42], an epoxy-free clamp was used in the present work, as shown in Fig. 3.11. The clamp assembly is made of invar, so that its thermal expansion is matched to that of Si [42]. The Si resonator can be operated in a number of modes, but the mode with by far the lowest dissipation is the second anti-symmetric torsional (AS2) mode [42]. The displacement profile and strain energy density for the AS2 mode calculated using the finite element method are shown in Fig. 3.12.

The AS2 mode has a resonant frequency of about 5.5 kHz. As shown in Fig. 3.11, a gold film was deposited onto part of the Si resonator in order to drive and detect its motion using an electrode structure similar to that used for the glass double paddle resonator. The gold film does not cover the upper torsion rod (the "neck") of the double paddle resonator, where the strain is concentrated, which means that the gold film does not contribute to the dissipation of the resonator. This region is where the sample, in this case a silver film, is deposited, as shown in Fig. 3.11.

The dissipation of the silicon paddle was determined from the time constant of free decay, i.e., the ring down technique. The drive and detect circuit was the same as in Fig. 2.4. With this technique, the silicon resonator was first driven on resonance with the function generator until the desired amplitude of motion was obtained. The drive was then turned off, and the reference to the lockin was simultaneously shifted off resonance so that the difference between the reference frequency and the resonant frequency was greater than the inverse time

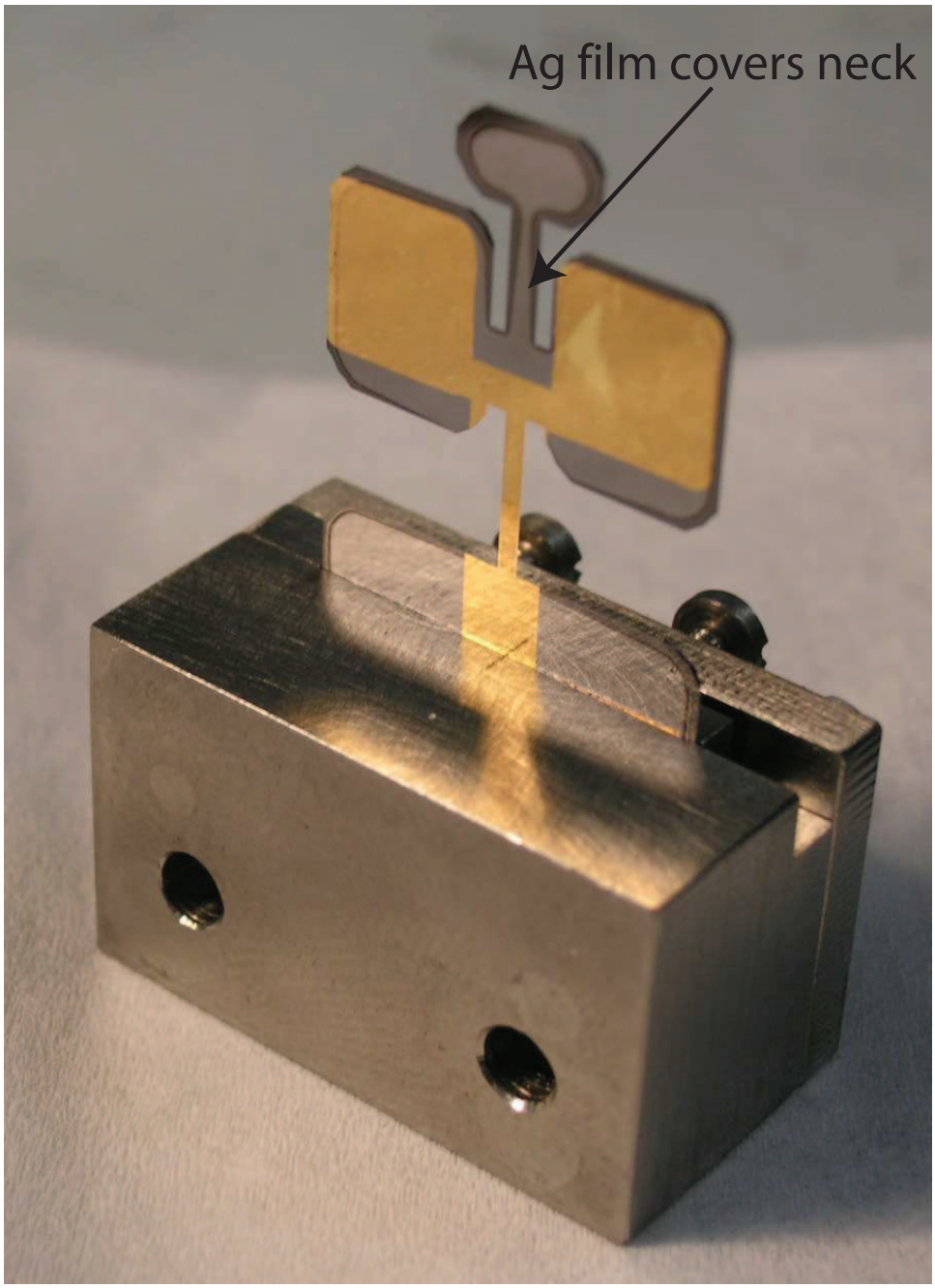

Figure 3.11: Photograph of a "bare" silicon double paddle resonator in the invar clamp assembly. The sample to be studied, in this case Ag, is deposited onto the "neck" (see Fig. 2.3), where the strain is concentrated (Fig. 3.12) [7].

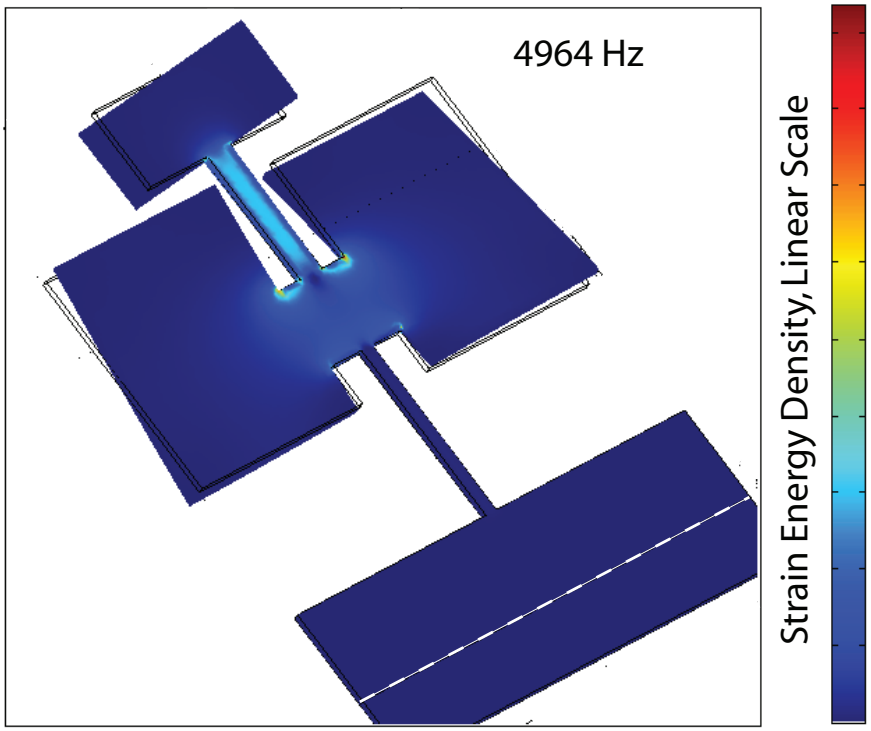

Figure 3.12: Displacement profile and strain energy density of the AS2 mode of the silicon double paddle resonator [7].

constant of free decay. This was done so that noise signals at the difference frequency would oscillate on a time scale much shorter than the decay of the resonator motion and thus would not influence the apparent decay time. The data was stored in the SR830 lockin buffer at the maximum rate that would not exceed the storage capacity of the buffer over the course of the ringdown, in order to avoid aliasing effects. We did not use Labview to periodically query the lockin output because the SR830 clock is more accurate than the Labview clock. A sample of raw data at 1.6 mK and with the silver film on the neck of the silicon substrate is shown in Fig. 3.13. The slope of the ring down on this log-linear

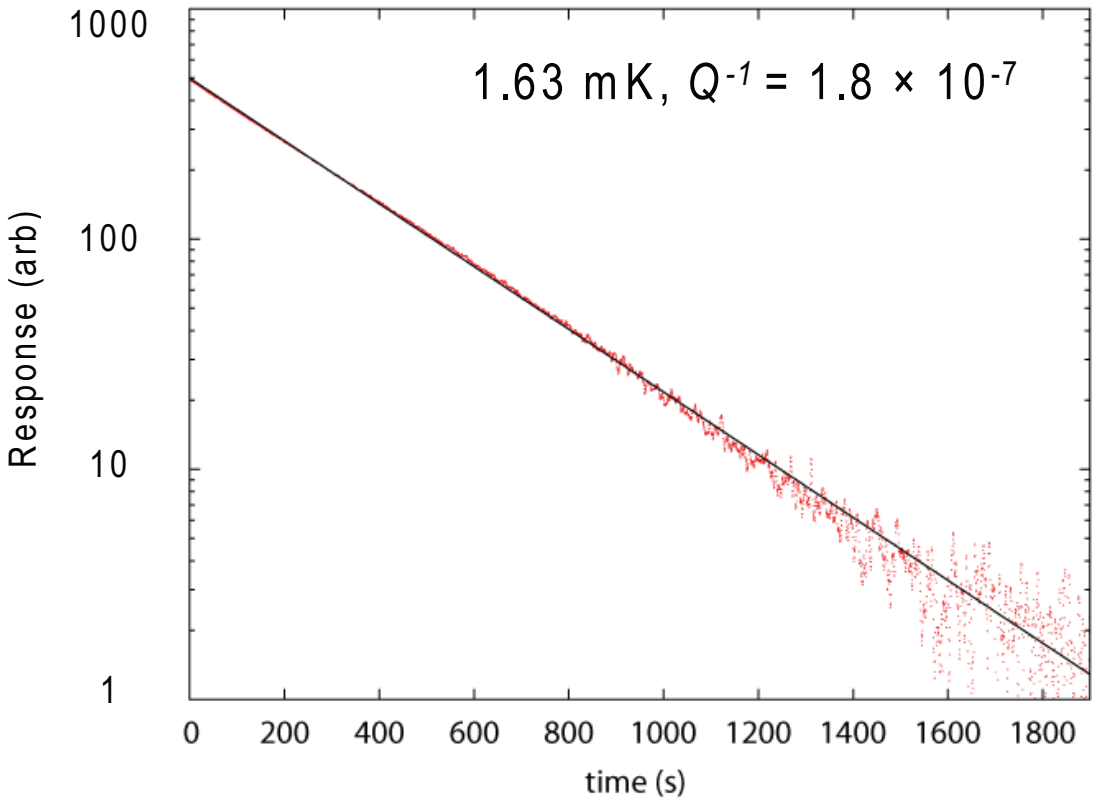

Figure 3.13: Example free decay of composite silicon/silver film double paddle resonator at 1.6 mK and best fit line.

scale is constant over more than two orders of magnitude in amplitude, indicating that we are operating in the linear regime and strain heating is negligible. At high amplitudes, the lockin data was compared with data obtained with the AC voltmeter function of the PAR 124 in order to verify that lockin detection was not skewing the data.

The internal friction of the silver film is related to that of the composite paddle and the bare substrate according to the equation [60]

$$Q_{film}^{-1} = \frac{G_s t_s}{3 G_f t_f} \left(Q_{paddle}^{-1} - Q_{bare}^{-1} \right) \tag{3.20}$$

where G_s (G_f)is the shear modulus of the substrate (film) and t_s (t_f) is the thick-

ness of the substrate (film). Equation 3.20 depends on the assumption that the thickness of the film is much less than that of the substrate. The shear modulus of silicon for common crystal orientations is given in [61], varying by about 30% as the direction is varied. Because I wanted to obtain an upper limit on the internal friction of the silver film, I used the maximum silicon shear modulus, 80 GPa. The shear modulus of bulk polycrystalline silver, 30 GPa, was used. Equation 3.20 neglects the interfacial contribution to the internal friction, but in a similar study of metal films that did not extend to such low temperatures [62] it was shown that Q^{-1}_{paddle} was linear in the film thickness for Au films as thin as 10 nm, indicating that the interfacial term is negligible.

The substrate internal friction Q^{-1}_{bare} and composite paddle internal friction Q^{-1}_{paddle} obtained from ring down measurements similar to that in Fig. 3.13 are shown in Fig. 3.14, along with the silver film internal friction Q^{-1}_{film} obtained using Eq. 3.20. It is not clear what limits the low temperature quality factor of the silver film. As with many other polycrystalline metal films, the low temperature internal friction observed in the Ag film is near the glassy range that spans $10^{-4} < Q^{-1} < 10^{-3}$ [62]. It is possible that dislocations in the polycrystalline silver film form tunneling states, leading to Q^{-1}_{film} near the glassy range.

Since the internal friction in the silver film is known, Eq. 3.20 can then be used to determine the contribution of the silver film to the dissipation of the composite glass/silver film resonator. The shear modulus of Suprasil 300 (the type of amorphous silica used for the present work) is 30 GPa. The background dissipation of the silver film along with the internal friction of the glass (i.e. without the contribution of the silver film) is shown in Fig. 3.15. It can be seen that the contribution of the silver film to the dissipation is negligible over

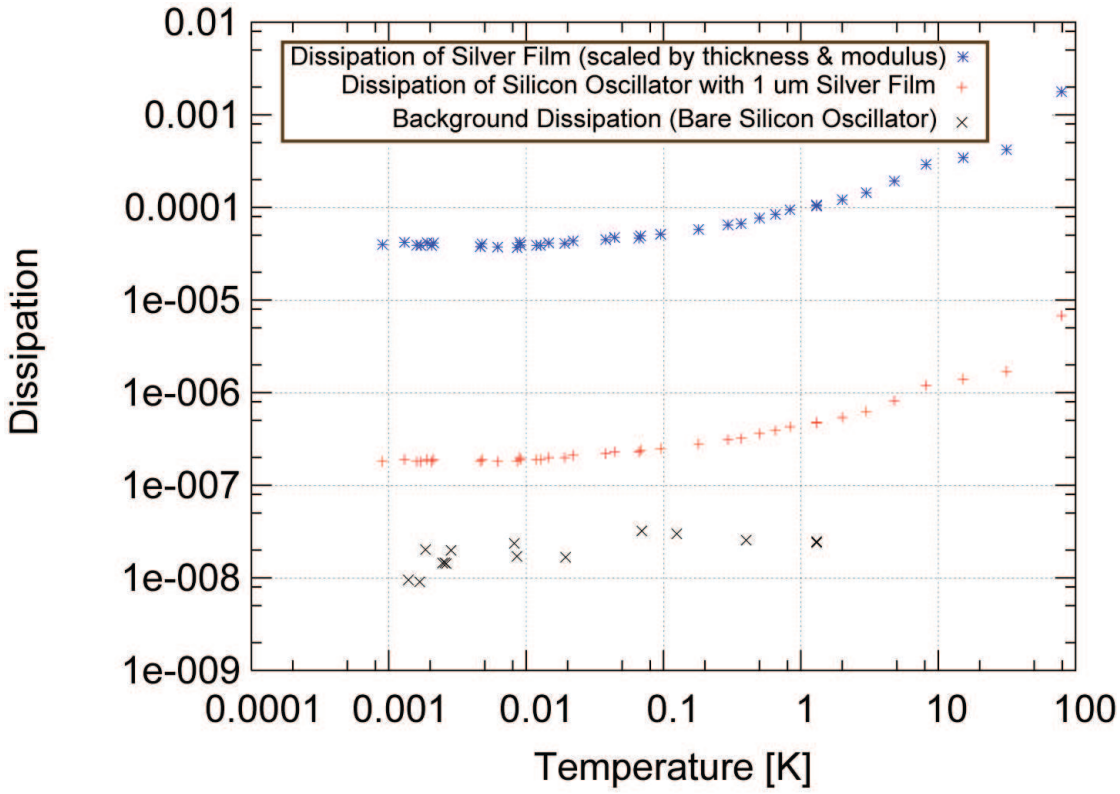

Figure 3.14: Dissipation of the bare Si substrate, the Si resonator with one micron thick Ag film, and the calculated internal friction of the Ag film.

most of the frequency and temperature range, but the contribution is small yet significant at 14 kHz at the lowest temperatures.

3.4 Conclusion

To conclude, after taking care to eliminate experimental artifacts such as non-linearity from our measurements, we observed a departure of Q^{-1} from the prediction of the STM below 10 mK and a $\approx 1 : -1$ ratio for the slopes $d(\delta v/v_0)/d(\log_{10} T)$. While the slope ratio could be accounted for by a modifica-

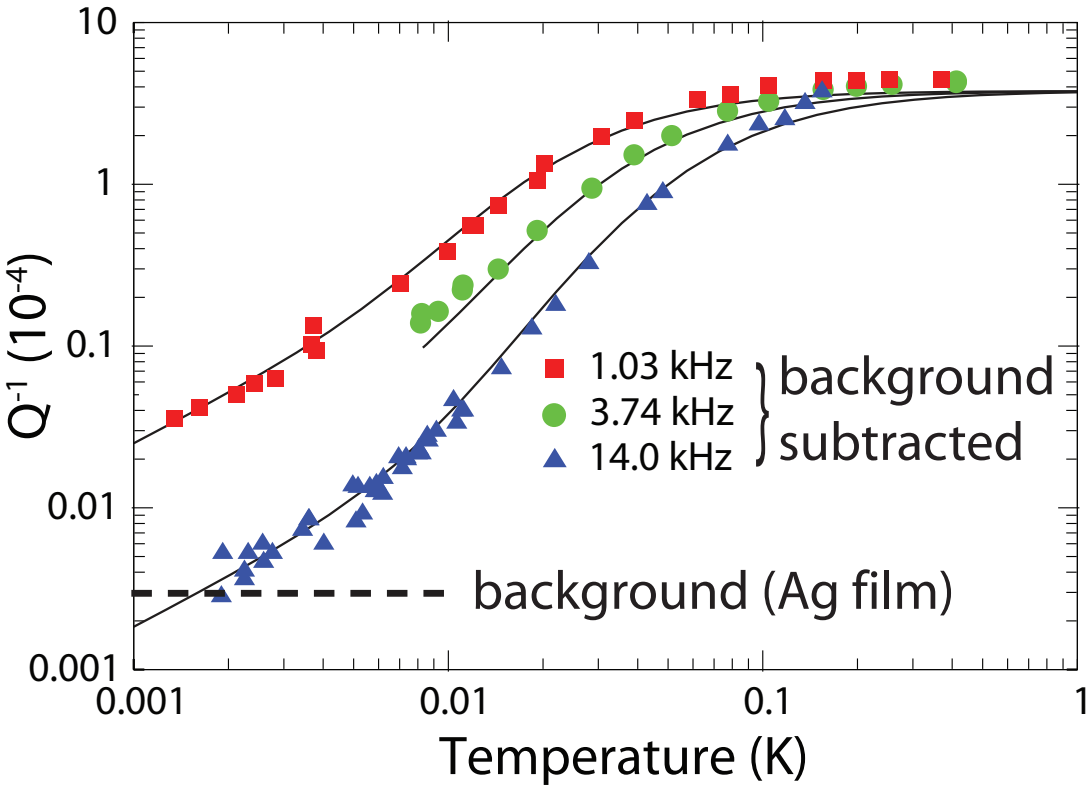

Figure 3.15: Contribution of the micron thick silver film to the dissipation of the glass resonator (labeled "background") as well as the internal friction of the glass (without the Ag film contribution). The lines are the same as the best fit lines in Fig. 3.3.

tion of the TLS distribution function, to our knowledge there is no reasonable modification that can account for the observed Q^{-1}. However, the observed Q^{-1} could be accounted for at all three frequencies by adding a single term, $\gamma_{\mathrm{tr,m}} = 1.0 \times 10^5\ T\ \mathrm{s}^{-1}\ \mathrm{K}^{-1}$, to the STM relaxation rate, motivated by theoretical work on interacting pairs of TLS [50]. While the theory of interacting pairs cannot predict the absolute value of the interaction-driven relaxation rate, it is argued in [35] that the prefactor needed to fit the present results is reasonable within that framework. Including the additional relaxation term did not degrade the quality of the fit to the Q^{-1} data above 10 mK, nor the fit to the $\delta v/v_0$

data over the entire temperature range. We conclude that the data are well described by the addition of a relaxation rate that is linear in temperature, but that the exact origin of the additional relaxation remains as a matter of theoretical debate. Thus, we have presented evidence that a refinement of the widely accepted standard tunneling model for glasses to account for interactions is necessary to describe the acoustic behavior of the prototypical glass, SiO_2, only below ≈ 10 mK.

CHAPTER 4

ACOUSTIC PROPERTIES OF A POLYCRYSTALLINE AL FILM

Here I review previous measurements of Q^{-1} and $\delta v/v_0$ in single crystal and polycrystalline aluminum in a variety of forms and present my measurements of these quantities in polycrystalline aluminum films. Well below the superconducting transition in aluminum at 1.19 K, the effect of electron quasiparticles on the acoustic properties is negligible [63]. In the previous measurements, some results were suggestive of glassy acoustic behavior, but it has not been possible to fit the data to the standard tunneling model. Here I show good agreement with the predictions of the standard tunneling model over a certain temperature range. In particular, I observed in my aluminum film a five-fold reduction in Q^{-1} at lowest temperatures relative to Q^{-1} in the plateau, with a temperature dependence that agrees with the standard tunneling model. Since the polycrystalline aluminum film consists of many single crystals of varied orientation, it is not immediately clear why the STM, which assumes a fully disordered lattice, should be applicable. It is possible that dislocation kinks form the low energy excitations, and that dissociation of the kinks leads to a low effective mass and energy barrier, allowing tunneling or thermally activated motion to occur [64].

In a perfect crystal, one expects a very low Q^{-1} and $\delta v/v_0 \propto -bT^4$ due purely to phonons [8]. However, even single crystals may have defects such as dislocations or impurities, and additional contributions to the temperature dependence of $\delta v/v_0$ and Q^{-1} are expected. Measurements of Q^{-1} and $\delta v/v_0$ for a single crystal aluminum reed of unknown purity at 5.0 kHz are presented in [8] and reproduced in Figs. 4.1, 4.2 and 4.3 (the work of Classen and cowork-

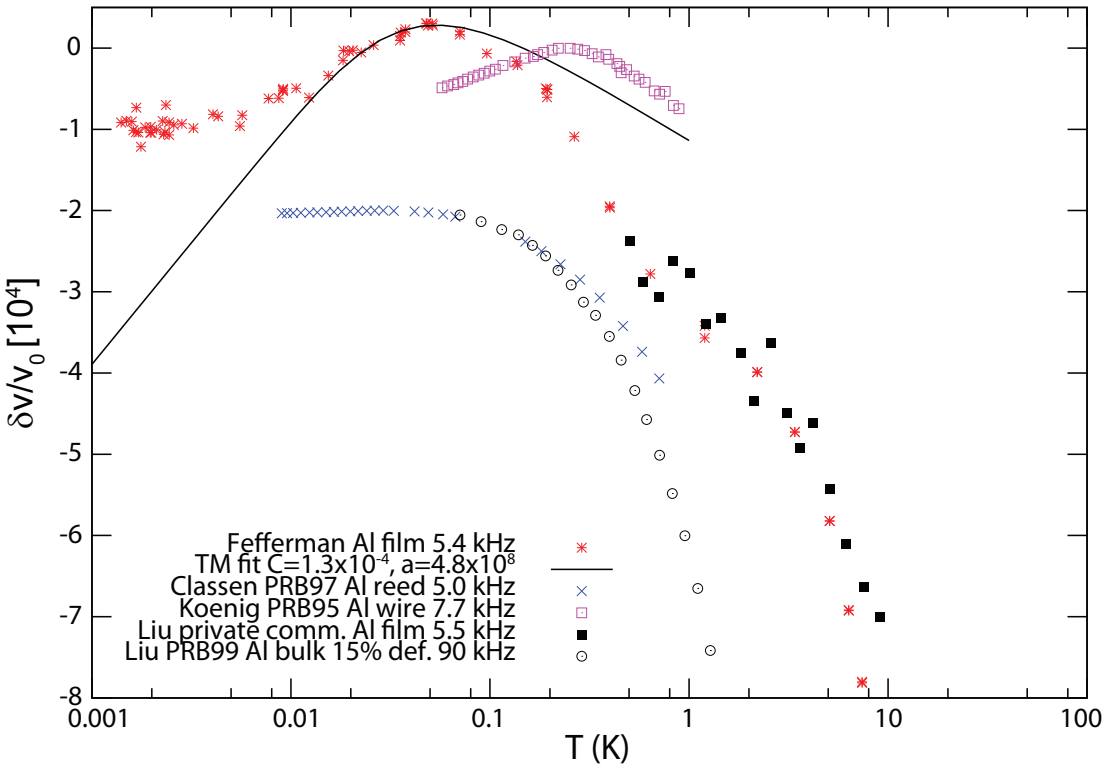

Figure 4.1: Measurements of $\delta v/v_0$ for several Al samples of different types (see legend). The tunneling model prediction for the same parameters used in Fig. 4.3 is compared with my measurements of $\delta v/v_0$.

ers). The approximate reed dimensions were 10 mm x 3 mm x 0.3 mm. At the lowest temperatures, $\delta v/v_0$ exhibits a nearly logarithmic dependence on temperature as expected in glassy systems, as shown on the expanded scale in Fig. 4.2. However, at temperatures just above that of the maximum in $\delta v/v_0$, the slope $d(\delta v/v_0)/d(\log_{10} T)$ is much greater than at low temperatures, in disagreement with the tunneling model predictions (Table 1.1). Also, the plateau in Q^{-1} expected between 1 K and the inflection point of the slope $d(\delta v/v_0)/d(\log_{10} T)$ at 30 mK is not observed (Fig. 4.3). While Q^{-1} is well below the glassy range, it is still much greater than that predicted by the tunneling model based on the low

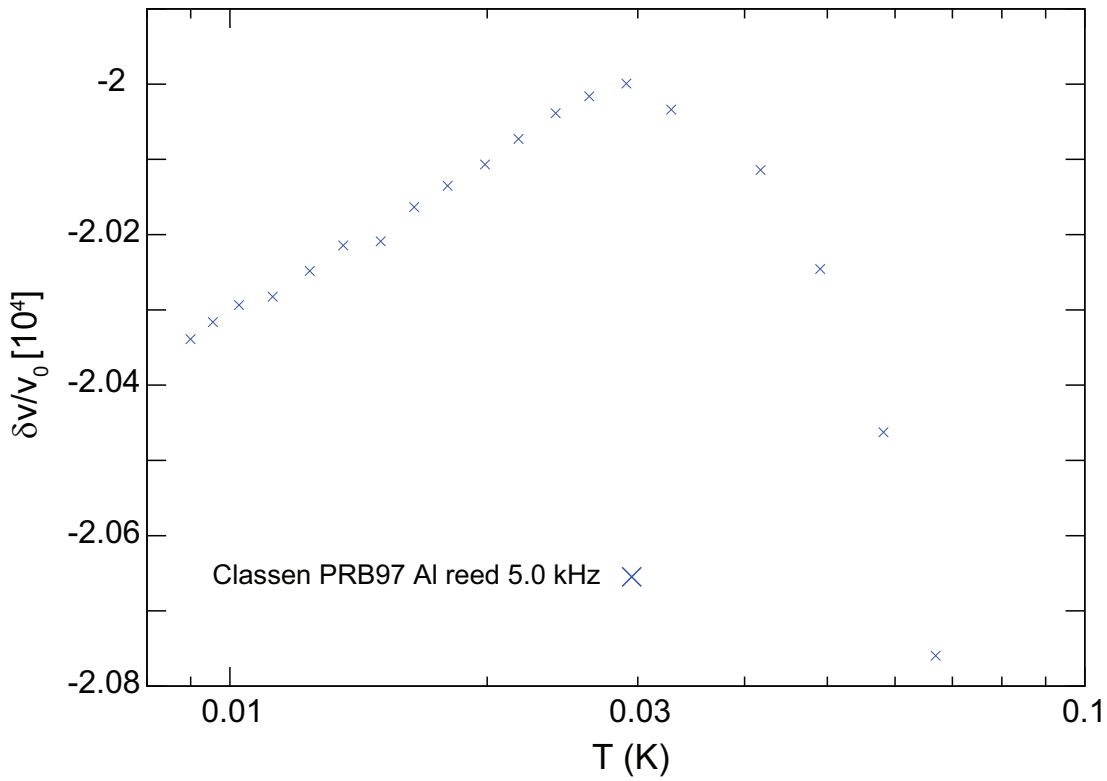

Figure 4.2: Measurements of a single crystal Al sample [8]. These are the same data as in Fig. 4.1, but plotted on an expanded scale.

temperature slope $d(\delta v/v_0)/d(\log_{10} T)$ (Table 1.1). Thus the acoustic properties of the single crystal aluminum reed are not in agreement with those expected from the standard tunneling model.

Good agreement with the standard tunneling model over a certain temperature range was observed in my measurements of a one micron thick polycrystalline aluminum film. The aluminum film was deposited on a single crystal silicon double paddle resonator, which was described in Section 3.3. The entire surface without the gold electrodes was coated with aluminum using a thermal evaporator in the Schwab lab at Cornell. I decided to keep the resonator in its invar clamp during the deposition to avoid clamping the resonator directly to the

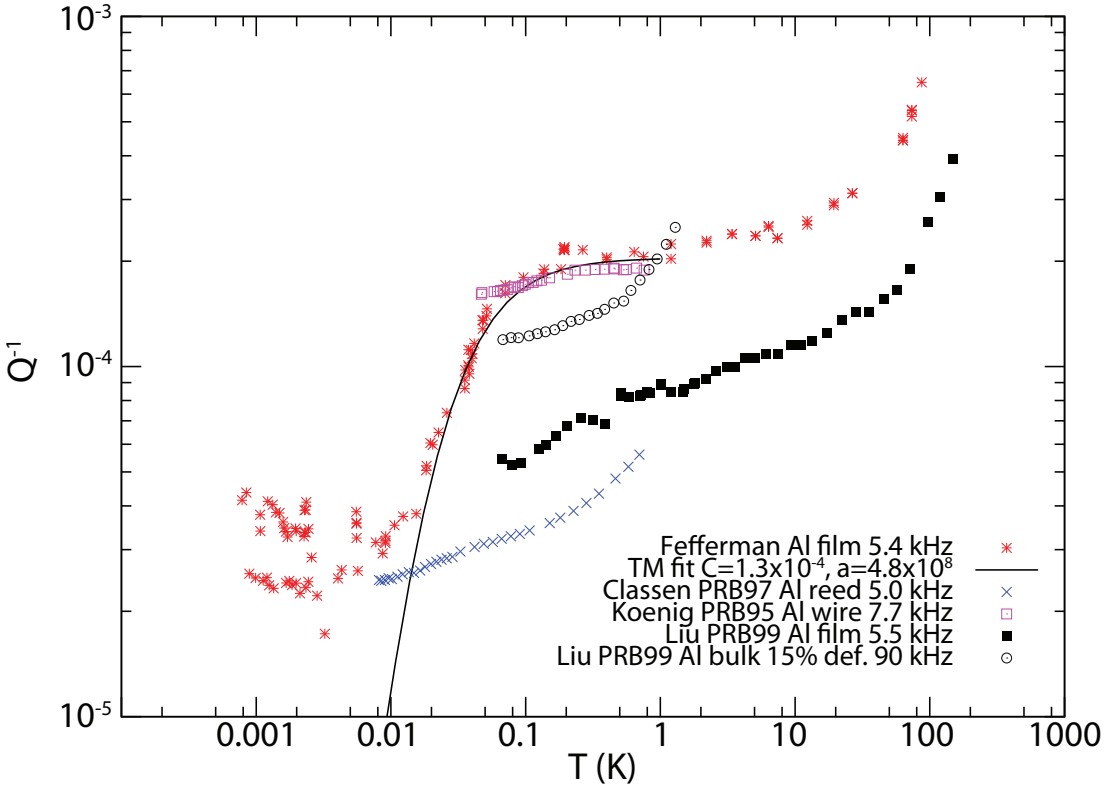

Figure 4.3: Measurements of Q^{-1} for several Al samples of different types (see legend). The tunneling model prediction that best fits my measurements of Q^{-1} is shown.

evaporator stage and risking scratches in the gold film electrodes. The evaporator stage was coupled to a heat sink cooled by circulating liquid nitrogen, and this cooling scheme resulted in high quality films in the past. During deposition, thermal radiation from the evaporator typically elevated the temperature of the evaporation stage to $\approx$ 200 K. The thermal resistance between the double paddle resonator and the evaporator stage probably resulted in substantial elevation of the resonator temperature relative to the evaporation stage. The relatively high temperatures at which deposition took place resulted in some large scale defects in the aluminum film, as shown in Fig. 4.4. The grains in the poly-

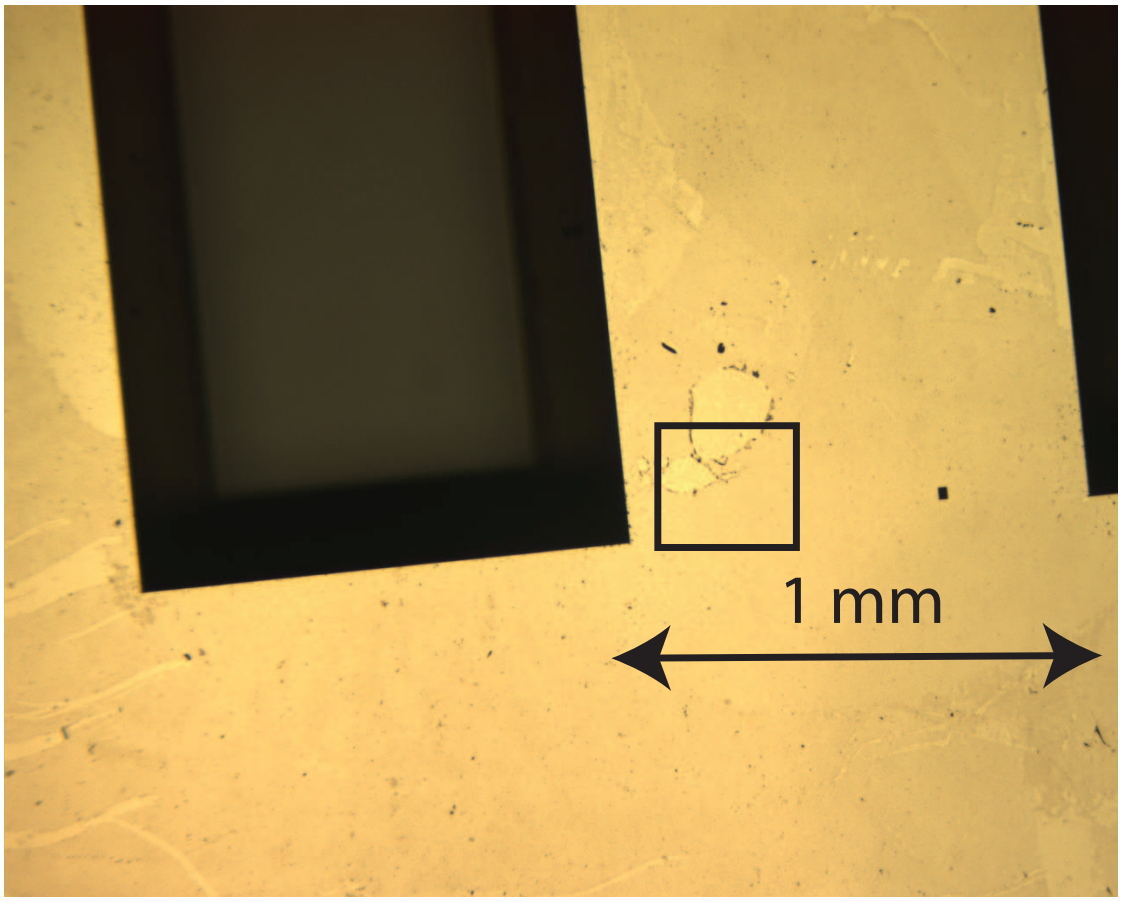

Figure 4.4: Photograph of the one micron thick aluminum film sample, showing some large scale defects. The black square borders the approximate region that is enlarged by a factor of ten in Fig. 4.5.

crystalline film are visible in Fig. 4.5, which is a photograph of the aluminum film at higher magnification.

The method for measuring Q^{-1} in the aluminum film is the same as was described for the silver film in Section 3.3 and the result is shown in Fig. 4.3 (labeled "Fefferman Al film"). The Q^{-1} plateau observed between 100 mK and 10 K is within the glassy range $2 \times 10^{-4} < Q^{-1} < 2 \times 10^{-3}$. Between 100 mK and 10 mK, Q^{-1} of the aluminum film decreases. In the context of the standard tunnel-

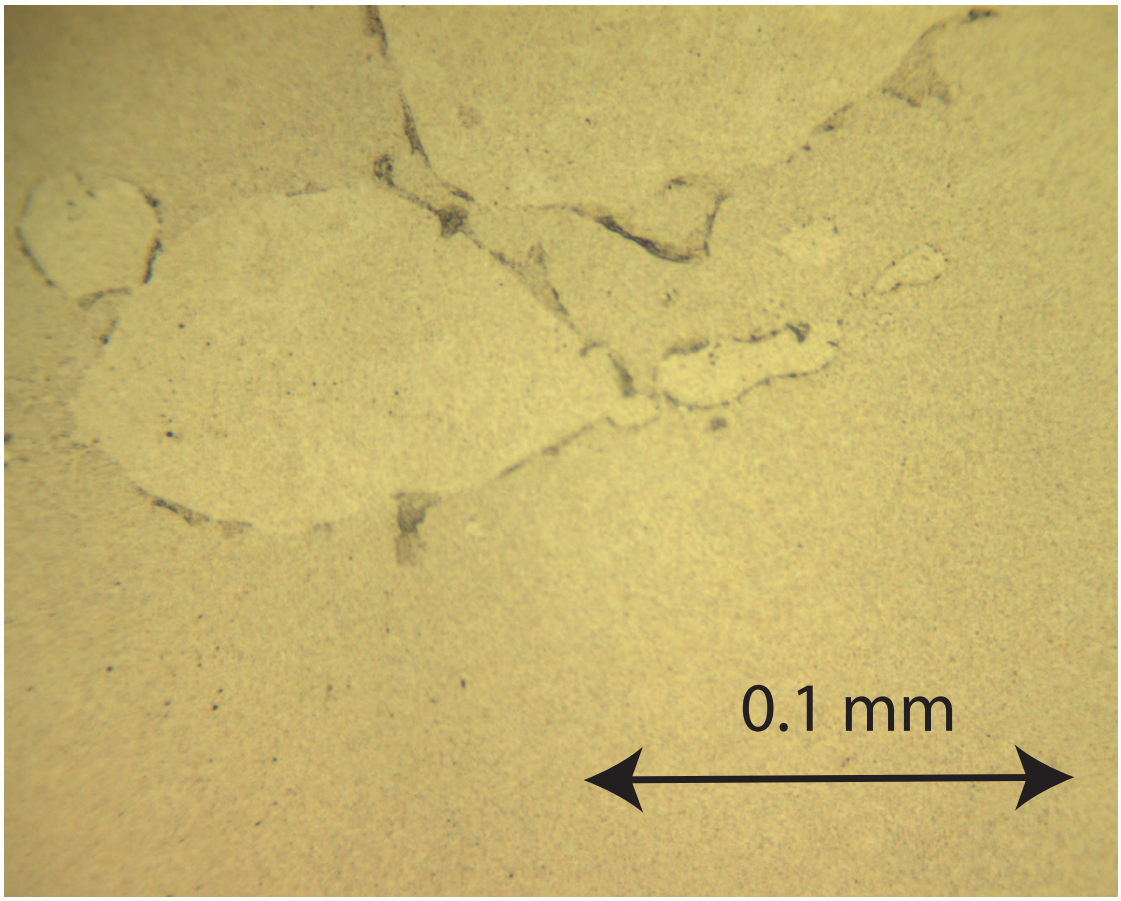

Figure 4.5: Photograph of the one micron thick aluminum film sample showing crystallites and large scale defects, at ten times higher magnification than in Fig. 4.4.

ing model, this "shoulder" at 100 mK would be interpreted as a decrease of the relaxation rate of the dominant two level systems below the driving frequency. Below 10 mK, the Q^{-1} is nearly temperature independent and is somewhat non-reproducible. Such non-reproducibility could originate from overdriving the resonator and altering the dislocation structure. However, at certain temperatures below 10 mK, low Q^{-1} was observed both before and after observations of high Q^{-1}. Since the change in Q^{-1} is not permanent, the over-driving explanation seems unlikely. The prediction of the standard tunneling model with best

fit single phonon relaxation rate prefactor $a = 4.8 \times 10^8$ $\mathrm{K^{-3}s^{-1}}$ and tunneling strength $C = 1.3 \times 10^{-4}$ is also shown in Fig. 4.3. The temperature dependence of the data is weaker than expected below 10 mK, perhaps due to thermal decoupling of the sample from the melting curve thermometer. The internal friction rises above the tunneling model prediction for temperatures well above 1 K, as seen in most amorphous solids.

The $\delta v/v_0$ for my aluminum film was determined by subtracting the contribution from the bare silicon substrate from the $\delta v/v_0$ of the composite paddle according to the formula [65]

$$\left(\frac{\Delta v}{v_0}\right)_{film} = \frac{1}{3}\frac{G_{sub}t_{sub}}{G_{film}t_{film}}\delta\left(\frac{\Delta f}{f_0}\right) + \left(\frac{\Delta v}{v_0}\right)_{sub} \tag{4.1}$$

where

$$\delta\left(\frac{\Delta f}{f_0}\right) = \left(\frac{\Delta f}{f_0}\right) - \left(\frac{\Delta f}{f_0}\right)_{sub}. \tag{4.2}$$

The result is shown in Fig. 4.1, along with the predictions of the standard tunneling model for the same parameters $a = 4.8 \times 10^8$ $\mathrm{K^{-3}s^{-1}}$ and $C = 1.3 \times 10^{-4}$ that were used to fit to Q^{-1}. There is good agreement with the prediction of the tunneling model for $10\ \mathrm{mK} < T < 100\ \mathrm{mK}$. Below 10 mK, $\delta v/v_0$ continues to decrease down to a temperature near 4 mK. However, the temperature dependence below 10 mK is weaker than that predicted by the tunneling model, as with Q^{-1} in the same temperature range, perhaps due to thermal decoupling of the sample from the melting curve thermometer. Between 100 mK and 1 K, the temperature dependence of the $\delta v/v_0$ data is weaker than that predicted by the standard tunneling model. This weak temperature dependence above the crossover temperature has been seen in most amorphous solids, including amorphous SiO_2, as shown in Fig. 3.2.

In [66], König and coworkers present measurements on a polycrystalline aluminum vibrating wire, and these also have qualitative similarities to the predictions of the standard tunneling model, although it is not possible to fit the tunneling model predictions to the data. The vibrating wire had a diameter of 25 microns, a length of a few millimeters, a resonant frequency of 7.7 kHz, and a purity of 4N. It was commercially available [66], which indicates that it underwent considerable plastic strain during the manufacturing process, which must have introduced a high density of dislocations. The $\delta v/v_0$ and Q^{-1} results are shown in Figs. 4.1 and 4.3. The Q^{-1} measured by König *et al* agrees very well with the Q^{-1} of my aluminum film. König *et al* measure roughly equal slopes $d(\delta v/v_0)/d(\log_{10} T)$ on either side of the maximum in $\delta v/v_0$, as observed in other glasses, including amorphous SiO_2, as shown in Fig. 3.4. However, the maximum in $\delta v/v_0$ occurs at 250 mK, which is about five times the temperature of the maximum in $\delta v/v_0$ for my aluminum film. Thus if the tunneling model parameters were determined by the temperature of the maximum in the $\delta v/v_0$ measured by König *et al*, the predicted Q^{-1} would not agree with their measurements. Rather, the expected Q^{-1} temperature dependence would be much stronger than what was observed below 250 mK. The $\delta v/v_0$ data could be affected by experimental artifacts: their data were taken at a strain of $\approx 9 \times 10^{-5}$, and they showed that strain dependent effects at this strain level were very important in another aluminum wire vibrating at 323 Hz (Fig. 9 in [66]).

In [62], Liu *et al* studied Q^{-1} in several metal films, including aluminum, using the same double paddle resonator technique that I used. These data are shown in Figs. 4.1 and 4.3. The aluminum film they studied was also one micron thick, although electron beam deposition was used. For an unknown reason, at 200 mK the Q^{-1} of the aluminum film measured by Liu *et al* is three times lower

than the Q^{-1} of my aluminum film, as shown in Fig. 4.3. Our measurements of $\delta v/v_0$, however, agree over the entire temperature range at which data is available, as shown in Fig. 4.1.

Pohl and coworkers have studied the effect of plastic deformation on the acoustic and thermal properties of bulk aluminum [62, 67, 68]. The plastic deformation is thought to produce a dislocation density n_{disl} =(10^{11} cm^{-2})ϵ_{plas}, where ϵ_{plas} is the plastic strain. The internal friction and magnitude of $d(\delta v/v_0)/d(\log_{10} T)$ increases up to dislocation densities of $\approx 10^{10}$ cm^{-2} or $\epsilon_{plas} \approx 15\%$. Above this deformation level, it is thought that the dislocation density increases to a point at which dislocation-dislocation interactions limit further contributions to the acoustic properties. Measurements of Q^{-1} and $\delta v/v_0$ for 15 % plastically deformed Al are shown in Figs. 4.1 and 4.3. The Q^{-1} of the deformed aluminum is in the glassy range [62], which spans $2 \times 10^{-4} < Q^{-1} < 2 \times 10^{-3}$, and is close to the Q^{-1} of my aluminum film between 100 mK and 1 K. This suggests that the origin of the Q^{-1} in my aluminum film is related to dislocations [62]. The $\delta v/v_0$ for the deformed Al decreases as the temperature increases from 100 mK to 1 K, as expected for an amorphous solid oscillating at kilohertz frequencies, but there is more curvature than expected when the data are plotted on a logarithmic scale. The $\delta v/v_0$ in fact has a linear temperature dependence, which is observed in amorphous solids as well, albeit at temperatures above a few Kelvin.

Given the good agreement between my aluminum film measurements and the predictions of the tunneling model, as well as the evidence from plastically deformed bulk aluminum that dislocations can produce Q^{-1} in the glassy range, it seems useful to consider models for two level systems formed by dislocations.

Dislocations are one-dimensional defects in crystals. In the neighborhood of a dislocation, the atomic positions are substantially different from the positions expected in a perfect crystal. Far from the dislocation (and other defects), the atoms are almost perfectly ordered [10, 69]. The periodic lattice surrounding a dislocation produces a periodic potential known as the Peierls potential. If a stress greater than the Peierls stress is applied, a dislocation can surmount the barriers in the periodic potential and glide through the lattice. If a crystal contains dislocations, its yield strength is much less than that predicted for a perfect crystal. For FCC metals, the Peierls stress $\sigma_p \leq 10^{-5}G$ [69], where G is the shear modulus (26 GPa in the case of aluminum). Kinks in the dislocation line can glide at a much lower stress known as the kink Peierls stress. Numerical simulations for a dislocation kink in copper yielded an activation energy for kink motion of 2 mK [64]. This very low barrier height was attributed to the width of the dislocation kinks. The spatial extension of the kink also leads to a low effective mass. The combination of low effective mass and low barrier leads to a relatively large tunneling amplitude (Eq. 1.3). According to [64] dislocation kinks "are likely the only candidate for quantum tunneling in pure fcc metals". If external static strain modulates the kink Peierls potential on an energy scale much greater than the kink Peierls barriers and on a length scale much greater than wavelength of the kink Peierls potential (i.e. the lattice constant), then nearly symmetric kink two level systems can form in the minima of the long length scale fluctuations. These minima would be preferentially occupied, leading to an excess of nearly symmetric two level systems. [28]

The good agreement between my measurements of the acoustic properties of a polycrystalline aluminum film and the predictions of the standard tunneling model provide support to the notion that some sort of two level systems

are responsible for the acoustic properties of my aluminum film. However, the phonon mean free path in aluminum films in [68] derived from heat conductivity measurements is much shorter than that predicted by the tunneling model based on the measurements of Q^{-1} in [62]. In addition, the excess specific heat with linear temperature dependence and time dependent heat release predicted by the tunneling model is not observed in plastically deformed aluminum [67]. The lack of glassy anomalies in the specific heat and heat release might be explicable in terms of the tunneling model by an abundance of symmetric tunneling states relative to asymmetric tunneling states [67], as would be expected if TLS form at the minima of long wavelength modulations of the kink Peierls potential. However, this still leaves the discrepancy between internal friction and thermal results. A radiation damping model was discussed in [70, 67]. However, it is assumed in [70] that the barrier height, stress energy and kink-kink interaction energies are all much less than the temperature. Thus the driven motion of the kinks would be adiabatic and the drive phonons cannot be attenuated [28]. At present, there does not seem to be a completely satisfactory explanation for my measurements of the elastic properties of the aluminum film.

APPENDIX A

MATHEMATICA TUNNELING MODEL CALCULATION

Here I reprint the Mathematica code that was used to fit the modified tunneling model (including interaction-driven relaxation and a modified TLS distribution function) to my acoustic measurements on the SiO_2 double paddle resonator. Comments are interspersed in the ordinary font used in the rest of this dissertation.

<< Graphics`

Ct $= 2.86$; tunneling strength as defined in Eq. 1.37

$a = 6.0 * 10^7$; prefactor of single phonon relaxation rate defined in Eq. 1.65

$b = 1.0 * 10^5$; prefactor of interaction driven relaxation rate

$\mu = 0.09$; TLS distribution parameter

kb $= 1.4 * 10^{-23}$;

hbar $= 1.05 * 10^{-34}$;

angfreqs $= \{2\pi 1.03 * 10^3, 2\pi 3.74 * 10^3, 2\pi 14.0 * 10^3\}$;

Emax $=$ **20kb**; upper limit of energy integral

tmin $= 0.001$; minimum temperature in calculation in Kelvin

tmax $= 1.00$; maximum temperature in calculation in Kelvin

tsteps $= 29$;

temps $=$

Table[**Exp**[t], {t, **Log**[**tmin**], **Log**[**tmax**], (**Log**[**tmax/tmin**])/**tsteps**}];

$\mathbf{maxrate[en\_, T\_]:=\frac{a}{kb^3}en^3Coth\left[\frac{en}{2*kb*T}\right]+bT}$ maximum relaxation rate at energy E, i.e., for a TLS with no asymmetryΔ

$\mathbf{P[r\_, en\_]:=\frac{1}{2r}(1-r)^{\mu-0.5}}$ TLS distribution from [5] with $r=(\Delta_0/E)^2$, which reduces to distribution in [11] for $\mu=0$

$\mathbf{int[T\_, Emax\_, \omega\_]:=}$
$\mathbf{\frac{Ct}{kb*T}NIntegrate\left[P[r, en]\frac{1-r}{Cosh\left[\frac{en}{2*kb*T}\right]^2}\frac{ir*maxrate[en,T]}{\omega+ir*maxrate[en,T]},\right.}$
$\mathbf{\left.\{en, 0, Emax\}, \{r, 0, 1\}, MaxRecursion\rightarrow 12\right]}$ Integration of $M_{rel}/\rho v^2$ over the distribution of TLS, where M_{rel} is from Eq. 1.61. Note that ρv^2 and P_0, the prefactor of the TLS distribution, are included in Ct

$\mathbf{results = Array[1, \{tsteps+1, 3, 3\}];}$
$\mathbf{Do[results[[i, 1, j]] = temps[[i]];}$
$\mathbf{results[[i, 2, j]] = -0.5Re[int[temps[[i]], Emax, angfreqs[[j]]]]+}$
$\mathbf{Ct\frac{Beta[1,\mu+0.5]}{2}}$
$\mathbf{\left(Re\left[PolyGamma\left[0.5+\frac{hbar*angfreqs[[j]]}{2\pi i*kb*temps[[i]]}\right]-\right.\right.}$
$\mathbf{\left.\left.Log\left[\frac{hbar*angfreqs[[j]]}{kb*temps[[i]]}\right]\right]\right);}$
$\mathbf{results[[i, 3, j]] = Im[int[temps[[i]], Emax, angfreqs[[j]]]];,}$
$\mathbf{\{i, Length[temps]\}, \{j, 3\}]}$ Filling a three dimensional array that contains Q^{-1} and $\delta v/v_0$ data for a range of temperatures and the three frequencies. Note the factor of -0.5 for the relaxational contribution to the sound speed. The resonant contribution to the sound speed is from Eq. 1.80. Because an arbitrary reference temperature T_0 must be used to measure $\delta v/v_0$ (since we do not know the zero temperature sound speed), a constant must be added to the theoretical sound speed in order to fit the data.

APPENDIX B

PYTHON CALCULATION OF $\delta C/C$

```
#This version uses several integration regions to calculate the capaciatance
#integrates over just the region of the electrode that overlaps with the Ag film

import os
from scipy import *
import pylab
os.chdir('C:\\Documents and Settings\\H-13\\My Documents\\python\\fits')
import read_spreadsheet
#reload(read_spreadsheet)
from scipy.optimize import fsolve



#return the inverse distance between capacitor plates in mm^-1 as
#a function of position assuming 0.01 nm peak displacement
def dinv(y,x):
    return 1/(1.0e-8*interpolate.bisplev(x,y,tck)+0.058)

os.chdir('C:\\Documents and Settings\\H-13\\My Documents\\Paddle\\FEM simulation')

displacement=read_spreadsheet.read_spdsht('node label vs displacement.txt')
nodecor=read_spreadsheet.read_spdsht_special('node coordinates.txt')
left_elect=read_spreadsheet.read_spdsht('left_elect Ag film region Sept 26.txt')
right_elect=read_spreadsheet.read_spdsht('right_elect.txt')
border=read_spreadsheet.read_spdsht('paddle_border.txt')

#subtract off y-offset of node coordinates
nodecor[2,:]=nodecor[2,:]-sort(nodecor[2,:])[0]

pylab.figure(1)
pylab.plot(nodecor[1,:],nodecor[2,:],',b')
```

```
#pylab.plot(border[0,:], border[1,:],'.r')
pylab.plot([left_elect[0,0],left_elect[0,1],left_elect[0,3],left_elect[0,2],\
            left_elect[0,0]],[left_elect[1,0],left_elect[1,1],left_elect[1,3],\
                              left_elect[1,2],left_elect[1,0]],'-g')
pylab.plot(right_elect[0,:], right_elect[1,:], '-g')

#make an array with left wing displacement:
wing=array([[],[],[]],pylab.Float)
for ii in range(3199):
    if (nodecor[1,ii]>-6.1 and nodecor[1,ii]<-1.8 and nodecor[2,ii]>5 and\
        nodecor[2,ii]<12):
        wing=concatenate((wing,[[nodecor[1,ii]], [nodecor[2,ii]],\
                                [displacement[1,ii]]]),axis=1)

#create bivariate spline interpolation of the wing displacement
#(interpolate is a subpackage of scipy)
#see help(interpolate.bisplrep) or the PDF by Oliphant for an explanation of tck
tck=interpolate.bisplrep(wing[0,:],wing[1,:],wing[2,:], kx=5, ky=5, quiet=0)

#make a contour plot of the wing displacement
pylab.figure(2)
x1=arange(-6.1,-1.8,0.05)
y1=arange(5.5,11.5,0.05)
#[X1, Y1]=meshgrid(x1,y1)
#pylab.contour(X=x1,Y=y1,Z=transpose(interpolate.bisplev(x1,y1,tck)),V=[0.0])
CS=pylab.contour(x1,y1,transpose(interpolate.bisplev(x1,y1,tck)),colors='k')
pylab.clabel(CS, inline=1)

#compute [slope, intercept] of lines between electrode corners
E=left_elect[:,0]
F=left_elect[:,1]
G=left_elect[:,2]
H=left_elect[:,3]
```

```
HG=[0.0,0.0]
GE=[0.0,0.0]
FE=[0.0,0.0]
HF=[0.0,0.0]
HG[0]=(left_elect[1,2]-left_elect[1,3])/(left_elect[0,2]-left_elect[0,3])
GE[0]=(left_elect[1,0]-left_elect[1,2])/(left_elect[0,0]-left_elect[0,2])
FE[0]=(left_elect[1,0]-left_elect[1,1])/(left_elect[0,0]-left_elect[0,1])
HF[0]=(left_elect[1,1]-left_elect[1,3])/(left_elect[0,1]-left_elect[0,3])
HG[1]=fsolve(lambda b: left_elect[1,2]-HG[0]*left_elect[0,2]-b,1.0)
GE[1]=fsolve(lambda b: left_elect[1,2]-GE[0]*left_elect[0,2]-b,1.0)
FE[1]=fsolve(lambda b: left_elect[1,1]-FE[0]*left_elect[0,1]-b,1.0)
HF[1]=fsolve(lambda b: left_elect[1,1]-HF[0]*left_elect[0,1]-b,1.0)

#plot border of interpolation domain
pylab.figure(1)
pylab.plot([-6.1,-6.1,-1.8,-1.8,-6.1],[5.5,11.5,11.5,5.5,5.5],'-r')
pylab.xlim(xmin,xmax)
pylab.ylim(ymin,ymax)

#calculate equilibrium capacitance of the left electrode in pF;
#1e-3 is to convert mm to m
#integration region is broken up into a central rectangle and bordering triangles
C0=zeros(4,pylab.Float)
C0[0]=8.85*integrate.dblquad(lambda w,z: 1/0.058, F[0], G[0], lambda x: E[1],\
                             lambda x: H[1])[0]*1e-3
C0[1]=8.85*integrate.dblquad(lambda w,z: 1/0.058, H[0], G[0], lambda x: H[1],\
                             lambda x: HG[0]*x+HG[1])[0]*1e-3
C0[2]=8.85*integrate.dblquad(lambda w,z: 1/0.058, G[0], E[0], lambda x: E[1],\
                             lambda x: GE[0]*x+GE[1])[0]*1e-3
C0[3]=8.85*integrate.dblquad(lambda w,z: 1/0.058, F[0], E[0],\
                             lambda x: FE[0]*x+FE[1], lambda x: E[1])[0]*1e-3
print 'C0 =', sum(C0)
```

```
#calculate change in capacitance in pF due to deflection of wing
#integration region is broken up into a central rectangle and bordering triangles
C1=zeros(4,pylab.Float)
C1[0]=8.85*integrate.dblquad(dinv, F[0], G[0], lambda x: E[1],\
                             lambda x: H[1])[0]*1e-3
C1[1]=8.85*integrate.dblquad(dinv, H[0], G[0], lambda x: H[1],\
                             lambda x: HG[0]*x+HG[1])[0]*1e-3
C1[2]=8.85*integrate.dblquad(dinv, G[0], E[0], lambda x: E[1],\
                             lambda x: GE[0]*x+GE[1])[0]*1e-3
C1[3]=8.85*integrate.dblquad(dinv, F[0], E[0], lambda x: FE[0]*x+FE[1],\
                             lambda x: E[1])[0]*1e-3
print 'deltaC/C0 =', sum(C1-C0)/sum(C0)


"""
pylab.figure(3)
error=[]
for jj in range(shape(wing)[1]):
    error=concatenate((error,[(interpolate.bisplev(wing[0,jj],wing[1,jj],tck)\
                               -wing[2,jj])/wing[2,jj]]))
pylab.plot(error,'.b')
"""
```

BIBLIOGRAPHY

[1] Robert O. Pohl, Xiao Liu, and EunJoo Thompson. Low-temperature thermal conductivity and acoustic attenuation in amorphous solids. *Rev. Mod. Phys.*, 74(4):991, Oct 2002.

[2] J. Jäckle, L. Piché, W. Arnold, and S. Hunklinger. Elastic effects of structural relaxation in glasses at low temperatures. *J. Non-Cryst. Solids*, 20(3):365–91, May 1976.

[3] X. Cao, M. Layer, A. Fleischmann, C. Enss, and S. Hunklinger. SQUID-based technique to study the elastic properties of solids at very low temperatures. *J. Low Temp. Phys.*, 146:295, 2007.

[4] J. Classen, T. Burkert, C. Enss, and S. Hunklinger. Anomalous frequency dependence of the internal friction of vitreous silica. *Phys. Rev. Lett.*, 84(10):2176–2179, Mar 2000.

[5] P. Doussineau, C. Frénois, R. G. Leisure, A. Levelut, and J.-Y. Prieur. *J. Phys. (Paris)*, 41:1193, 1980.

[6] E. Nazaretski, R. D. Merithew, R. O. Pohl, and J. M. Parpia. Measurement of the acoustic properties of amorphous silica above 4.5 mK. *Phys. Rev. B*, 71(14):144201, Apr 2005.

[7] T. H. Metcalf. (private communication).

[8] J. Classen, M. Hübner, C. Enss, G. Weiss, and S. Hunklinger. Similarities and differences between the low-temperature acoustic properties of crystalline materials and glasses. *Phys. Rev. B*, 56(13):8012–8020, Oct 1997.

[9] R. C. Zeller and R. O. Pohl. Thermal conductivity and specific heat of noncrystalline solids. *Phys. Rev. B*, 4(6):2029–2041, Sep 1971.

[10] N. W. Ashcroft and N. D. Mermin. *Solid State Physics*. Brooks/Cole, London, 1976.

[11] W. A. Phillips. Two-level states in glasses. *Rep. Prog. Phys.*, 50(12):1657–708, December 1987.

[12] P. W. Anderson, B. I. Halperin, and C. M. Varma. *Philos. Mag.*, 25:1, 1972.

[13] W. A. Phillips. *J. Low Temp. Phys.*, 7:351, 1972.

[14] C. C. Yu and A. J. Leggett. Low temperature properties of amorphous materials: through a glass darkly. *Comments Cond. Mat. Phys.*, 14(4):231–51, 1988.

[15] A. L. Burin and Yu. Kagan. *Zh. Eksp. Teor. Fiz. [Sov. Phys.—JETP]*, 82:159–171, 1996.

[16] R. Kühn. Universality in glassy low-temperature physics. *Europhys. Lett.*, 62(3):313, May 2003.

[17] J.F. Shackelford and R.H. Doremus, editors. *Ceramic and Glass Materials*. Springer, Berlin, 2008.

[18] R. E. Strakna. Investigation of low-temperature ultrasonic absorption in fast-neutron irradiated SiO_2 glass. *Phys. Rev.*, 123(6):2020–2026, Sep 1961.

[19] J. E. VanCleve. *Elastic Mysteries: The Relationship of the Low-Temperature Elastic Properties of Quasicrystals and Other Alloys to the Phenomenology of Glasses*. PhD thesis, Cornell University, 1991.

[20] R. Loudon. *The Quantum Theory of Light*. Clarendon Press, Oxford, 1973.

[21] R. Shankar. *Principles of Quantum Mechanics*. Plenum Press, New York, 1994.

[22] D. V. Anghel, T. Kühn, Y. M. Galperin, and M. Manninen. Interaction of two-level systems in amorphous materials with arbitrary phonon fields. *Physical Review B (Condensed Matter and Materials Physics)*, 75(6):064202, 2007.

[23] A. S. Nowick and B. S. Berry. *Anelastic Relaxation in Crystalline Solids*. Academic Press, New York, 1972.

[24] S. Hunklinger and W. Arnold. Ultrasonic properties of glasses at low temperatures. In W. P. Mason and R. N. Thurston, editors, *Physical Acoustics*, volume XII. Academic Press, New York, 1976.

[25] Doru Bodea and Alois Würger. Interaction-driven relaxation of two-level systems in glasses. *Phys. Rev. Lett.*, 97(16):165505, 2006.

[26] Z. Nussinov, A. V. Balatsky, M. J. Graf, and S. A. Trugman. Origin of the decrease in the torsional-oscillator period of solid ^{4}He. *Physical Review B (Condensed Matter and Materials Physics)*, 76(1):014530, 2007.

[27] F. Reif. *Fundamentals of Statistical and Thermal Physics*. McGraw Hill, Boston, 1965.

[28] J. P. Sethna. (private communication).

[29] B. Hunt, E. Pratt, V. Gadagkar, M. Yamashita, A. V. Balatsky, and J. C. Davis. Evidence for a superglass state in solid ^{4}He. *Science*, 324:632, 2009.

[30] B.A. Auld. *Acoustic Fields and Waves in Solids*, volume 1. John Wiley & Sons, New York, 1973.

[31] D.R. Southworth, R.A. Barton, S.S. Verbridge, B. Ilic, A.D. Fefferman, H.G. Craighead, and J.M. Parpia. Stress and silicon nitride: A crack in the universal dissipation of glasses. *Phys. Rev. Lett.*, 102(22):225503, June 2009.

[32] P. Esquinazi, editor. *Tunneling Systems in Amorphous and Crystalline Solids*. Springer, Berlin, 1998.

[33] A. L. Burin and I. Ya. Polishchuk. condmat arXiv:0707.2596v1.

[34] D. Bodea and A. Würger. Erratum: Interaction-driven relaxation of two-level systems in glasses. *Phys. Rev. Lett.*, 99:159903, 2007.

[35] A. L. Burin and I. Ya. Polishchuk. condmat arXiv:0709.3324v1.

[36] J. M. Parpia, W. P. Kirk, P. S. Kobiela, T. L. Rhodes, Z. Olejniczak, and G. N. Parker. Optimization procedure for the cooling of liquid ^{3}He by adiabatic demagnetization of praseodymium nickel. *Review of Scientific Instruments*, 56(3):437–443, 1985.

[37] G.C. Straty and E.D. Adams. Highly sensitive capacitance pressure gauge. *Rev. Sci. Inst.*, 40:1393–1397, 1969.

[38] R.L. Rusby, M. Durieux, A.L. Reesink, R.P. Hudson, G. Schuster, M. Kühne, W. E. Fogle, R.J. Soulen, and E.D. Adams. *J. Low Temp. Phys.*, 126:633, 2002.

[39] D.S. Greywall and P.A. Busch. ^{3}He-melting-curve thermometry. *Jour. Low Temp. Phys.*, 46:451–65, 1982.

[40] R. N. Kleiman, G. K. Kaminsky, J. D. Reppy, R. Pindak, and D. J. Bishop. Single-crystal silicon high-Q torsional oscillators. *Review of Scientific Instruments*, 56(11):2088–2091, 1985.

[41] D. J. Griffiths. *Introduction to Electrodyamics*. Prentice Hall, Upper Saddle River, NJ, 1999.

[42] Christoph L. Spiel, R. O. Pohl, and Alan T. Zehnder. Normal modes of a Si(100) double-paddle oscillator. *Review of Scientific Instruments*, 72(2):1482–1491, 2001.

[43] Heraeus-Quarzglas.

[44] H. Hosaka, K. Itao, and S. Kuroda. Damping characteristics of beam-shaped micro-oscillators. *Sensors and Actuators A*, 49:87, 1995.

[45] R.E. Mihailovich and N.C. MacDonald. Dissipation measurements of vacuum-operated single-crystal silicon microresonators. *Sensors and Actuators A*, 50:199, 1995.

[46] A. D. Fefferman, R. O. Pohl, A. T. Zehnder, and J. M. Parpia. Acoustic properties of amorphous silica between 1 and 500 mK. *Physical Review Letters*, 100(19):195501, 2008.

[47] Jürgen T. Stockburger, Milena Grifoni, and Maura Sassetti. Nonlinear acoustic response of glasses in the tunneling model. *Phys. Rev. B*, 51(5):2835–2843, Feb 1995.

[48] J. Classen, C. Enss, C. Bechinger, G. Weiss, and S. Hunklinger. Low frequency acoustic and dielectric measurements on glasses. *Ann. Phys. (Leipzig)*, 3(5):315–35, 1994.

[49] Sonja Rau, Christian Enss, Siegfried Hunklinger, Peter Neu, and Alois Würger. Acoustic properties of oxide glasses at low temperatures. *Phys. Rev. B*, 52(10):7179–7194, Sep 1995.

[50] A. L. Burin and Yu. Kagan. *Zh. Eksp. Teor. Fiz. [Sov. Phys.—JETP]*, 80:761–768, 1995.

[51] EunJoo Thompson, G. Lawes, J. M. Parpia, and R. O. Pohl. Low temperature acoustic properties of amorphous silica and the tunneling model. *Phys. Rev. Lett.*, 84(20):4601–4604, May 2000.

[52] J. Classen, C. Enss, and S. Hunklinger. Comment on low temperature acoustic properties of amorphous silica and the tunneling model. *Phys. Rev. Lett.*, 86(11):2480, Mar 2001.

[53] WWW Table of Radioactive Isotopes, http://nucleardata.nuclear.lu.se/NuclearData/toi/nuclide.asp?iZA=550137.

[54] E. Nazaretski, V.O. Kostroun, S. Dimov, R.O. Pohl, and J.M. Parpia. *JLTP*, 137:609, 2004.

[55] E. Storm and H.I. Israel. *Nucl. Data Tables, A*, 7:565, 1970.

[56] NIST Photon Cross Section Data, http://physics.nist.gov/ PhysRefData/Xcom/html/xcom1.html.

[57] A. L. Burin, I. Ya. Polishchuk, P. Fulde, and Y. Sereda. Low-temperature breakdown of coherent tunneling in amorphous solids induced by the nuclear quadrupole interaction. *Phys. Rev. B*, 73:014205, 2006.

[58] S. Rogge, D. Natelson, B. Tigner, and D. D. Osheroff. Nonlinear dielectric response of glasses at low temperature. *Phys. Rev. B*, 55(17):11256–11262, May 1997.

[59] P. Strehlow and M. Meissner. *Physica B*, 263-264:273, 1999.

[60] T. H. Metcalf. *Elastic Properties, Annealing, and Vapor Pressure of Neon and Argon Films*. PhD thesis, Cornell University, 1991.

[61] J.J. Wortman and R.A. Evans. *Journal of Applied Physics*, 36:153, 1964.

[62] Xiao Liu, EunJoo Thompson, B. E. White, and R. O. Pohl. Low-temperature internal friction in metal films and in plastically deformed bulk aluminum. *Phys. Rev. B*, 59(18):11767–11776, May 1999.

[63] J. L. Black and P. Fulde. Influence of the superconducting state upon the low-temperature properties of metallic glasses. *Phys. Rev. Lett.*, 43(6):453–456, Aug 1979.

[64] Tejs Vegge, James P. Sethna, Siew-Ann Cheong, K. W. Jacobsen, Christopher R. Myers, and Daniel C. Ralph. Calculation of quantum tunneling for a spatially extended defect: The dislocation kink in copper has a low effective mass. *Phys. Rev. Lett.*, 86(8):1546–1549, Feb 2001.

[65] B. E. White. *Elastic Properties of Amorphous Thin Films*. PhD thesis, Cornell University, 1996.

[66] R. König, P. Esquinazi, and B. Neppert. Tunneling systems in polycrystalline metals: Absence of electron-assisted relaxation. *Phys. Rev. B*, 51(17):11424–11432, May 1995.

[67] W. Wasserbäch, S. Abens, S. Sahling, R. O. Pohl, and Eunjoo Thompson. *Phys. Stat. Sol.*, 228:799–823, 2001.

[68] P. D. Vu, Xiao Liu, and R. O. Pohl. Phonon scattering and internal friction in dielectric and metallic films at low temperatures. *Phys. Rev. B*, 63(12):125421, Mar 2001.

[69] D. Hull and D. J. Bacon. *Introduction to Dislocations*. Pergamon Press, Oxford, 1984.

[70] A. Hikata and C. Elbaum. Dislocation drag in sodium chloride at low temperature. *Phys. Rev. B*, 9(10):4529–4541, May 1974.